ALL-SOFT ELECTRONIC DEVICES AND INTEGRATED MICROSYSTEMS ENABLED BY LIQUID METAL

A Dissertation
Presented to
The Academic Faculty

by

Min-gu Kim

In Partial Fulfillment
of the Requirements for the Degree
Doctor of Philosophy in the
School of Electrical and Computer Engineering

Georgia Institute of Technology
May 2019

ALL-SOFT ELECTRONIC DEVICES AND INTEGRATED MICROSYSTEMS ENABLED BY LIQUID METAL

Approved by:

Dr. Oliver Brand, Advisor
School of Electrical and Computer Engineering
Georgia Institute of Technology

Dr. Bernard Kippelen
School of Electrical and Computer Engineering
Georgia Institute of Technology

Dr. Omer T. Inan
School of Electrical and Computer Engineering
Georgia Institute of Technology

Dr. Seung Woo Lee
The George W. Woodruff School of Mechanical Engineering
Georgia Institute of Technology

Dr. Muhannad S. Bakir
School of Electrical and Computer Engineering
Georgia Institute of Technology

Date Approved: March 11, 2019

To my wife Eun kyung, my daughter Sophia Seoyun,

my parents and in-law Jubeom, Younbun, Seewon, Myunghee, and my sister Minhye,

for their endless love and support.

ACKNOWLEDGEMENTS

I would like to express my deepest appreciation to my advisor Dr. Oliver Brand for his support, guidance, and encouragement to explore a new research area. Dr. Brand has provided me with many opportunities to participate in various research projects. These experiences have been extremely valuable to broaden my research horizon and think in a bigger picture. Beyond academics, his gentleness, enthusiasm, and leadership have greatly inspired me in many aspects, which will be an invaluable asset in my life.

Along the same line, I would like to thank Dr. Bernard Kippelen, Dr. Omer Inan, Dr. Muhannad Bakir, Dr. Seung Woo Lee, and Dr. Maysam Ghovanloo for serving on my dissertation & proposal committees and for providing valuable advice. I have been involved in several collaborative research projects with Dr. Maysam Ghovanloo and Pyungwoo Yeon on a soft wireless sensing platform and its optimization process, and I want to thank both for their technical support and discussion. I wish to thank Dr. Seung Woo Lee and Dr. Byeongyong Lee for the rewarding collaboration on soft supercapacitors. I am grateful for their generous support and constructive discussion. I would like to thank Dr. Bernard Kippelen, Dr. Canek Fuentes-Hernandez, Xiaojia Jia, and Youngrak Park for collaboration opportunities in the area of flexible organic electronics. In addition, I have had the pleasure to meet Dr. Michael Dickey and his students at the NC State University. Their insights and technical discussions were particularly helpful for my current and future research. Furthermore, I want to thank Dr. Gary May of the University of California at Davis, Dr. Luke Lee of the National University of Singapore, Dr. Chong H. Ahn of the University of Cincinnati, Dr. Jeong-Bong Lee of the University of Texas at Dallas, Dr. Kang-Wook Lee of

the IBM T. J. Watson Research Center, and Dr. Christopher Tabor of the Air Force Research Lab (AFRL) for their valuable advice and support.

I am very fortunate to have worked with the members of the Integrated Sensing Systems (iSenSys) group and the Institute for Electronics and Nanotechnology (IEN) at the Georgia Institute of Technology. I am grateful to all my past and present group mates Dr. Christopher Carron, Dr. Spyridon Pavlidis, Dr. Patrick Getz, Dr. Hommood Alrowais, Dr. Luke Beardslee, Choongsoon Kim, Devin Brown, Steven Schwartz, Biya Haile, and Isha Lodhi. Also, thanks to Purnima Sharma for her tireless help with all administration processes. I want to thank the IEN staff members Gary Spinner, Dr. Hang Chen, Devin Brown, Dr. Paul Joseph, Richard Schafer, and Dr. Seung-Joon Paik for their cleanroom support and help. In addition, I would like to express my appreciation to the entire Georgia Tech community for providing me with a memorable experience.

I would like to express my sincere gratitude to my parents Jubeom Kim and Younbun Nam, my parents-in-law Seewon Ryu and Myunghee Kim, and my sister Minhye Kim. Lastly but most importantly, one of the greatest achievements in my life is to marry my wife Eun Kyung Ryu and have a daughter Sophia Seoyun Kim. Words cannot express how grateful I am to my family, and I would not have accomplished any of my goals without their endless love and support.

Min-gu Kim

March 2019

Atlanta, GA, USA

TABLE OF CONTENTS

LIST OF TABLES

LIST OF FIGURES

LIST OF SYMBOLS AND ABBREVIATIONS

SYMBOLS

σ	Electrical conductivity
ρ	Electrical resistivity
k	Thermal conductivity
γ	Surface tension
E	Young's modulus
υ	Poisson's ratio
ε	Strain
ε_0	Permittivity of free space
ε_r	Relative permittivity
f_{res}	Self-resonance frequency
K	Partition coefficient
D	Diffusion coefficient
τ_{res}	Response time
τ_{rec}	Recovery time

ABBREVIATIONS

AR	Aspect ratio
CNT	Carbon nanotube
EGaIn	Eutectic gallium-indium alloy
EtOH	Ethanol
Galinstan	Eutectic gallium-indium-tin alloy

GF	Gauge factor
HR	Heart rate
IDE	Interdigitated electrode
i-PrOH	Isopropanol
IR	Infrared
LbL	Layer by layer
MeOH	Methanol
NP	Nanoparticle
NW	Nanowire
O-CNT	Oxygen-functionalized carbon nanotube
PDMS	Poly(dimethylsiloxane)
PPG	Photoplethysmogram
Res	Resolution
RH	Relative humidity
sMEA	Soft microelectrode array
sPCB	Soft printed circuit board
SpO_2	Saturation of peripheral oxygen
sTPV	Soft through-PDMS via
SWNT	Single-walled carbon nanotube
VOC	Volatile organic compound
VMR	Volume mixing ratio

SUMMARY

The objective of this thesis is to explore all-soft electronic devices and integrated microsystems enabled by gallium-based liquid metal (eutectic gallium-indium alloy, EGaIn) to realize fully-integrated wearable and skin-mountable electronics. Lightweight, flexible, and stretchable wearable electronics have gained significant attention for various sensing applications ranging from entertainment to healthcare, but the mechanical mismatch between soft biological skins and conventional rigid and bulky electronic materials often limits the ultimate usability and leads to hard-soft material interface failure. To circumvent this limitation, the use of conducting liquid, such as EGaIn, has great potential because of its low melting temperature, and excellent electrical and mechanical properties. However, EGaIn patterning challenges, particularly regarding minimum feature sizes, size-scalability, uniformity, and residue-free surfaces, have limited its use for the demonstration of high-density electronic devices. These technical challenges have motivated the development of novel EGaIn patterning and integration technologies to develop all-soft microelectronic devices and fully-integrated soft microsystems.

This research particularly focuses on lithography-enabled thin-film patterning techniques for EGaIn structures with dimensions ranging from the nanometer scale to the centimeter scale. Soft-lithography-based EGaIn thin-film patterning techniques utilizing subtractive reverse stamping and additive stamping processes is investigated. Microscale EGaIn thin-film patterning using subtractive reverse stamping yields high-resolution (>2 μm), size-scalable (μm to 1-2 mm), uniform, and residue-free EGaIn thin-film structures. Uniform, large-area (mm to cm) EGaIn thin-film patterning is achieved using a

complementary additive stamping technique. While micrometer-scale EGaIn thin-film patterning is demonstrated using the subtractive reverse stamping technique, scaling this process down to submicron features is difficult because of the high surface tension of EGaIn. To overcome this limitation, a novel hybrid fabrication technique using electron-beam lithography in combination with soft lithography is investigated. Using this technique, for the first time, submicron-scale EGaIn thin-film patterning with feature sizes as small as 180 nm is demonstrated.

The developed multiscale EGaIn patterning techniques in combination with a vertical integration approach based on EGaIn-filled soft vias overcome the current limitation in EGaIn fabrication and integration. Combining the scalable fabrication based on soft lithography and vertical integration techniques, 3D-integrated, soft functional microsystems are demonstrated for physical strain and pressure sensing and chemical environmental sensing applications. The developed 3D-integrated, physical and chemical microsystems improve over a single sensor by enabling high-density integration, multifunctional sensing capabilities, as well as mechanical flexibility and stretchability. In addition, all-soft and liquid-phase supercapacitors based on oxygen functionalized CNT-integrated EGaIn electrodes are demonstrated for powering soft electronic devices. The supercapacitors represent the first demonstration of an all-soft platform based on EGaIn for high-performance and wearable energy storage.

CHAPTER 1. INTRODUCTION

1.1 Motivation

Bio-inspired and skin-like electronics, which have lightweight, flexible, stretchable, and biocompatible characteristics, are an intriguing technological platform that can augment human vision, audition, gustation, olfaction, and somatosensation for various sensing applications ranging from military, entertainment to healthcare [1-4]. Several examples of skin- and body-mountable healthcare sensing platforms have been recently reported [5-7]. Figure 1.1 (a) shows the demonstrated "smart lens" from Verily Life Sciences and Alcon, used to diagnose diseases and allow unobtrusive and continuous monitoring of patients [5]. To fit comfortably on eyes, the smart lense is made of soft materials such as hydrogel and incorporates solid-state sensors and microelectronic circuits in a flexible hybrid electronics format to operate sensor, manage power, and transmit data to an external device. Although the lens itself is flexible, incorporation of rigid electronic components increases the risk of eye irritation and obstructs vision. Similarly, a fully-integrated, wearable sweat sensing system has been demonstrated at the University of California, Berkeley [6]. The integrated sensing system (see Figure 1.1 (b)), which is able to detect glucose, lactate, sodium, and potassium in sweat as well as the body temperature, uses an electrochemical sensor array fabricated on a flexible polyethylene terephthalate (PET) substrate. The flexible sweat sensor array is connected to a flexible printed circuit board with off-the-shelf electronic components and a lithium-ion polymer. Although the sensing system can be worn directly on the body, the use of rigid electronics with rigid interconnects limits system-level mechanical flexibility and stretchability.

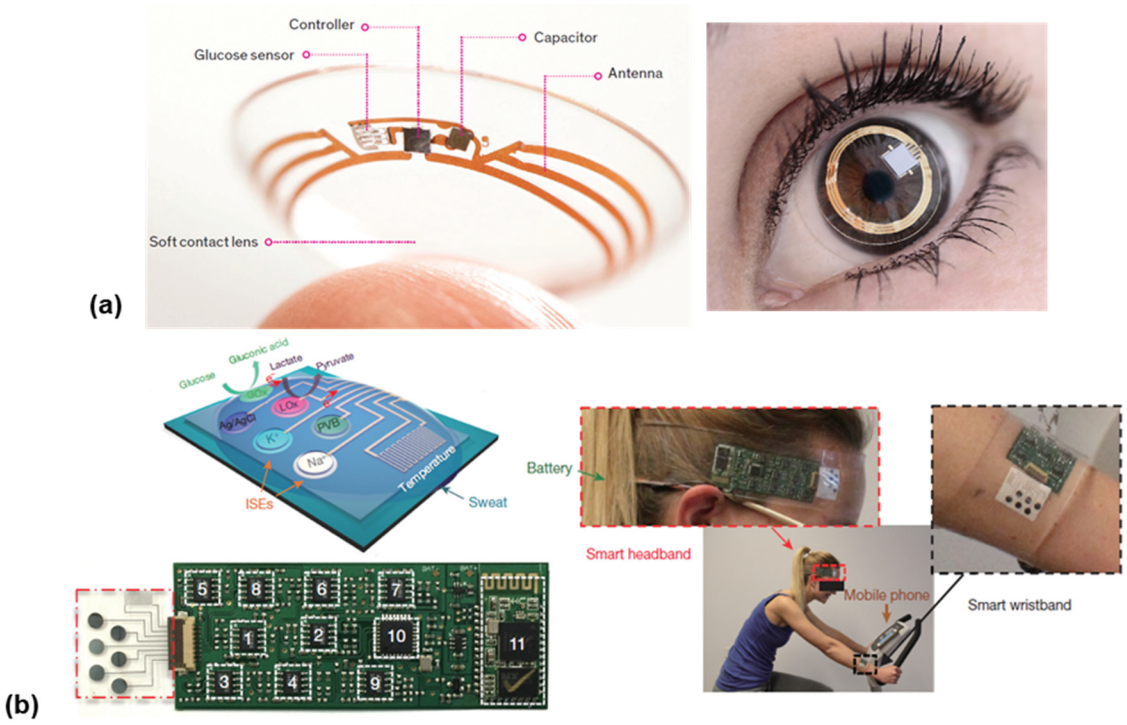

Figure 1.1 Flexible healthcare sensing platforms: (a) contact lens with an integrated glucose sensor [5] and (b) wearable integrated sweat sensing system [6].

Overall, current, state-of-the-art wearable and skin-mountable electronics routinely rely on sensors and electronics, which are integrated on relied on rigid and stiff substrates, interconnected with rigid wires and encapsulated in plastic packaging. Thus, one of the remaining major technical challenges is the mechanical mismatch between soft biological skins and tissues and the conventional rigid and bulky electronic materials often used in wearable healthcare platforms [8, 9]. This challenge has initiated the development of a variety of soft electronic materials, fabrication methods, and detection schemes to provide a seamless link between humans and the digital world [1, 9, 10]. In this regard, the use of liquid-phase conductors and elastomeric substrates (e.g. poly(dimethylsiloxane), PDMS) offer new opportunities for soft, deformable, and self-healing electronic devices [11, 12]. Among conducting liquids, gallium-based liquid metal, in particular eutectic gallium-

indium (EGaIn), is of particular interest because of its low toxicity, low melting temperature, as well as excellent electrical and mechanical properties [13, 14]. However, EGaIn patterning and integration challenges with respect to minimum feature sizes, size-scalability, uniformity, and residue-free surfaces, have limited its use to demonstrate soft electronic devices and integrated microsystems. These technical challenges have motivated the development of novel EGaIn patterning and integration technologies to develop all-soft microelectronic devices and fully-integrated soft microsystems, as shown in Figures 1.2. The proposed integrated soft microsystems, which comprise a soft electronic device, such as a sensor and/or circuit, and a soft energy storage element, can be utilized for wearable and skin-mountable physical, chemical, and biological sensing applications.

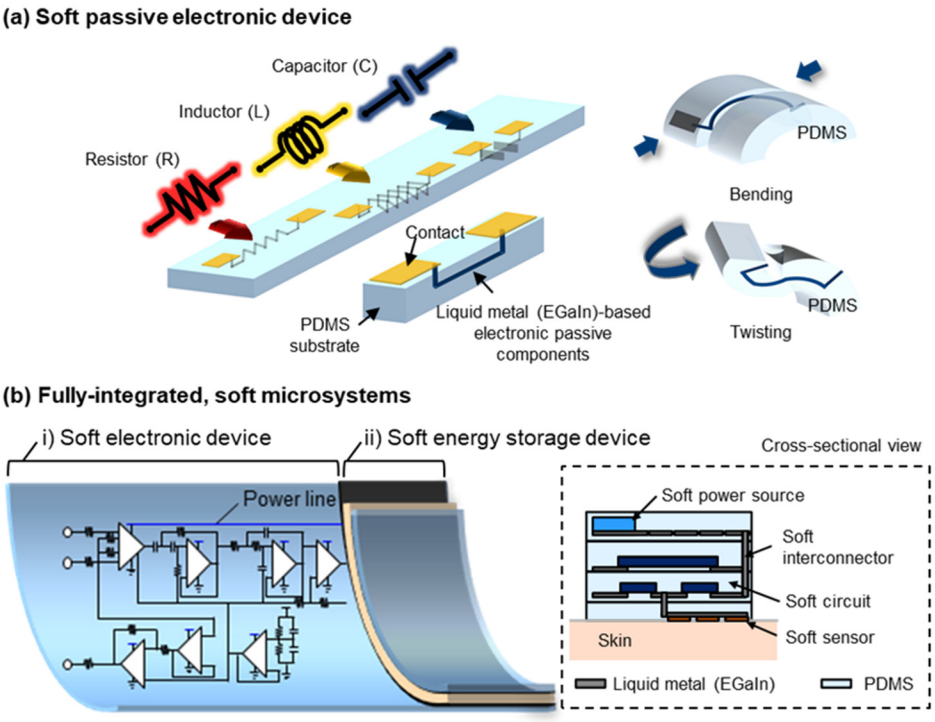

Figure 1.2 Schematic illustration of (a) soft electronic passive devices, including a resistor, an inductor, and a capacitor, that can change shape in response to bending or twisting forces and (b) integrated soft microsystems, comprising soft electronic sensors and circuits and soft energy storage elements, implemented using gallium-based liquid metal (eutectic gallium-indium (EGaIn)).

1.2 Materials and Approaches for Soft Electronic Devices

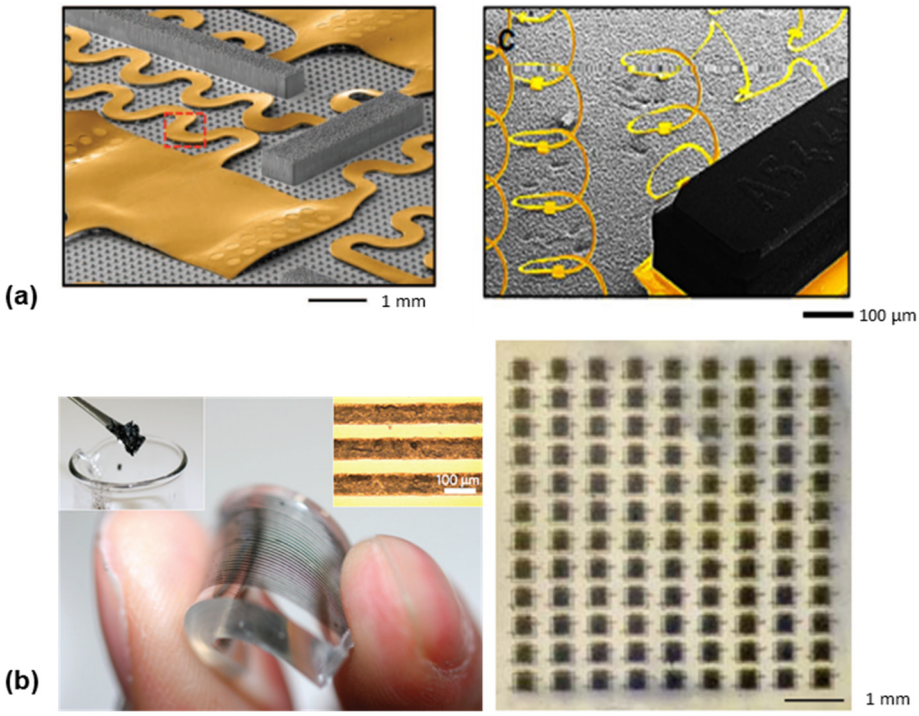

Figure 1.3 Approaches to achieve flexible and stretchable electronics: (a) 2D (left) [15] and 3D (right) [16] compliant wave-like, solid metal patterns and (b) conductive nanocomposite patterns, fabricated by mixing single-walled carbon nanotubes (SWNTs) into polymer matrices (left) [17] or printing SWNTs onto soft substrates (right) [18].

The growing demand for wearable and skin-mountable electronics has resulted in significant research in the area of soft and stretchable electronics, which maintain their electrical functionality even upon significant mechanical deformation [8, 9, 19]. Different materials and fabrication approaches to achieve flexible and stretchable electronic characteristics have been introduced. As an example, Figure 1.3 (a) shows 2D and 3D compliant wave-like, solid metal patterns on a soft substrate that can endure large mechanical deformation [15, 16, 20, 21]. Limitations of this approach are that the rigid wavy metal patterns limit the ultimate strain and lower the density of electronic components. As an alternative approach, Figure 1.3 (b) shows printed highly elastic

conductors, obtained by mixing conductive nanomaterials (e.g. carbon nanotubes (CNTs), nanowires (NWs), or nanoparticles (NPs)) into polymer matrices or by dispensing them directly onto soft substrates [17, 18, 22, 23]. This approach enables inexpensive fabrication processes by printing inks for conductive circuits, but the relatively low resolution and low conductivity of these conductors are still challenging for high-density electronics integration.

Figure 1.4 Intrinsically soft and liquid-phase conductor: gallium-based liquid metal (eutectic gallium-indium alloy, EGaIn) [14].

As an alternative to these conventional approaches, the use of intrinsically soft conductors is a promising approach to realize all-soft and skin-like electronics [11, 12]. Thereby, the use of low melting temperature metals (see Figure 1.4), such as gallium-based liquid metal (eutectic gallium-indium (EGaIn, 75% Ga and 25% In, by weight) or eutectic gallium-indium-tin (Galinstan, 68.5% Ga, 21.5% In, and 10% Sn, by weight)), could pave the path for all-soft electronics [13]. This study primarily focuses on EGaIn. EGaIn offers a number of advantages including its reduced toxicity (compared to toxic liquid metals, such as mercury (Hg)), low melting temperature (MP < 15 °C), favorable mechanical stretchability (being a liquid, it offers very large stretchability, which is ultimately limited by the mechanical properties of the encasing material), thermal conductivity (k = 26.6 W m^{-1} K^{-1}), and electrical conductivity ($\sigma = 3.4 \times 10^6$ S m^{-1}) [24]. A thin oxide layer ($t \approx$ 1-3

nm) formed on the EGaIn surface under atmospheric oxygen level allows EGaIn to be molded in elastomeric substrates [25]. As EGaIn is a liquid-phase conductor with a brittle oxide layer on its surface, the shape of a microchannel filled with EGaIn can be easily changed in response to mechanical deformation with a new oxide layer instantaneously being formed on the EGaIn surface, making it shape reconfigurable. Table 1.1 summarize the physical properties of the gallium-based liquid metal (EGaIn and Galinstan), in comparison to gallium (Ga), and mercury (Hg).

Table 1.1. Physical properties of low melting temperature soft conductors.

Physical property	Eutectic Ga-In (EGaIn)	Eutectic Ga-In-Sn (Galinstan)	Gallium (Ga)	Mercury (Hg)
Melting point [°C]	15	-19	29.8	-39
Boiling point [°C]	2000	>1300	2200	357
Density [kg m^{-3}]	6250	6440	6100	13599
Viscosity [10^{-3} Pa s]	1.99	2.4	1.37	1.52
Electric conductivity [10^{6} S m^{-1}]	3.4	3.4	6.7	1.0
Thermal conductivity [W m^{-1} K^{-1}]	26.6	16.5	29	8.5

1.3 Liquid Metal Patterning Technologies

The moldable characteristic of EGaIn thanks to the formation of the oxide skin has led to the development of a broad range of patterning methods based on lithography-enabled stamping and stencil printing, injection, as well as additive and subtractive direct write/patterning processes [26], as shown in Figure 1.5 and summarized in Table 1.2. EGaIn patterning using lithography-defined stencils yields simple and high throughput EGaIn patterning on elastomeric substrates with smallest feature sizes of width (w) ≈ 200 μm and thickness (t) ≈ 50 μm using metal stencil films [27], w ≈ 10 μm and t ≈ 2 μm using microfabricated metal stencil films [28], and w ≈ 20 μm and t ≈ 10 μm using polymer stencil films [29]. Limitations of this approach are the relatively low resolution, rough EGaIn surface, and considerable EGaIn waste during the stencil lift-off process. Subtractive direct patterning techniques using laser ablation [30] or electrochemical reduction [31] enable an inexpensive and facile approach to pattern fine EGaIn lines, but the serial process makes EGaIn removal slow in the case of patterning small EGaIn features on large substrates. The major technical challenge for both lithography-enabled stencil printing and subtractive direct patterning approaches is that creating thin and uniform EGaIn films are difficult due to the high surface tension of EGaIn (γ = 624 mN m^{-1}). Manually spreading EGaIn using a roller typically results in rough surfaces with holes in the EGaIn film [32]. Additive direct write and injection approaches address the EGaIn waste and uniformity issues [26]. 2D/3D direct writing techniques allow to deposit EGaIn patterns in desired locations only, but the resolution is limited to w ≈ 100 μm and t > 50 μm because of the size limitation of the injection nozzles [33, 34]. Microfluidic injection [35] and vacuum filling [36] approaches provide better resolution with w > 10 μm, but the

microchannel requires relatively large thicknesses of $t > 50$ μm to reduce pressure drops, and its practical use is limited when EGaIn film needs to be exposed to the surface for additional processing. Using a microtransfer deposition process based on soft lithography, the smallest EGaIn features so far with $w > 2$ μm were demonstrated [37], but the technology suffered from EGaIn residues formed outside of the channel areas during the molding process.

To summarize, unlike solid metal patterning based on conventional micro and nanofabrication, creating smooth and uniform EGaIn thin films is the primary technical hurdles besides the need for high resolution and size scalability [38]. Therefore, developing a high-resolution and uniform thin-film deposition and patterning technique, which covers micrometer to centimeter scale patterns without EGaIn residues, may open vast opportunities for the fabrication and integration of soft microsystems.

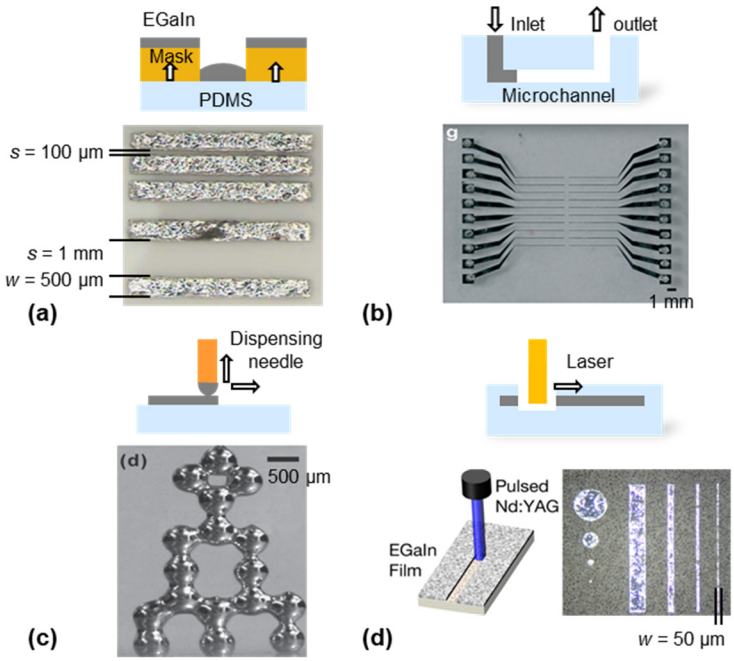

Figure 1.5 Schematic illustration of EGaIn patterning processes and fabrication results using (a) lithography-enabled stencil printing [27], (b) injection [36], (c) additive 3D printing [34], and (d) subtractive laser ablation [30] processes.

Table 1.2. Summary of EGaIn patterning technologies using lithography-enabled stamping and stencil printing, injection, additive, and subtractive processes.

Patterning techniques	Approach	Minimum feature size (w)	Film thickness (t)	Note
Lithography enabled based on stamping	Microtransfer molding [37]	2 μm	1 μm	– Microscale line patterning – Liquid metal residue on surfaces
Lithography enabled based on stencil printing	Metal film [27]	200 μm	≈ 50 μm	– Simple and high throughput process – Relatively large feature size – Non-uniform and rough edge
	Microfabricated metal films [28]	10 μm	≈ 2 μm	
	Polymer film [29]	20 μm	≈ 10 μm	
Injection	Fluidic injection [35]	200 μm	300 μm	– Simple, fast, and low-cost process – Better resolution – High channel thickness
	Vacuum filling [36]	10 μm	> 50 μm	
Additive	2D Printing [33]	83 μm	≈ 50 μm	– 2D/3D structure fabrication – Relatively low resolution – Uniform thickness
	3D Printing [34]	≈ 100 μm	≈ 100 μm	
Subtractive	Laser ablation [30]	50 μm	≈ 17 μm	– Relatively low resolution – Non-uniform thickness – Excessive liquid metal loss
	Electrochemical reduction [31]	≈ mm	≈ 100 μm	

1.4 Liquid-Metal-Based Soft Sensing Platforms

From the above discussions, it is evident that EGaIn offers a number of advantages with respect to favorable electrical and mechanical properties. In this chapter, soft and stretchable sensing platforms will be reviewed focused on EGaIn. Subchapter 1.4.1 examines physical strain sensing platforms, and Subchapter 1.4.2 discusses chemical sensing platforms.

1.4.1 Physical Strain Sensing Platforms

Soft and stretchable strain sensors respond to applied strain utilizing resistive, capacitive, or optical sensing principles [39]. Subchapter 1.4.1 mainly focuses on resistive-type strain sensors, which are more suitable for wearable and skin-mountable electronics because they require relatively simple readout circuits and offer high flexibility and stretchability. Soft and stretchable strain sensor have been investigated using nanomaterials (e.g. CNTs [23, 40, 41], NWs [42, 43], and NPs [44, 45]) and liquid-phase conductors (e.g. EGaIn [35, 46, 47]) as shown in Figure 1.6. Elastomers (e.g. PDMS and Ecoflex) are commonly used as supporting materials of soft and stretchable sensors.

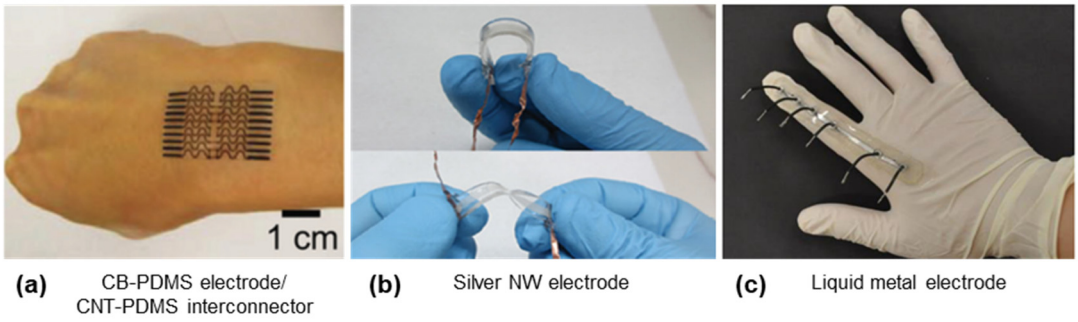

Figure 1.6. Soft and stretchable strain sensors based on (a) carbon-black-doped PDMS (CB-PDMS) electrodes and carbon-nanotube-doped PDMS (CNT-PDMS) interconnector [41], (b) silver nanowire electrodes [42], and (c) liquid metal electrodes [47].

By utilizing conductive nanomaterials, strain sensing mechanism using disconnection between sensing elements [42, 43] and crack propagation in thin films [40, 44] have been investigated (see Figure 1.6). In case of conductive nanowire networks, electrons can flow through overlapping nanomaterials within a percolation network [42]. Stretching nanomaterial-containing thin films causes some connected nanomaterials to lose their overlapped area and, thus, resulting in an increase of the electrical resistance [42]. In case of brittle CNT or nanoparticle films, crack propagation is dominant. Cracks originate and propagate in brittle thin films coated on soft polymer upon stretching [41]. As a result, the electrical resistance is drastically increased by applying strain and reduced again upon release of the applied strain [44]. In general, nanomaterial-based strain sensors shows high sensitivity, but nonlinearity and hysteresis are main drawbacks, which makes the calibration process complex and difficult.

By utilizing liquid-phase conductors, nonlinearity and hysteresis issues can be minimized [48]. In case of EGaIn-filled microchannels, the strain-resistance response primarily originates from geometrical effects [49]. The resistance change with applied strain can be explained by the effect of geometry changes on the resistance, given by $R = \rho L/A$, where ρ is the electrical resistivity, L is the length, and A is the cross-sectional area of the conductor. The thin-film resistivity of EGaIn is identical to its bulk resistivity ($\rho = 29.4 \times 10^{-8}$ Ω m) [37]. EGaIn-filled strain sensors could be stretched >100% and showed linear strain responses with little hysteresis and delay, but the limitation is low sensitivity (gauge factor ($GF = (\Delta R/R)/\varepsilon) \approx 2$) [49]. Demonstrated strain sensors showed high durability >1000 cycles without noticeable degradation.

Overall, the major technical challenges for soft and stretchable strain sensors are to achieve high stretchability, high sensitivity, as well as linearity with little hysteresis. Moreover, the system-level integration of soft and stretchable electronics is a significant technical challenge, considering the need for integrating readout circuits, energy storage components, and communication units with the sensing elements. Table 1.3 compares resistive-type strain sensor performances demonstrated in the literature.

Table 1.3. Comparison of strain sensor demonstrated in the literature.

Mechanism	Materials	Stretchability	Sensitivity	Linearity
Geometry changes	EGaIn-PDMS [35]	100%	≈ 3.6-3.9	Linear
	EGaIn-Ecoflex [46]	700%	≈ 1.5-2	Linear
Disconnection mechanism	Ag NWs-PDMS [42]	70%	≈ 2-14	Nonlinear
	ZnO NWs/PSNF* -PDMS [43]	50%	≈ 116	Linear
Crack propagation	SWNTs**-PDMS [40]	280%	0.82	Nonlinear
	Ag NPs-PDMS [44]	20%	2.05	Linear

*PSNF: polystyrene nanofiber, **SWNT: single-walled carbon nanotube

1.4.2 Chemical Environmental Sensing Platforms

Soft and stretchable chemical sensing platforms based on EGaIn have been investigated for healthcare and environmental monitoring applications [24, 50, 51]. Thanks to EGaIn's high electrical conductivity and fluidic behavior, EGaIn can serve as an injectable and deformable electrode [24, 25]. Thereby, the oxide layer (Ga_2O_3) on the EGaIn surfaces enables stable EGaIn structures inside of the microchannels and allows for direct contact with applied chemicals [52]. Above behavior allows the designer to integrate EGaIn electrodes into microfluidic systems for environmental and biosensing applications.

EGaIn drop electrodes have been investigated for heavy metal ion sensing, instead of using toxic liquid metal, such as mercury [53, 54]. The hanging liquid metal drop electrode can be employed in the voltammetric analysis of heavy metal ions, such as Pd^{2+} and Cd^{2+}. Also, miniaturized heavy metal ion sensing platform using EGaIn microdroplet electrodes was demonstrated to increase sensitivity [55].

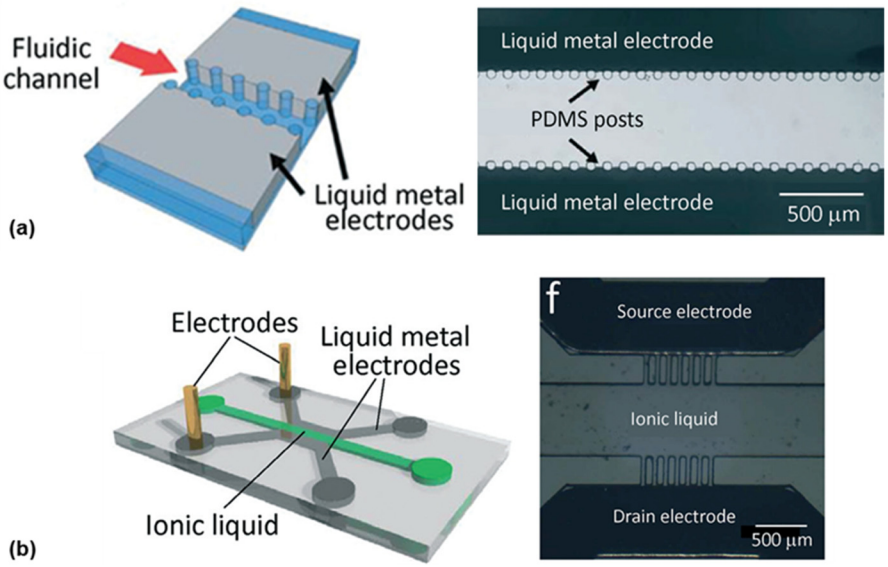

Figure 1.7 Soft microfluidic chemical sensing platforms with pre-aligned liquid metal electrodes for (a) electrohydrodynamic mixing [52] and (b) temperature, humidity, and oxygen sensing [56].

EGaIn microelectrodes that are injected in PDMS microfluidic channels containing PDMS posts have been investigated for liquid- and gas-phase chemical analysis [51, 52, 56]. Figure 1.7 (a)-(b) shows the soft and stretchable microfluidic platform with three fluidic channels, where two EGaIn channels are in contact with a central fluidic channel via small junction channels [52, 56]. Injected EGaIn are inherently aligned with and in direct contact with the central microfluidic channels for electrohydrodynamic mixing [52] and neural stimulation within the microfluidic platform [51] (Figure 1.7 (a)). Figure 1.7 (b) shows the microfluidic platforms for gas-phase chemical sensing based on resistive and

capacitive transduction mechanisms [56]. EGaIn-based gas sensing performance has been investigated using different ionic liquids for humidity and oxygen sensing (1-ethyl-3-methylimidazolium trifluoromethanesulfonate [EMIM][Otf], 1-butyl methylimidazolium hexafluorophosphate [BMIM][PF_6], and 1-butyl-1-methylpyrrolidinium bis (trifluoromethylsulfonyl)imide [BMPYR][NTf_2] [56]. Thereby, the device measures the capacitance and conductance of the ionic liquid in response to temperature, humidity, and oxygen changes. For oxygen gas sensing, the sensitivity was characterized using various ionic liquids, and the highest sensitivity reveals 1% increase in conductance per 1% increase in oxygen concentration. However, the limitation is slow response and recovery time constants (>1 hour time constants).

1.5 Soft Energy Storage Components

Recently, a number of wearable healthcare sensing systems have been demonstrated [6, 57]. Although the fabrication and characterization of flexible sensors have been successfully demonstrated, their system-level integration with rigid and heavy solid-state energy storage components is a major limiting factor for wearable and skin-mountable electronics applications. To power and better integrate with soft electronic devices, future energy storage components require lightweight, flexible, and stretchable characteristics, as well as high energy density, and excellent electrochemical and mechanical stability [58-60].

Supercapacitors, also known as electrochemical capacitors, are considered a promising mobile energy storage solution because of their ultrafast power supply, high energy density, and long cycle life [58, 61]. Supercapacitors are composed of two

electrodes and an ion-permeable membrane with liquid or solid electrolyte to ionically connect both electrodes [62]. When a voltage is applied, ions in the electrolyte form electrical double-layers of opposite polarity to the electrode's polarity. The high capacitances of supercapacitors mainly arise from surface reactions of electrode materials, including electrochemical adsorption/desorption of cations and anions at the electrode/electrolyte interface, and surface faradaic redox reactions [58, 62]. Depending on the charge storage mechanisms, supercapacitors can be classified to electrical double-layer capacitors (ion adsorption), pseudocapacitors (surface redox reactions), and hybrid capacitors (ion adsorption and surface redox reactions) [62]. Conventional electrodes for supercapacitors are mainly manufactured by coating slurry materials, containing active materials (e.g. transition-metal oxides) and conductive materials (e.g. carbon-based nanomaterials), onto a metallic current collector using polymer binders (e.g. poly(vinylidene fluoride) [59, 63]. These rigid current collectors mechanically/electrically fail at strains of the order of 1-2% and the coated active/conductive materials are easily delaminated from the current collector by mechanical deformation, making their use in wearable and skin-mountable applications challenging [59]. In this respect, the design and fabrication of flexible and stretchable electrodes is one of the key challenges for soft energy storage devices.

Buckled or wavy carbon nanomaterials have been mainly used for soft and stretchable energy storage components. Stretchable supercapacitors using buckled single-walled CNT (SWNT) electrodes have been demonstrated [64-66]. Thereby, the SWNT microfilms were printed on a pre-strained PDMS substrate. Then, buckled SWNT patterns could be formed by releasing the pre-strained PDMS because the mechanical mismatch

between the relatively stiff SWNT film and the soft PDMS substrate causes the surface to buckle (Figure 1.8 (a)). The obtained specific capacitance was 54 F g^{-1} without applied strain, and 52 F g^{-1} at 30% applied strain at the current density of 1 A g^{-1}, indicating no significant change of the electrochemical performance with applied strain [64]. Two-dimensional carbon-based nanomaterials, such as crumpled graphene, have also been adopted for stretchable supercapacitors [67-70]. Crumpled graphene electrodes were obtained by transferring a graphene film to a pre-strained PDMS substrate. The resulting specific capacitance was 196 F g^{-1} at the current density of 1 A g^{-1} and showed good reliability over 1,000 stretch/release cycles [67]. Textile-based stretchable supercapacitors were demonstrated using a simple "dipping and drying" process for wearable electronics applications [71-73]. Thereby, stretchable textile electrodes were fabricated by dipping cellulose cotton textile substrates into an aqueous SWNT ink, as shown in Figure 1.8 (b). The fabricated textile supercapacitors showed an areal capacitance of 0.48 F cm^{-2} and cycling stability over 3,000 cycles [71]. Finally, stretchable solid-state supercapacitor arrays were demonstrated using SWNT electrodes with serpentine metal interconnections (Figure 1.8 (c)) [74, 75]. To achieve the mechanical stability over deformation, narrow serpentine metallic interconnections were encapsulated with polyimide films. Then, SWNT electrodes were spray-coated on Ti/Au current collector electrodes. Fabricated supercapacitor arrays showed a capacitance of ~100 μF at a scan rate of 500 mV s^{-1} (55.3 F g^{-1} at a scan rate of 500 mV s^{-1}) [74]. The electrochemical performance was stable under strain up to 30% [74]. Overall, stretchable supercapacitors have been demonstrated relying on carbon-based conductive networks used as current collectors. While these conductive carbon networks enabled highly flexible and stretchable devices, their relatively low

conductivity compared to metallic current collectors as well as their conductivity decrease under applied strain are considered limitations [10, 17, 76]. Furthermore, the design and fabrication of soft and stretchable current collectors that do not suffer from active material delamination remains a technical challenge for high-performance, stretchable energy storage solutions for integrated soft microsystems.

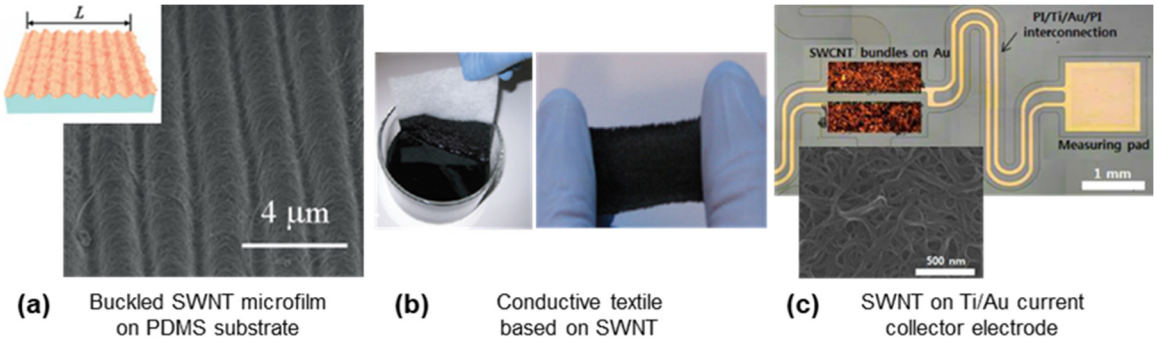

Figure 1.8. Soft electrodes for stretchable supercapacitors: (a) buckled single-walled CNT (SWNT) microfilms printed on a pre-strained PDMS substrate [64], (b) conductive textile fabricated by dipping into SWNT ink [71], and (c) SWNT on a solid current collector electrode [74].

1.6 Thesis Outline

The objective of this thesis is to explore all-soft electronic devices and integrated microsystems enabled by EGaIn. To this end, lithography-enabled and multiscale EGaIn thin-film patterning techniques with a vertical integration approach are developed to overcome the current limitation in EGaIn fabrication and enable size-scalable and high-density all-soft electronic devices and integrated microsystems. Combining the scalable fabrication and integration techniques, 3D-integrated, soft functional microsystems are investigated for physical strain sensing and chemical environmental sensing applications.

In addition, soft energy storage devices are investigated to demonstrate a path towards fully-integrated soft microsystems. To address these research objectives, this thesis is outlined in the following manner.

Chapter 2 investigates microscale EGaIn thin-film patterning using a subtractive reverse stamping technique based on soft lithography and a vertical integration technique for soft microelectronic devices. Size-scalable and uniform EGaIn thin-film patterning ranging from single micron to several millimeters in line width at room temperature and in ambient pressure is demonstrated.

Chapter 3 presents centimeter-scale EGaIn thin-film patterning using an additive stamping technique based on soft lithography for large-scale soft electronics. By combining the additive and subtractive patterning techniques with 3D integration, skin-mountable, soft microsystems are demonstrated to highlight high-density fabrication and integration capabilities.

Chapter 4 presents a nanofabrication process to create submicron-scale soft electronic devices by combining electron-beam lithography for micro/nanostructure fabrication and soft lithography for EGaIn stamping. The proposed hybrid lithography enables high resolution and high density soft electronic devices. For the first time, submicron-scale EGaIn thin film patterning with feature sizes as small as 180 nm is demonstrated.

Chapter 5 describes 3D-integrated, all-soft physical strain sensing microsystems, which are composed of a soft sensor, a soft interconnector, and a soft readout circuit, by utilizing the reverse stamping process and the 3D integration technique. Two types of soft

physical microsystems are investigated: (i) a finger-mountable strain sensing microsystem and (ii) a fingertip microsystem for simultaneous proximity, touch, and pressure sensing.

Chapter 6 introduces all-soft chemical sensing platforms for detection of liquid-phase and gas-phase volatile organic compounds (VOCs) using the same device and demonstrates battery-free and wireless sensing using a 3D-integrated, inductive-capacitive (*LC*) sensor and a soft readout coil. Again, the sensing platforms are enabled by utilizing the subtractive reverse stamping process and the 3D integration technique.

Chapter 7 introduces all-soft energy storage devices for powering wearable and skin-mountable electronics and demonstrates soft supercapacitor based on CNT-integrated EGaIn electrodes. EGaIn electrodes are fabricated by utilizing the additive stamping process and functionalized with CNT via a layer-by-layer (LBL) adsorption technique.

Chapter 8 summarizes the contributions of this work and outlines avenues of potential future research.

CHAPTER 2. MICROSCALE LIQUID METAL THIN-FILM PATTERNING USING SUBTRACTIVE REVERSE STAMPING TECHNIQUE BASED ON SOFT LITHOGRAPHY

2.1 Motivation

For the fabrication of EGaIn-based soft electronics, EGaIn is patterned on an elastomeric substrate, such as PDMS, and subsequently sealed with an additional PDMS cover [13, 26]. Such a process can form all-soft and stretchable electronic elements because the liquid nature of EGaIn maintains electrical functionality during mechanical deformation, such as bending, twisting, or stretching. However, technical challenges remain to make all-soft and functional microelectronics a reality and are briefly discussed in the following.

One of the primary technical hurdles associated with EGaIn-based microelectronics is the difficulty to pattern fine features without residue because EGaIn adheres to most surfaces thanks to the oxide layer on the surface, and thus generates unwanted EGaIn residue [25]. Moreover, it is challenging to achieve uniform and smooth thin films because of the high surface tension and unique wetting properties of EGaIn in air [26]. Therefore, patterning fine, uniform, and smooth EGaIn lines without residue remains challenging.

Another technical challenge for flexible and stretchable electronics is ability to vertically integrate multiple layers to enhance functionality and performance [77]. In silicon technology, through-silicon vias (TSVs) represent a well-established technology for vertical integration [78]. However, no equivalent process exists for flexible and stretchable electronics. Therefore, although stretchable electronic elements in a single layer have been

presented, integration of all-soft electronic components via vertical interconnects has not yet been demonstrated.

In this chapter, a process to create size-scalable and high-density soft passive components using subtractive reverse stamping based on soft lithography is demonstrated [79, 80]. The proposed fabrication process addresses the challenges of high-resolution, size-scalable, uniform, and residue-free EGaIn thin-film patterning ranging from single micrometers to several millimeters in line width at room temperature and in ambient pressure. In addition, EGaIn-filled, soft through-PDMS vias (sTPVs) are investigated to address the integration challenges by providing multilayer vertical interconnection.

2.2 Subtractive Reverse Stamping Technique Based on Soft Lithography

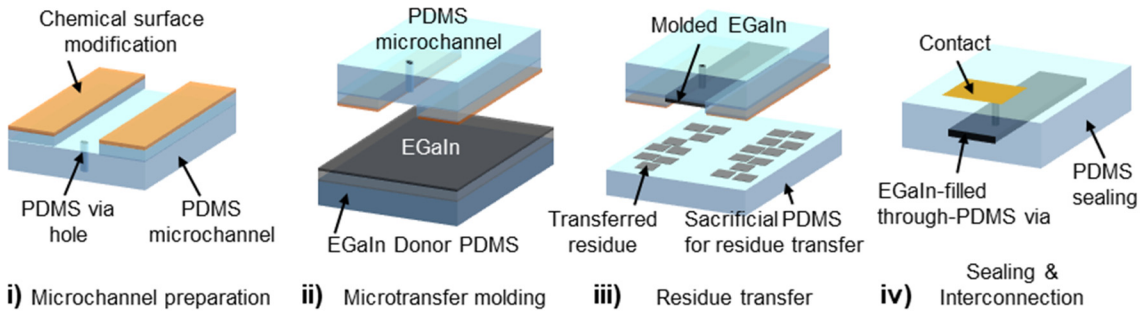

Figure 2.1 Subtractive reverse stamping process based on soft lithography for scalable, uniform, and residue-free EGaIn thin-film fabrication.

Figure 2.1 provides a schematic diagram of the proposed subtractive reverse stamping process based on soft lithography for scalable, uniform, and residue-free EGaIn thin-film fabrication. The advanced liquid metal patterning process consists of four steps: i) selective chemical surface modification of the PDMS mold, ii) microtransfer molding of EGaIn, iii) residue transfer, and iv) sealing and vertical interconnection. The fabrication

process starts with the selective chemical surface modification of a PDMS mold with embedded 5 μm deep concave microchannels, fabricated using a normal replica molding process. The surface of the PDMS mold is chemically modified using toluene for selective wetting (Figure 2.1-i). This selective chemical surface modification process increases the hydrophobicity compared to the non-modified PDMS surface. The surface energy of the modified PDMS surface was measured to be ≈ 12-18 mJ m^{-2} using a contact angle measurement system (Ramé-hart, Model 250 goniometer), compared to ≈ 22-25 mJ m^{-2} for non-modified surfaces. In the next step (Figure 2.1-ii), the PDMS mold is pressed onto a donor PDMS substrate coated with the EGaIn film and separated from it. Because of the initial surface modification, any unwanted liquid metal residue outside of the channel areas can now be effectively transferred to a higher-surface-energy (non-modified) sacrificial PDMS substrate (Figure 2.1-iii). This process is repeated several times until all liquid metal residue is removed. Finally, the PDMS mold with liquid-metal-filled channels is covered with an additional PDMS layer. For vertical interconnection, the PDMS mold or the additional PDMS layer has embedded liquid-metal-filled through-PDMS vias, fabricated using a normal replica molding process or a PDMS punch and filled using the same reverse stamping process (Figure 2.1-iv). The detailed fabrication process of the subtractive reverse stamping including detailed material information is described in Appendix A1.

Resulting patterned EGaIn lines with widths ranging from 2 μm to 200 μm and inter-channel spacings ranging from 2 μm to 100 μm without EGaIn residue are shown in Figure 2.2 (a)-(d). Figure 2.3 (a) shows 50 μm wide EGaIn lines and the surrounding PDMS surfaces with and without the chemical surface modification and residue transfer technique. Using the surface modification and residue transfer technique, essentially all EGaIn residue

formed on the outside of the channel surface could be effectively transferred, and the patterned EGaIn lines show smooth surfaces and uniform thickness inside the PDMS mold. Figure 2.3 (b) shows the measured EGaIn thickness inside of the PDMS mold as a function of PDMS channel width. The measured EGaIn thickness was 309±54 nm and 1.10±0.18 μm for a channel width of 50 μm and 5 μm, respectively. The decreasing film thickness with increasing channel widths can be explained by the deformation of the PDMS mold under applied pressure during the molding process [81]. The deformation of the PDMS mold during the process has been shown to yield EGaIn thin films and smooth surfaces with sharp edges and a uniform thickness compared to other EGaIn patterning methods previously demonstrated [11, 26]. Figure 2.3 (c) shows the cross-sectional view of a EGaIn molded microchannel. The patterned EGaIn thin line is uniformly molded in the microchannel after being covered with an additional PDMS.

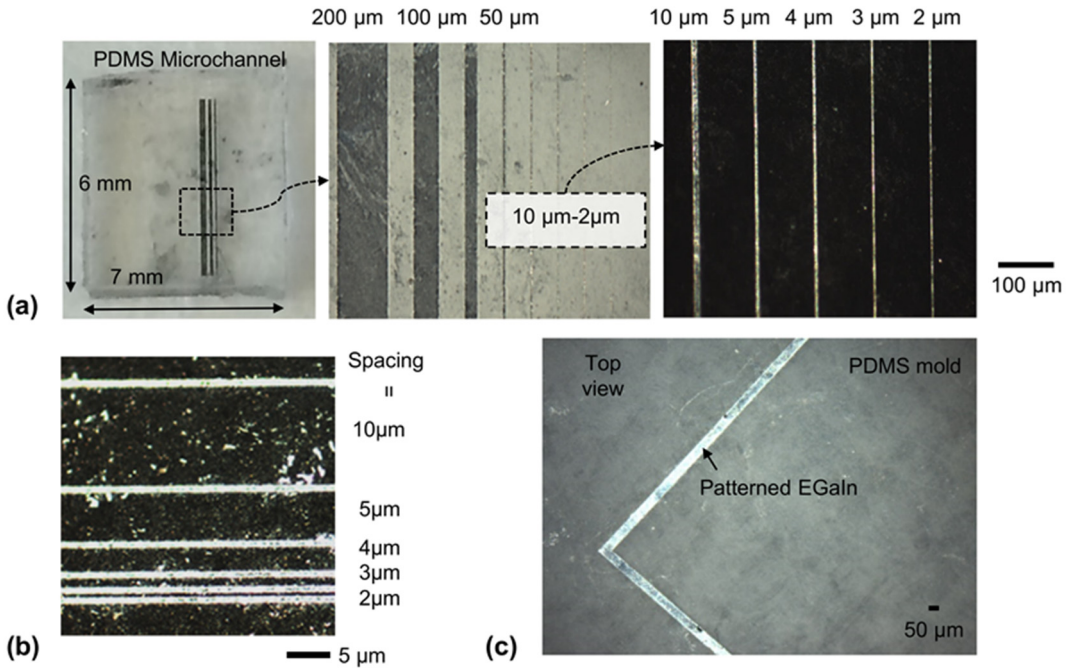

Figure 2.2 (a) Patterned EGaIn lines with widths from 2 μm to 200 μm at inter-channel spacings of 100 μm and (b) spacings from 2 μm to 10 μm; (c) Soft circuit demonstration with a conductor line with 50 μm without liquid metal residue outside of the channel region.

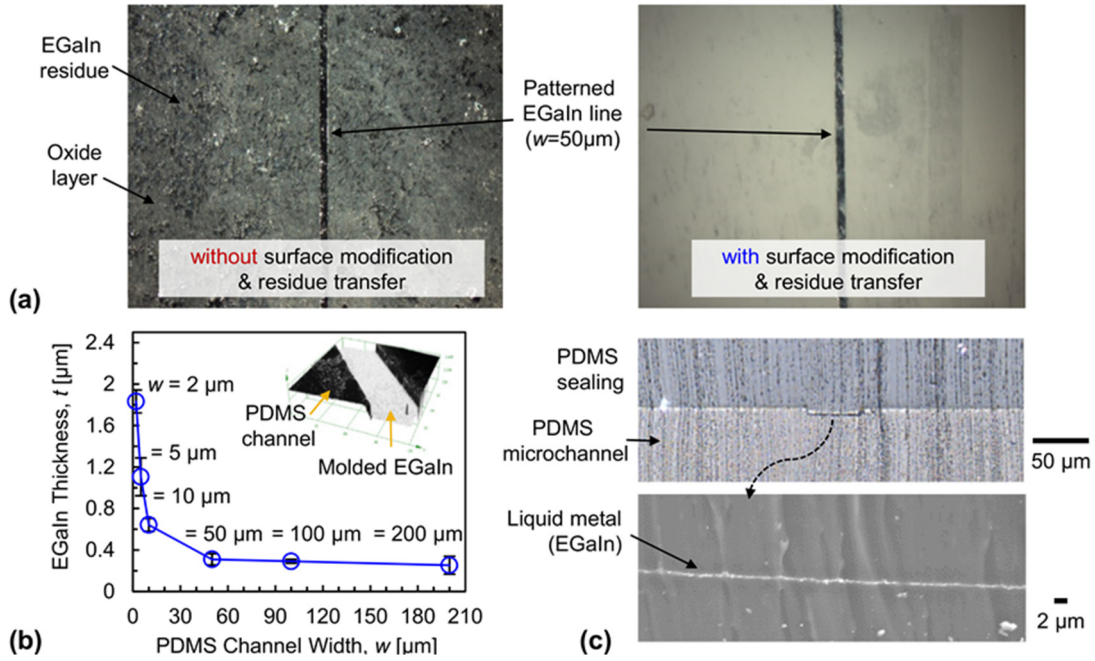

Figure 2.3 (a) EGaIn patterns and surrounding PDMS surfaces with and without chemical surface modification and residue transfer technique for residue-free surfaces; (b) Measured EGaIn thickness inside of a PDMS mold as a function of PDMS channel width; (c) Cross-sectional view of an EGaIn molded microchannel having 50 μm in width and 5 μm in thickness (top) and enlarged view of the molded EGaIn thin film having 300 nm thickness (bottom).

2.3 Microscale Soft Passive Electronic Devices

2.3.1 Design, Fabrication, and Electrical Characterization

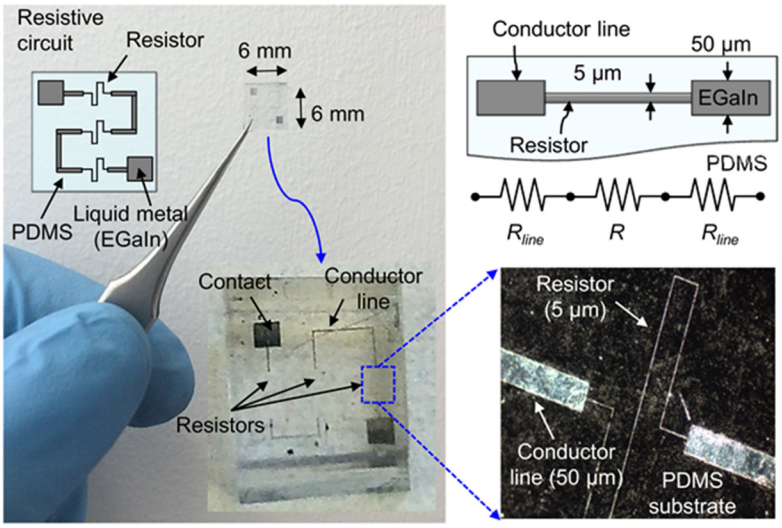

Figure 2.4 EGaIn-based soft circuit with three embedded resistors (5 μm width) connected with conductor lines (50 μm width).

Based on this proposed fabrication process, the electrical characteristics and performance of fabricated all-soft, passive components were investigated. Figure 2.4 shows a simple circuit with embedded resistors. This soft circuit has three serial resistors with 5 μm width, and the resistors are connected with 50 μm wide conductor lines. The resistance $R = \rho L/A$ is determined by the resistivity ρ of the conductive material as well as the cross-sectional area A and the length L. The thin-film resistivity of EGaIn is identical to its resistivity (electrical resistivity $\rho = 29.4\times10^{-8}\,\Omega$ m) [37]. The cross-sectional area of the resistor and the conductor line were designed and fabricated to have 5 μm width with 1 μm thickness and 50 μm width with 300 nm thickness, respectively. Thus, the channel length is the main design parameter to determine the resistance of the line.

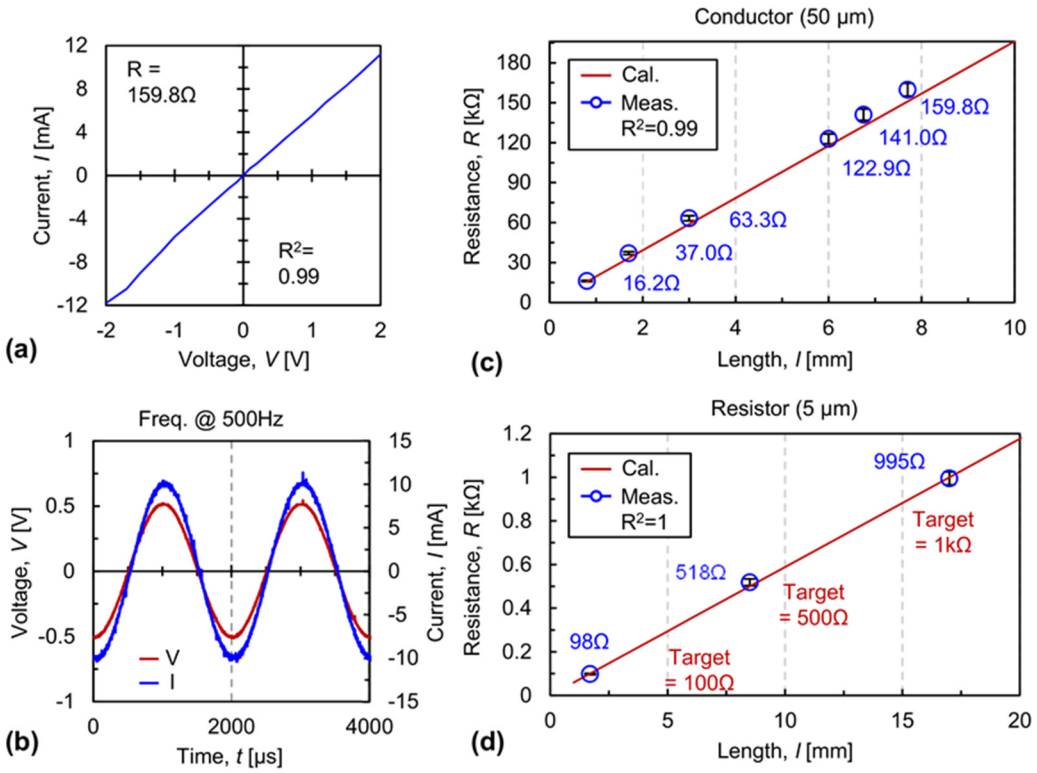

Figure 2.5 (a) DC characterization and (b) AC characterization of conductor lines; Calculated and measured resistance of (c) conductor lines and (d) resistors as a function of the channel length.

Initially, the DC and AC electrical characteristics of the resistors were investigated. The DC *I-V* curve for the conductor line (50 μm width) is shown in Figure 2.5 (a), exhibiting an ohmic behavior with <5.8% deviation between the calculated and measured values. For the AC electrical characterization, a sinusoidal voltage (±0.5 V at 500Hz) was applied to the conductor line. The measured resistance again agreed well with the calculated value, exhibiting <2.1% deviation between calculated and measured values and, as expected, no phase shift between current and voltage, as shown in Figure 2.5 (b). Then, the resistance of the 50 μm wide conductor lines was measured as a function of the channel length. The measured resistance scaled linearly with the channel length with <6.5% deviation compared to calculated values as shown in Figure 2.5 (c). The serpentine-shaped

resistors (5 μm width) were designed and fabricated to have a target resistance of 100 Ω with 1.7 mm length, 500 Ω with 8.5 mm length, and 1 kΩ with 17 mm length. Similar to the conductor lines, they exhibited highly linear *I-V* characteristics, and resistance values matched the calculated value as shown in Figure 2.5 (d). These results demonstrate the possibility to design soft circuits with embedded serial and/or parallel soft resistors.

2.3.2 Mechanical Characterization

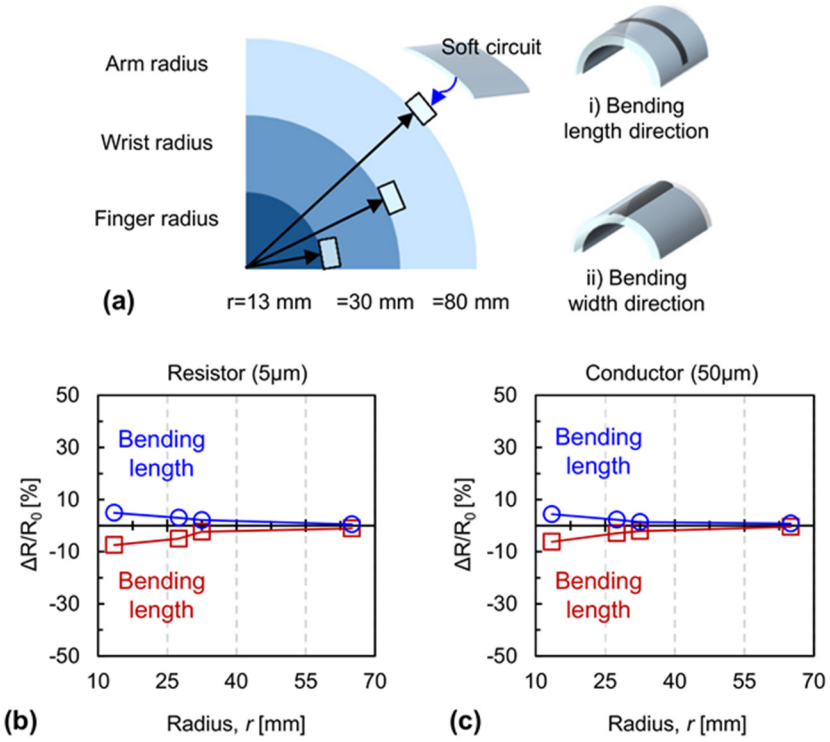

Figure 2.6 (a) Illustration of bending characterization with various sizes of circular cylinders for wearable electronics applications; Measured relative resistance changes of (b) resistors and (c) conductor lines, subject to bending along the length direction or width direction, as a function of the radius of curvature.

One of the main requirements for soft microelectronics is to maintain their electronic functionality during deformation [8]. To demonstrate this, the electrical behavior of EGaIn-based soft circuits was experimentally investigated by applying bending and

twisting forces. Different sizes of circular cylinders were prepared to simulate typical bending radii of fingers (radius < 30 mm), wrists (≈ 80 mm), and arms (> 80 mm), as shown in Figure 2.6 (a). The resistor embedded in a PDMS chip with overall dimensions of 50 mm (w) × 50 mm (l) × 2 mm (t) was attached to the surface of the circular cylinders to measure the relative resistance changes $\Delta R/R_0$, where ΔR is the difference in resistance after and before bending, and R_0 is the initial resistance before bending. Figures 2.6 (b) and (c) show the measured relative resistance changes of the resistor (5 μm width) and the conductor line (50 μm width) as a function of the radius of curvature. As the radius of curvature becomes smaller, the relative resistance changes gradually increased to 4.9% by bending the resistor along the length direction but decreased to -7.4% by bending it along the width direction in the case of the minimal radius of curvature of 13.5 mm (Figure 2.6 (b)). Overall, the observed relative resistance changes for the resistors are below ±4% for radii of curvature larger than 27.5 mm and below ±1% for radii of curvature over 65 mm. The relative resistance changes for the conductor line show similar behavior (Figure 2.6 (c)).

The change of resistance upon bending can be understood by considering the effect of geometry changes of the resistor: bending along the length direction increases the resistor length (while simultaneously decreasing its width and thickness), thus resulting in a resistance increase. Bending along the width direction, on the other hand, increases the resistor width (while simultaneously decreasing its length and thickness), yielding a decrease in resistance. To estimate the direction and magnitude of the resistance change, finite element simulations were conducted in COMSOL Multiphysics (COMSOL Inc., Burlington MA) using the fluid-structure interaction physics, with the liquid metal being

fully surrounded by the PDMS chip. To simulate the bending, the PDMS chip (10 mm (*w*) × 10 mm (*l*) × 2 mm (*t*)) with the embedded channel is conformally wrapped around the surface of the circular cylinders using a prescribed displacement in both length and width direction. In addition, boundary loads are applied to the outer faces of the chip in the direction of the bending to ensure that the interface to the circular cylinder is stress-free (see Figure 2.7 (a) and (b)).

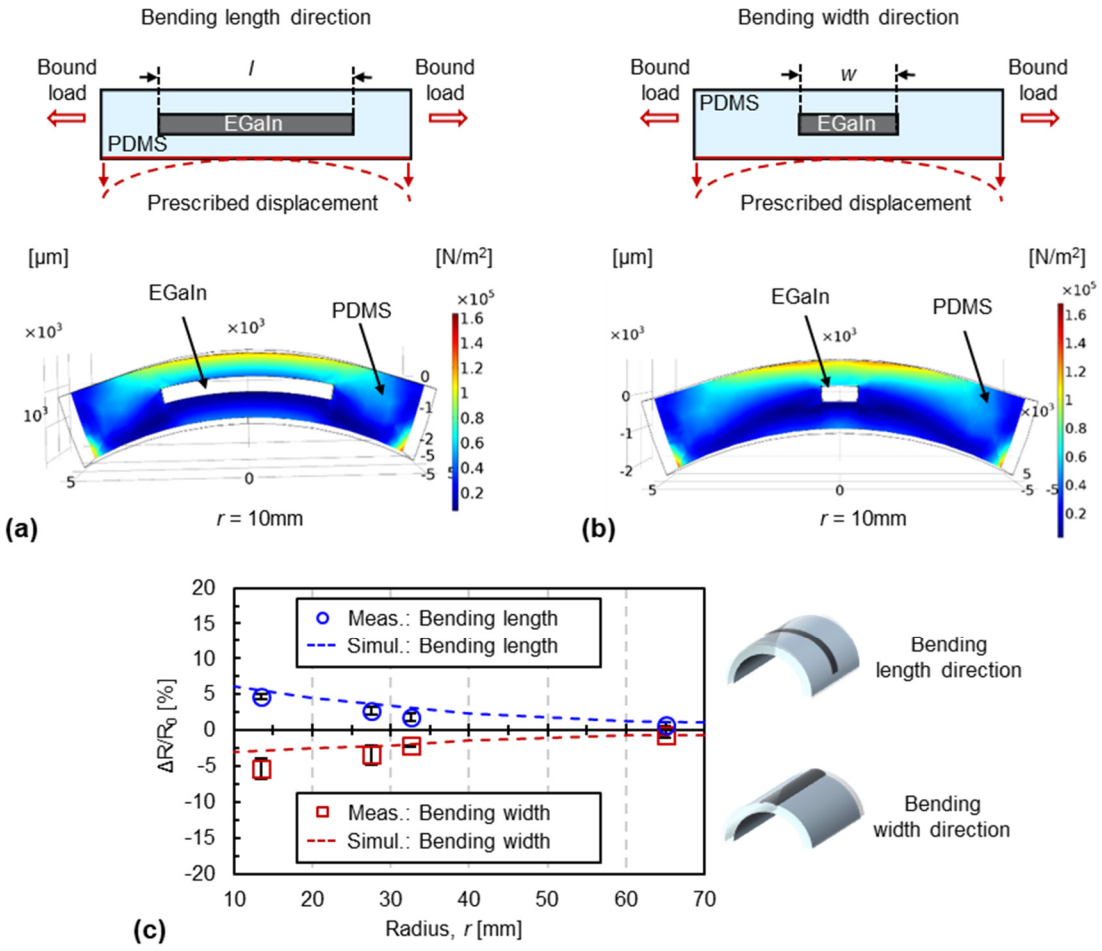

Figure 2.7 Finite element simulations of test chip bending over a 10 mm radius circular cylinder along the (a) length direction and the (b) width direction of the EGaIn-filled microchannel; (c) Comparison of simulated and measured relative resistance changes as a function of the radius of curvature.

Figures 2.7 (a) and (b) show the simulated deformed PDMS upon bending to conform to a 10 mm radius circular cylinder in length and width direction of the microchannel, respectively. Figure 2.7 (c) compares the resulting simulated relative resistance change with the experimental data. It exhibits a similar increasing (by bending along the length direction) and decreasing (by bending along the width direction) tendency as the bending radius becomes smaller. The measured relative resistance changes agreed well with the simulated values with <26% deviation. It is believed that the simplified simulation model, which does not consider the through-PDMS vias of the actual test chip, and the experimental error are the reason for this difference.

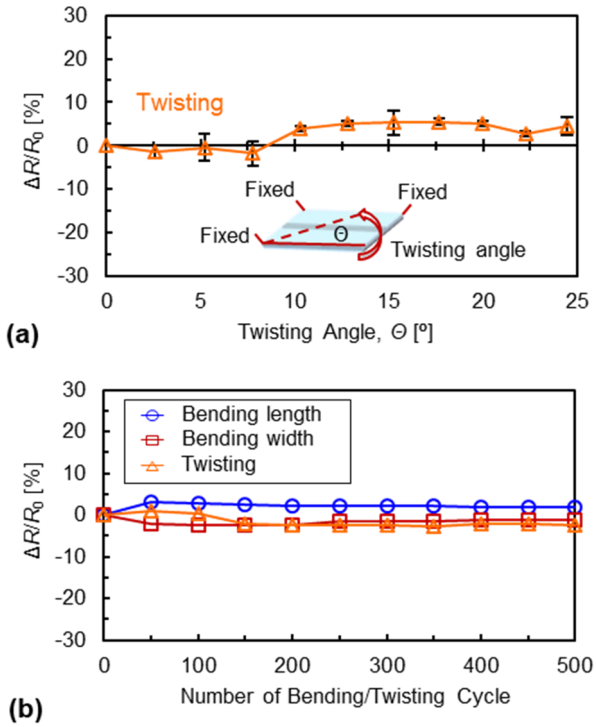

Figure 2.8 (a) Measured relative resistance changes as a function of applied torsion angles; (b) Relative resistance changes as a function of the number of subsequent bending and twisting cycles (bending was performed around a cylinder with 13.5 mm radius, and twisting was performed to a 25˚ angle).

To investigate the twisting behavior, twisting forces were applied to the same soft circuit. Figures 2.8 (a) show the measured relative resistance changes as a function of the twisting angle, indicating <4.2% resistance change on both the resistor and conductor line. Twisting has a minor effect on the resistance because the original resistor shape of the channel is largely maintained under twisting deformation [82]. Finally, as a simple reliability test, the relative resistance changes as a function of the number of bending and twisting cycles were measured (see Figure 2.8 (b)), with less than ±2.3% resistance change up to 500 bending or twisting cycles.

2.3.3 Soft Passive Energy Storage Devices

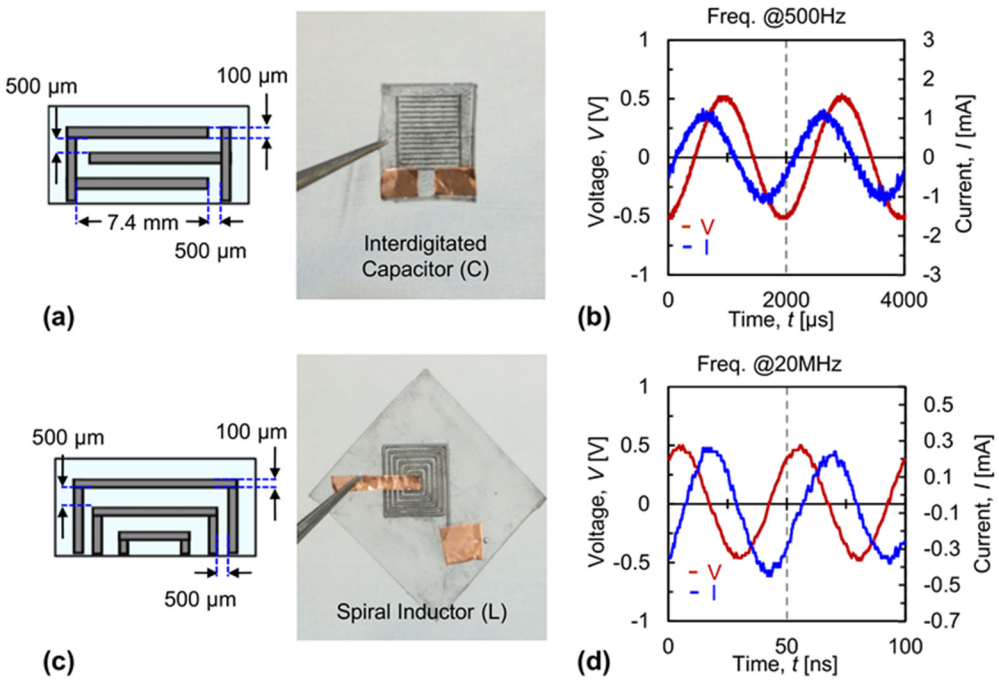

Figure 2.9 (a) Schematic illustration and fabricated interdigitated capacitor; (b) AC characterization of the fabricated interdigitated capacitor; (c) Schematic illustration and fabricated planar spiral inductor; (d) AC characterization of the fabricated rectangular spiral inductor.

Passive energy storage components, namely interdigitated capacitors and planar spiral inductors, were also designed and fabricated using the same patterning process, and subsequently electrically characterized. The capacitor comprises 15 interdigitated electrodes (IDEs) with 100 μm width and 7.4 mm length with an electrode spacing of 500 μm (see Figure 2.9 (a)). As expected, the fabricated interdigitated capacitor acts like an open circuit at DC, and an applied alternating voltage (±0.5 V at 500Hz) lags the current by 90°, as shown in Figure 2.9 (b). The fabricated rectangular spiral inductor has 5 turns with a line width of 100 μm and a line spacing of 500 μm width (see Figure 2.9 (c)). The fabricated planar spiral inductor acts like a short circuit at DC, and an applied alternating voltage (±0.5 V at 20MHz) leads the current by 90° as shown in Figure 2.9 (d). Using these fundamental RLC elements, different types of EGaIn-based soft circuits can be designed. Further electrical characteristics of the fabricated interdigitated capacitors and planar spiral inductors will be discussed in Chapter 6.

2.4 Vertical Integration using EGaIn-Filled Soft Vias

Incorporating EGaIn-filled soft vias, so-called soft through-PDMS vias or sTPV, facilitates high-density integration as well as system-level flexibility and stretchability. Figure 2.10 (a) shows the schematic of and fabricated sTPVs of various via sizes. The PDMS-through vias were compactly filled with liquid metal using the same patterning process. The smallest via diameter was 350 μm, and the largest via diameter was 1.2 mm, yielding an aspect ratio (AR) ranging from 1.7 to 5.7. Figure 2.10 (b) shows the calculated and measured resistance of the sTPVs in the mΩ range for various diameters. Vertical soft

circuit integration was demonstrated using a resistor circuit with sTPVs, as shown in Figure 2.10 (c). Because of the self-healing characteristics of EGaIn, this vertical integration scheme enables novel 3D structures by stacking layers on each other for vertical integration.

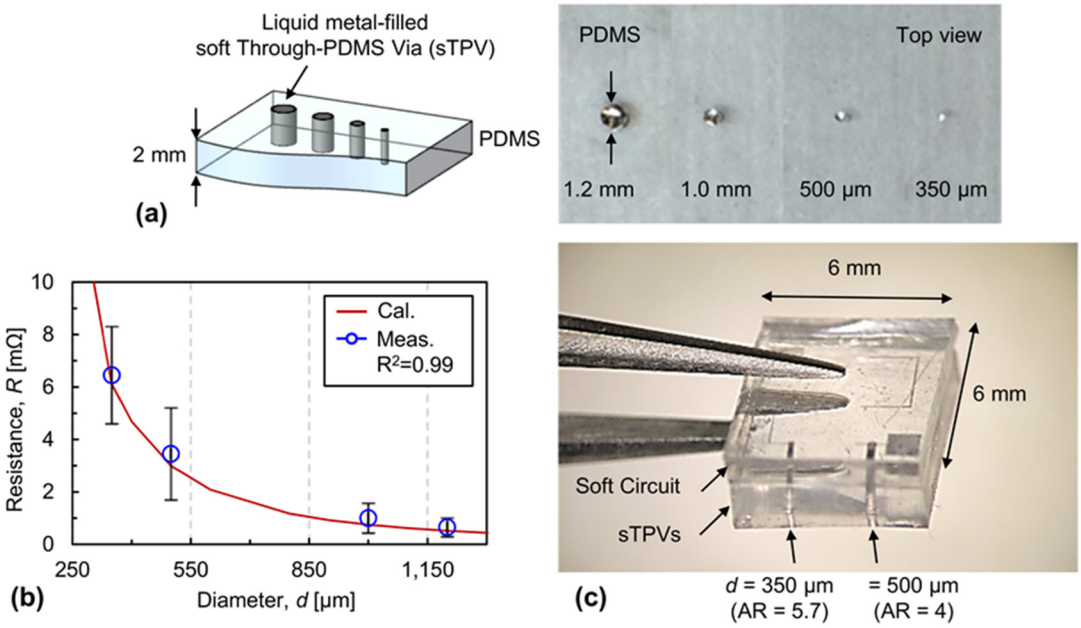

Figure 2.10 (a) Schematic of and fabricated EGaIn-filled soft vias with various diameters from 1.2 mm (aspect ratio (AR) = 1.7) to 350 µm (AR = 5.7); (b) Calculated and measured resistance of sTPVs as a function of the via diameters; (c) Demonstration of vertical soft circuit integration using a resistor-embedded circuit and sTPVs.

To demonstrate potential applications for soft microelectronics, 2.5D and 3D vertical soft circuit integration schemes were investigated and are shown in Figures 2.11 (a) and (b), respectively. Figure 2.11 (c) shows a LED circuit with embedded resistors that integrates two commercial LEDs. Using a 2.5D integration scheme, two LEDs were attached on top of the substrate using sTPVs, and the circuit layers were vertically stacked using alignment marks for multilayer integration. A voltage was supplied to the circuit through probe tips, and the circuit was operated under bending and twisting deformation

(Figure 2.11 (d)). Vertical multilayer interconnection based on sTPVs is one of the potential primary approaches for high-density soft microelectronics. Figure 2.11 (e) shows the 3D integrations scheme, which consists of five layers in total (two LED circuits and three sTPV layers). The diameter of the sTPVs was 1 mm with 1 mm thickness, and all PDMS layers were bonded after oxygen plasma treatment.

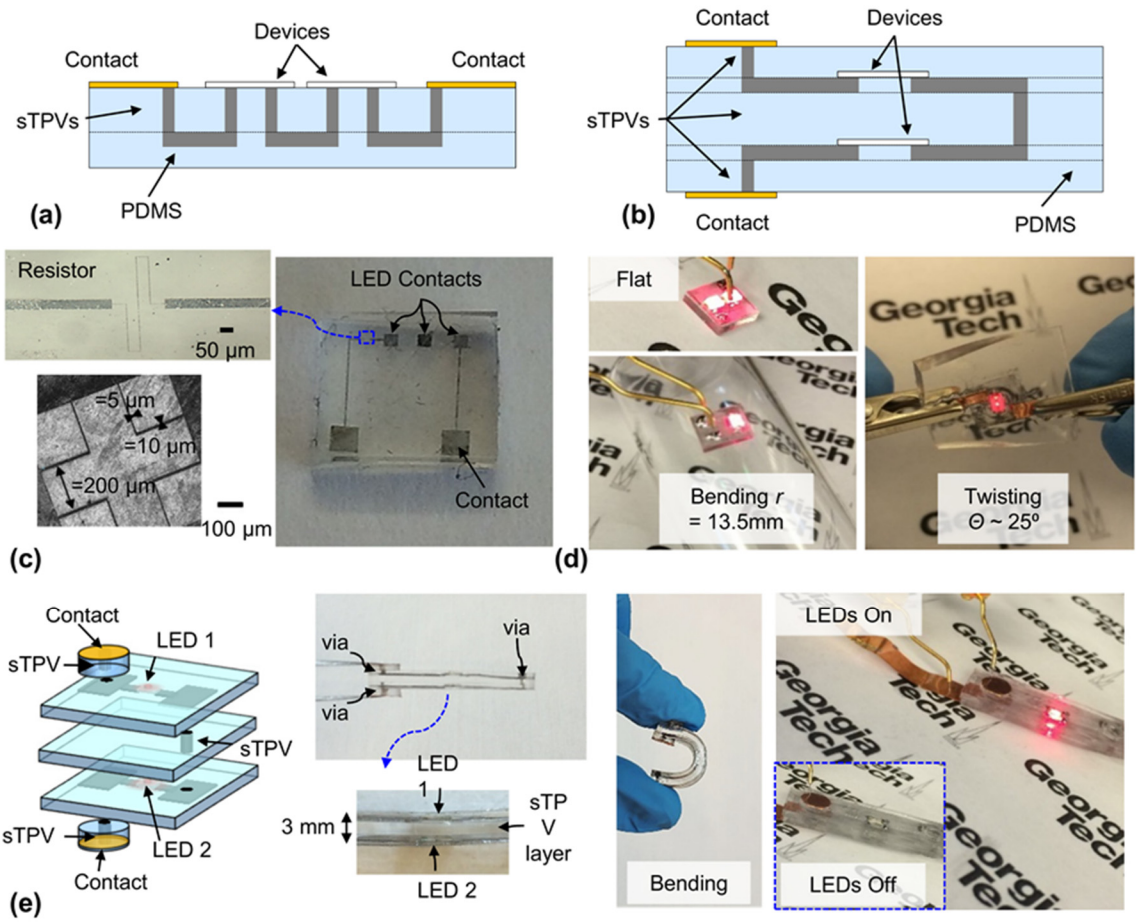

Figure 2.11 Schematic for (a) 2.5D and (b) 3D vertical soft circuit integrations; (c) Fabricated LED circuit with embedded resistors as 2.5D integration demonstration; (d) LED circuit operation under bending and twisting deformation; (e) 3D integration of LED circuit with sTPVs for multilayer interconnection.

The vertical integration scheme can facilitate system-level flexibility and stretchability. Figure 2.12 (a) shows an LEDs array circuit subjected to bending, twisting,

and stretching forces. Figure 2.12 (b) shows the relative resistance changes of a conductor line as a function of applied strain. As expected, $\Delta R/R_0$ linearly increase because of the geometry changes. The circuit withstood large deformations (≈ 35% strain) while maintaining its electrical functionality. Furthermore, we demonstrated a bandaid integration with the soft LED circuit attached to a finger or an arm, shown in Figure 2.12 (c), which again demonstrates its electrical functionality on non-planar objects. These results demonstrate that the soft microelectronic circuits are electrically functional under deformation and can potentially be applied to all-soft wearable electronics for healthcare, food, and environmental monitoring.

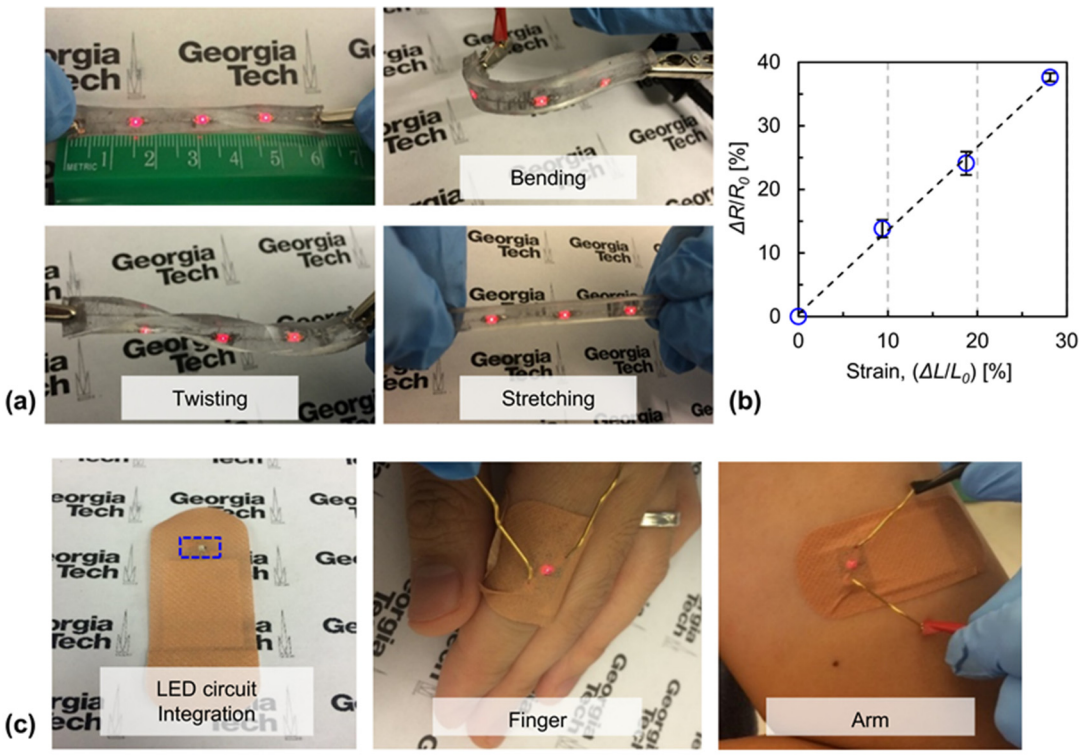

Figure 2.12 (a) Demonstration of system-level flexibility and stretchability by applying bending, twisting, and stretching forces; (e) Relative resistance change of conductor line as a function of applied strain; (c) Demonstration of system-level flexibility and stretchability: a soft LED circuit integrated with a bandaid is attached to a human finger and arm to highlight a wearable electronics application.

2.5 Conclusion

This chapter introduces microscale EGaIn thin-film patterning and vertical integration techniques for 3D-integrated, all-soft microelectronics. A subtractive reverse stamping technique based on soft lithography is developed allowing line width ranging from single micrometers to several millimeters to enable all-soft electronic passive components and circuits, as well as vertical integrations. The soft electronic devices remain functional under bending, twisting, and stretching deformations. Based on the demonstrated fundamental building blocks, more sophisticated, soft hybrid electronics can be built for a wide variety of applications.

CHAPTER 3. LARGE-SCALE LIQUID METAL THIN-FILM PATTERNING USING ADDITIVE STAMPING TECHNIQUE BASED ON SOFT LITHOGRAPHY

3.1 Motivation

The subtractive reverse stamping technique based on soft lithography introduced in Chapter 2 demonstrated high-resolution and size-scalable EGaIn patterns from 2 μm to 1–2 mm in line width. However, for channel widths > 2 mm, EGaIn is not effectively transferred to the inside of the PDMS channels because of the sagging deformation of wide channels during the pressure-based molding process. Therefore, the pattern dimensions, in particular line widths achievable using the subtractive reverse stamping approach are limited to the single μm to a couple of mm scale. This difficulty to define large patterns initiated the development of a uniform, large-area EGaIn thin-film patterning technique for large-scale (mm-cm) soft electronics fabrication, such as soft printed circuit boards (sPCB) and soft energy storage devices.

In general, stamping lithography offers a simple, fast, and low-cost way to print large-area patterns [81]. In case of the EGaIn, the oxide layer on the EGaIn surfaces interferes with uniform wetting on soft elastomeric substrates, typically resulting in non-uniform thickness and rough surfaces [32]. Therefore, stamp lithography for the use of EGaIn has often been regarded as the lowest resolution and least reliable technique among the additive printing methods [26, 32, 83].

In this chapter, large-area and uniform EGaIn thin-film patterning using an additive stamping process is demonstrated for large-scale (mm - cm) soft electronic devices. By

utilizing a physical surface modification, the PDMS substrate surface can be modified to have uniform wetting properties for EGaIn. In addition, by combining structures fabricated using the demonstrated additive and subtractive stamping techniques via 3D heterogeneous integration, functional soft microsystems are demonstrated [84, 85].

3.2 Additive Stamping Technique Based on Soft Lithography

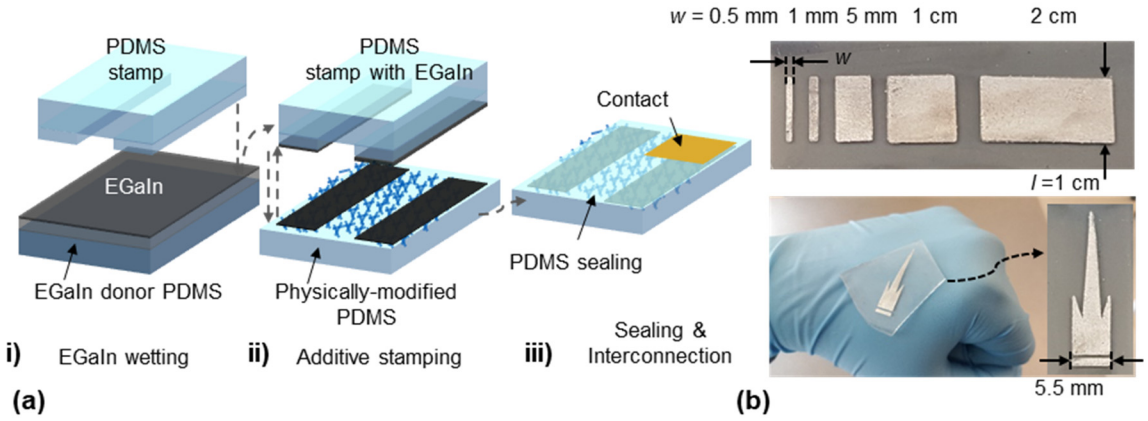

Figure 3.1 (a) Additive stamping process based on soft lithography for centimeter-scale EGaIn patterning on a physical-surface-modified PDMS substrate; (b) Patterned EGaIn lines and Georgia Tech tower to demonstrate large-area EGaIn patterning with 500 µm resolution.

Figure 3.1 (a) illustrates the additive stamping approach for large-area, centimeter-scale EGaIn patterning relying on physical surface modification of the PDMS substrate. Thereby, a proper physical surface modification provides uniform wetting properties, which enables transfer of uniform and residue-free EGaIn thin films. The physical surface modification creates a paper-textured PDMS surface [86, 87], which increase the surface areas and, thus, adhesion forces, and ultimately enhances the wettability to enable printing of uniform and smooth EGaIn thin films using the additive stamping process. The

underlying liquid metal patterning process mainly consists of three steps: i) EGaIn wetting on a PDMS stamp, ii) EGaIn transfer using additive stamping, and iii) sealing and interconnection. The fabrication process starts with the PDMS stamp preparation and wetting EGaIn on the PDMS stamp (Figure 3.1 (a)-i). The PDMS mold/stamp is then gently pressed onto a donor PDMS substrate coated with EGaIn and separated from it (Figure 3.1 (a)-ii). During the molding process, EGaIn adheres to all surfaces of the PDMS stamp, including the concave channels and protruding surface areas. In the next step, the PDMS stamp wet with EGaIn is stamped onto a PDMS substrate with a physically modified surface to deposit a patterned EGaIn film. Finally, the resulting transferred pattern is covered with an additional PDMS layer by either casting or spin coating (Figure 3.1 (a)-iii). The additive stamping approach provides large-area EGaIn patterns with 500 µm resolution, as shown in Figure 3.1 (b). The detailed fabrication process of the additive stamping and material information are described in Appendix A.2.

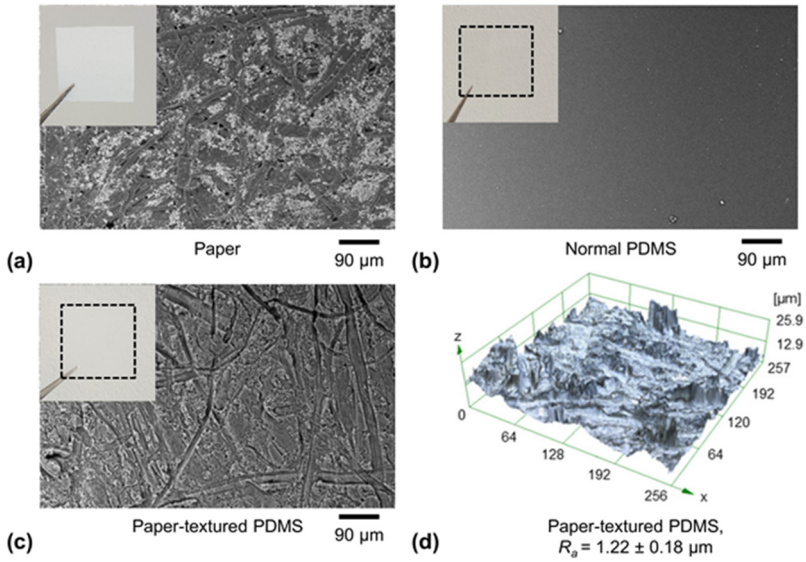

Figure 3.2 SEM images of (a) paper, (b) normal PDMS, and (c) paper-textured PDMS surfaces; d) 3D image of the paper-textured PDMS surface.

To achieve uniform large-area EGaIn patterns, the PDMS stamp wet with EGaIn is stamped onto a PDMS substrate with a paper-textured surface. To this end, regular paper texture, which comprises randomly distributed micro cellulose fiber structures (Figure 3.2 (a)), is transferred to a PDMS surface using a conventional PDMS casting method. The resulting paper-texture PDMS exhibits a surface microstructure which allows it to wet with EGaIn compared to a normal, smooth PDMS surface (Figure 3.2 (b)-(d)). As a result, continuous EGaIn films can be effectively transferred to paper-textured PDMS using multiple stamping steps. The smallest EGaIn feature sizes realized this way were w = 500 μm in width and $t \approx 1.5$ μm in thickness (with 5 times stamping). While this additive stamping process shows relatively poor lateral resolution, it is suitable for large-area patterning and thin-film deposition and thus can complement the high-resolution, subtractive reverse stamping process described in Chapter 2.

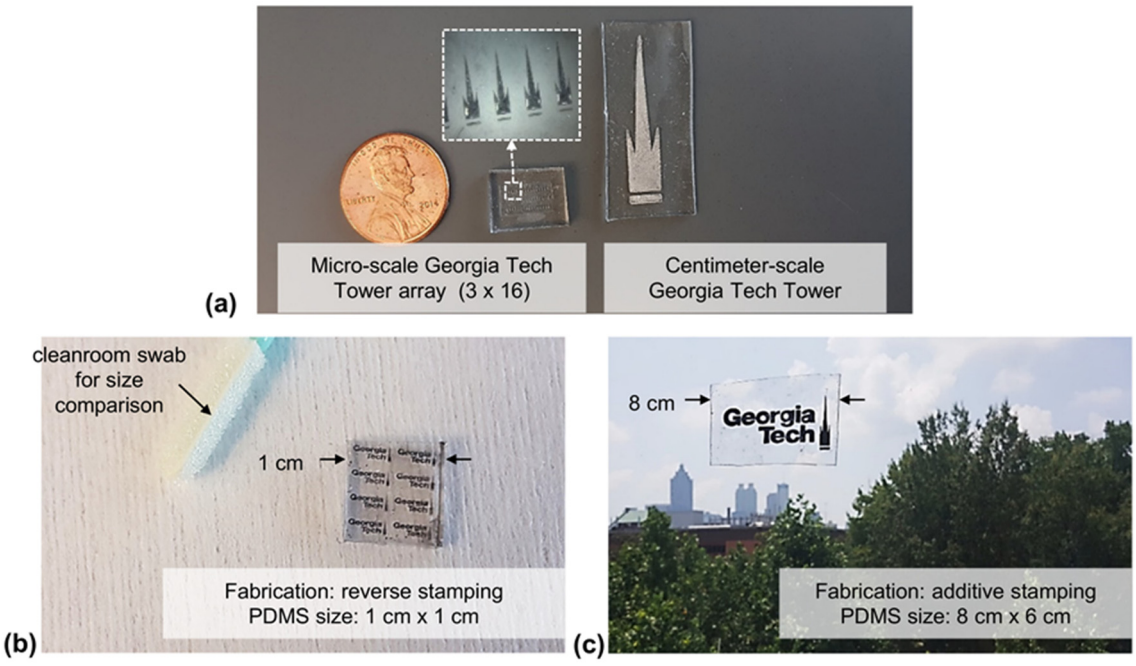

Figure 3.3 (a) Comparison of EGaIn-based microscale and centimeter-scale Georgia Tech towers fabricated using (b) the subtractive reverse stamping and (c) the additive stamping approaches.

To demonstrate the multiscale patterning capability of both processes, we fabricated EGaIn-based microscale and centimeter-scale versions of the Georgia Tech tower logo using the subtractive and additive approaches, respectively (Figure 3.3 (a)): on one hand, a microfabricated PDMS mold with a 3 × 16 array of Georgia Tech towers with a critical dimension of 2 μm and, on the other hand, a stamped version of the Georgia Tech tower on a PDMS substrate with critical dimensions of ≈ 500 μm are prepared, which is ×23 wider in length and ×529 larger in area compared to the microfabricated PDMS mold. The resulting patterns using both additive and subtractive methods show uniform and smooth EGaIn films with sharp edges, spanning lateral dimensions from single micrometers to centimeters, which demonstrates the complementary nature of both fabrication processes (Figure 3.3 (b)-(c)).

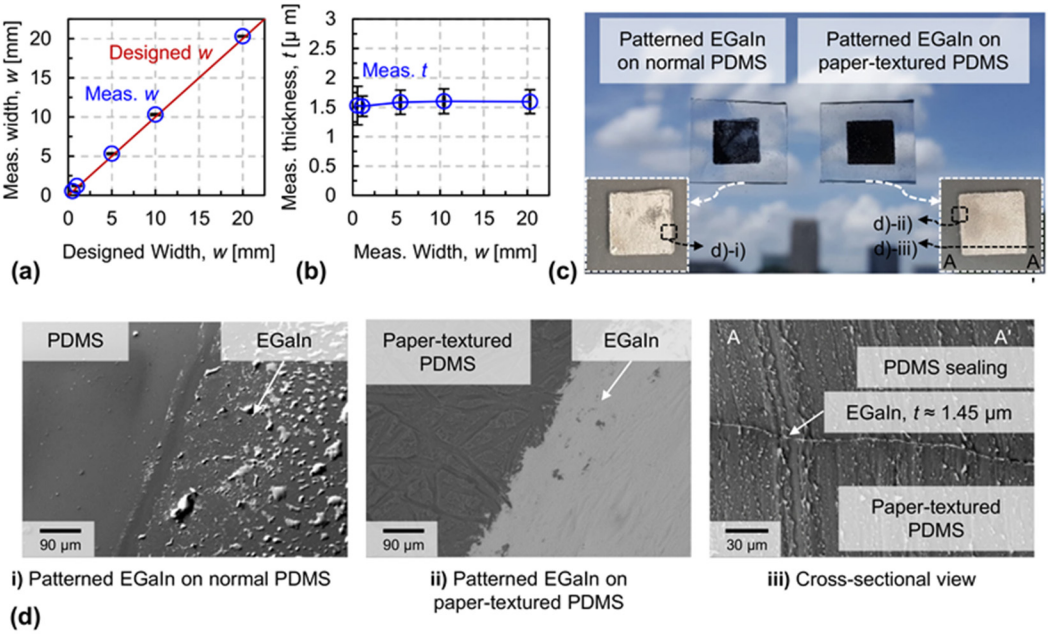

Figure 3.4 Characterization of patterned EGaIn thin films fabricated using the additive stamping approach: (a) measured EGaIn pattern width as a function of designed stamp width and (b) resulting film thickness as a function of patterned EGaIn width; (c)-(d) patterned EGaIn films on normal and paper-textured PDMS surfaces, and cross-sectional view of patterned EGaIn film on paper-textured PDMS after sealing with an additional PDMS layer.

Figure 3.4 highlights the characterization of patterned EGaIn thin films based on the additive stamping technique. Figure 3.4 (a) and (b) show the measured EGaIn width as a function of the designed stamp width and the resulting film thickness as a function of the patterned EGaIn width, respectively. PDMS stamps with > 500 μm in width and 10 mm in length (Figure 3.1 (b)) were prepared and stamped 5 times (alignment done under a stereo microscope) on the paper-textured PDMS substrates. Thereby, stamping 5 times is the optimized number of stamping steps to achieve smooth and uniform films (Figure 3.5)). The tested smallest feature was 500 μm, and the patterned EGaIn lines showed reliable and uniform line width with on average <6.5% deviation from the designed PDMS width. This deviation can be explained by the deformation of PDMS elements during the stamping process as well as the misalignment during multiple stamping processes. The resulting film thickness after 5 times stamping was 1.56 ± 0.22 μm over the range of patterns tested. The uniform EGaIn thin film formation using the additive stamping approach is made possible thanks to the physical surface modification and the multiple stamping processes.

To evaluate the impact of the physical surface modification on the EGaIn wettability and resulting film quality, Figure 3.4 (c) and (d) compare patterned EGaIn films on a normal, smooth PDMS surface and a paper-textured PDMS surface. To this end, a square-shape PDMS stamp with 1 cm × 1 cm dimensions was prepared, and EGaIn was stamped on both the normal PDMS and the paper-textured PDMS substrate. As expected, patterned EGaIn on the normal, smooth PDMS surface exhibits non-uniform films with EGaIn droplets and non-covered areas, as shown in Figure 3.4 (d)-i). Because of this non-uniform thickness resulting from poor surface wetting, stamping lithography has been typically considered the least reliable EGaIn patterning method [32, 83]. In contrast,

patterned EGaIn on the physical-surface-modified PDMS shows smooth and uniform thin films, as seen in Figure 3.4 (d)-ii). Figure 3.4 (d)-iii) shows a cross-sectional view of the stamped EGaIn thin film on the paper-textured PDMS after being covered with an additional PDMS layer, demonstrating the uniformly molded ≈ 1.45 μm thick EGaIn film patterned on the paper-textured PDMS substrate.

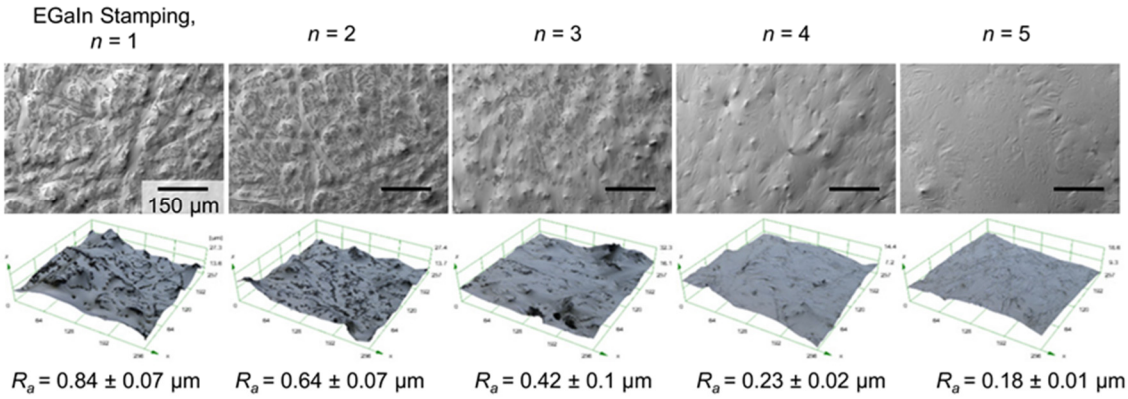

Figure 3.5 Surface characteristics of stamped EGaIn thin films on paper-textured PDMS as a function of the number of stamping steps (n). R_a indicates the average measured surface roughness using a laser confocal microscope (Olympus, LEXT OLS 4000).

The uniformity and smoothness of the EGaIn thin film were further evaluated as a function of the number of stamping steps, as shown in Figure 3.5. In the EGaIn stamping process, the PDMS surface roughness plays an important role in uniform wetting, which promotes EGaIn adhesion on a physically modified elastomeric surface. The paper-textured PDMS exhibited micrometer-sized surface structures with an average roughness R_a of 1.22 ± 0.18 μm. The additive stamping process decreases the surface roughness R_a with an increasing number of stamping steps, which indicates that the stamped EGaIn film is getting smoother. The random, micrometer-sized features on the paper-textured PDMS surface were partially wetted during the initial 1-2 stamping steps, ultimately filling the grooved areas with EGaIn. After stamping 5 times, the surface structures of the paper-

textured PDMS were fully covered with EGaIn, showing a uniform and smooth EGaIn thin film with low R_a of 0.18 ± 0.01 μm. Interestingly, after stamping > 6 times, excessive EGaIn partially formed small EGaIn edge beads along the edges of the patterned areas. To make films uniform again, these excessive edge beads can be effectively transferred to a sacrificial PDMS layer.

3.3 Large-Scale Soft Passive Electronic Devices

3.3.1 Design and Fabrication of Millimetre-Scale Soft Electronic Devices

Using the additive stamping process, soft passive components and circuits were fabricated, and their electrical and mechanical characteristics were investigated. Figure 3.6 (a) shows fabricated soft passive components, namely a resistor, a planar spiral inductor, and an interdigitated capacitor, all having 1 mm line width and 1 mm line spacing, attached to a non-planar object. One of the main requirements for soft microsystems is to maintain their electronic functionality during mechanical deformation. Thus, we experimentally investigated the electrical functionality by applying bending and stretching forces. Figure 3.6 (b) shows a simple circuit comprising a 5 × 5 array of commercial light emitting diodes (LED) on a flexible and stretchable PDMS substrate with EGaIn interconnects. Utilizing a stereo microscope for alignment, the commercial surface-mount LEDs were manually attached using a tweezer to EGaIn contacts along the patterned EGaIn lines and sealed using an additional PDMS casting step. Applying a constant current to the soft circuit, the LED array was subjected to bending (bending radius, r = 10 mm) and stretching (strain, $\varepsilon \leq 50\%$) deformations. The soft circuit withstood these bending deformations and strain up

to 50% while maintaining its electrical functionality, which also confirmed that the EGaIn thin film was uniformly patterned without voids.

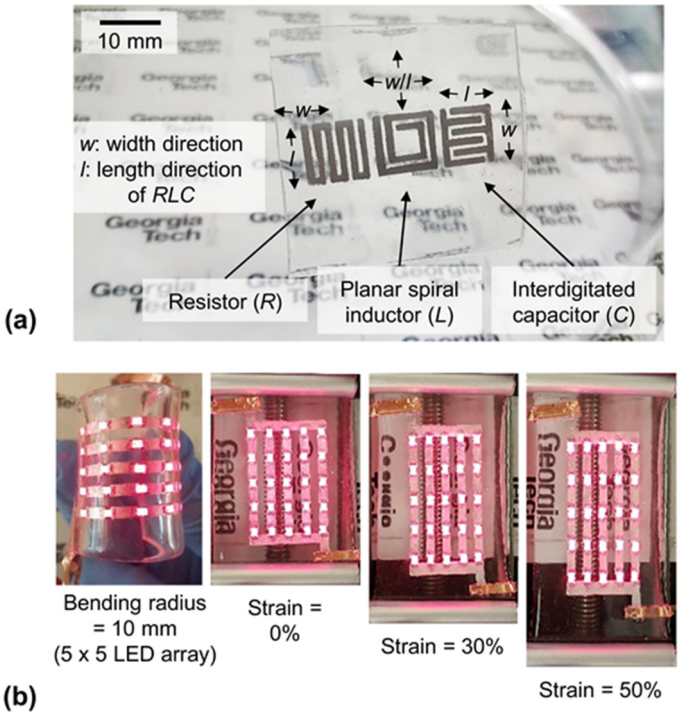

Figure 3.6 (a) Fabricated soft passive components using the additive stamping process, including a resistor, a planar spiral inductor, and an interdigitated capacitor; (b) Fabricated soft circuit with embedded LEDs (5 × 5 array) operated under bending (bending radius = 10 mm) and stretching (strain = 50%) deformation.

3.3.2 Electrical and Mechanical Characterization

The electrical and mechanical characteristics of the stamped soft passive components were investigated. Figure 3.7 (a) shows the *I*-*V* characteristic of the resistor (1 mm in width, 70 mm in length, and 1.35 μm in thickness), exhibiting an ohmic behavior with <7% deviation between the calculated and measured resistance value. Then, uniaxial strain up to 30% was applied in both width and length directions to the resistor, the planar spiral inductor, and the interdigitated capacitor. Figure 3.7 (b)-(d) shows the measured and calculated relative resistance, inductance, and capacitance changes, respectively, as a

function of the applied uniaxial strain in both length (ε_l) and width (ε_w) directions. The calculated values are based on either analytical calculations or numerical simulation using COMSOL. The relative resistance change $\Delta R/R$ of the resistor increases by stretching it along the length direction ($\varepsilon_l = \Delta l/l$) and decreases by stretching along the width direction ($\varepsilon_w = \Delta w/w$), as shown in Figure 3.7 (b). This behavior can simply be explained by the effect of geometry changes on the resistance $R = \rho l/(wt)$, considering the Poisson's ratio of the elastomeric material [46]. The Poisson's ratio is the negative of the ratio of the transverse contraction strain to the longitudinal extension strain in the direction of stretching force, with 0.5 being used for the Poisson's ratio of PDMS.

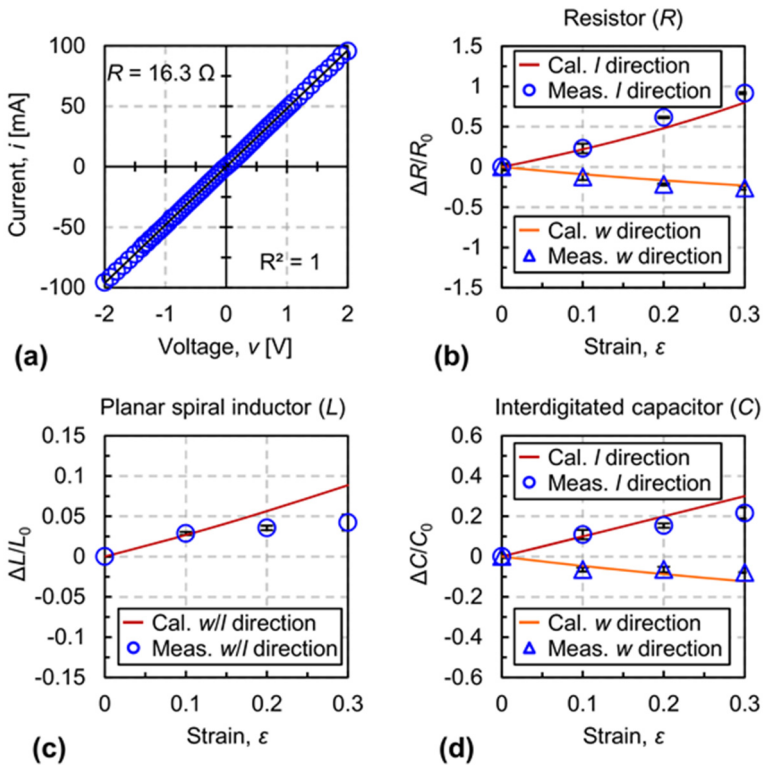

Figure 3.7 Electrical and mechanical characteristics of fabricated soft passive components: (a) *I-V* characterization of a EGaIn resistor; (b)-(d) Measured and calculated relative resistance, inductance, and capacitance changes as a function of applied uniaxial strain in both length and width directions.

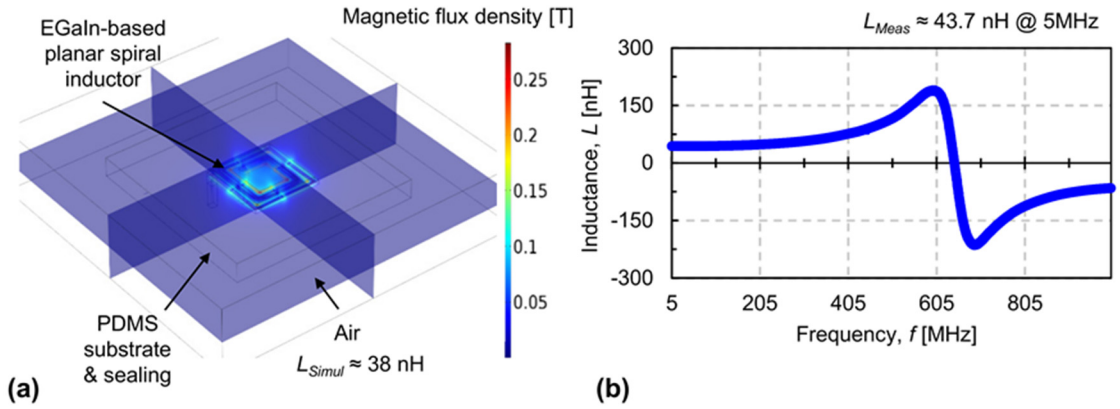

Figure 3.8 (a) Numerical evaluation of planar spiral inductor based on EGaIn using finite element simulation; (b) Measured inductance as a function of frequency.

Figure 3.8 (a)-(b) shows the electrical characteristics of EGaIn-based, planar spiral inductor, obtained using numerical and experimental approaches. Figure 3.8 (a) displays the magnetic flux density calculated using the finite element simulation with COMSOL Multiphysics (COMSOL Inc., Burlington MA). The modeled inductor is surrounded by the PDMS chip and enclosed in an air domain to encapsulate the electromagnetic field. The simulated inductance of the planar spiral inductor (d_{out} = 11 mm, d_{in} = 5 mm, and n (number of turns) = 2) was 38 nH using the magnetic and electric field physics. Figure 3.8 (b) shows the measured inductance as a function of frequency using a network analyzer (Rohde&Schwarz, ZVB 4). The measured inductance was 43.7 nH at 5MHz, which agreed well with the simulated value with <15% deviation. To evaluate its characteristics under mechanical loading, we used the modified Wheeler formula and calculated the relative inductance change $\Delta L/L$ as a function of the applied strain in both length and width directions [88-90]. Under the assumption of equibiaxial strain ($\varepsilon_{wl} = \varepsilon_w = \varepsilon_l$) and incompressible ($(\varepsilon_w+1)(\varepsilon_l+1)(\varepsilon_t+1) = 1$) conditions, the calculated $\Delta L/L$ can be simplified for strain in both width and length direction [88, 89]:

$$\frac{\Delta L}{L} = \frac{\varepsilon_{wl} + 1}{2} + \frac{1}{2\sqrt{\varepsilon_{wl} + 1}} - 1 \quad (1)$$

Overall, both calculated and measured $\Delta L/L$ increase by stretching in both width and length directions with similar behavior because of the orthotropic geometry, as shown in Figure 3.7 (c). The rather large deviation between analytically calculated and measured values, especially large strain >15%, may arise from the simplified 2D analytical model and the shape distortion of the planar spiral inductor while stretching [88, 91].

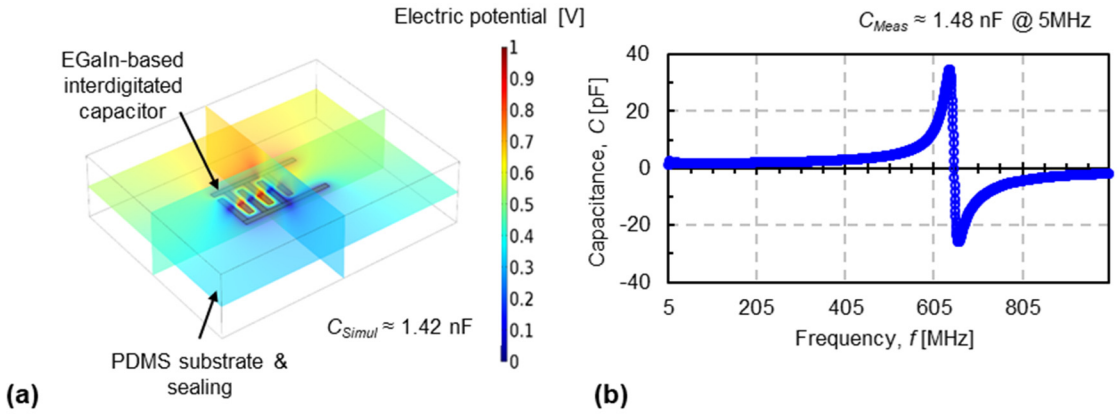

Figure 3.9 (a) Numerical evaluation of interdigitated capacitor based on EGaIn using finite element simulation; (b) Measured capacitance as a function of frequency.

The electrical characteristics of the EGaIn-based, interdigitated capacitor are displayed in Figure 3.9. Figure 3.9 (a) shows the simulated electric potential of the interdigitated capacitor for an applied voltage of 1 V, obtained using COMSOL Multiphysics (COMSOL Inc., Burlington MA). The simulated capacitance of the interdigitated capacitor (l (length of the electrode) = 6 mm and n (number of electrodes) = 6) was 1.42 nF using the electrostatic physics. Figure 3.9 (b) shows the measured capacitance as a function of frequency using a network analyzer (Rohde&Schwarz, ZVB 4). The measured capacitance was 1.48 nF at 5MHz, which again agreed well with the

simulated value with <5% deviation. By adopting a conformal mapping technique [90], which provides a closed-form expression for the capacitance by transforming the coplanar line geometry to a parallel-plate structure, the calculated capacitance C can be simplified to $C_0(\varepsilon_l+1)$ under the conditions of $l = l_0(\varepsilon_l+1)$, $w = w_0(\varepsilon_w+1)$, $s = s_0(\varepsilon_w+1)$, and $(\varepsilon_w+1)(\varepsilon_l+1)(\varepsilon_t+1) = 1$, with s being the electrode spacing. Therefore, the calculated relative capacitance change $\Delta C/C$ can be simplified to ε_l under strain the length direction and equation (2) under strain in the width direction [32, 88].

$$\frac{\Delta C}{C} = \frac{1}{\sqrt{\varepsilon_{\mathrm{w}} + 1}} - 1 \tag{2}$$

Both calculated and measured ΔC/C linearly increase when the interdigitated capacitor is stretched along the length direction, whereas they monotonically decrease when stretched along the width direction, as shown in Figure 3.7 (d). As discussed above for the planar spiral inductor case, the 2D nature of the analytical model and the shape distortion of the interdigitated capacitor likely cause the deviation between analytically calculated and measured values [88].

3.4 Examples of 3D-Integrated Soft Microsystems Based on Additive and Subtractive Stamping Techniques

By combining the additive and subtractive stamping techniques with 3D heterogeneous integration, more complex soft microsystems can be realized. Two different skin-mountable, soft functional microsystems based on 3D integration are demonstrated: a fingertip-mountable, soft biological sensing platform in subchapter 3.4.1 and soft heaters with localized and distributed heating capability in subchapter 3.4.2.

3.4.1 Fingertip-Mountable, Soft Biological Microsystems

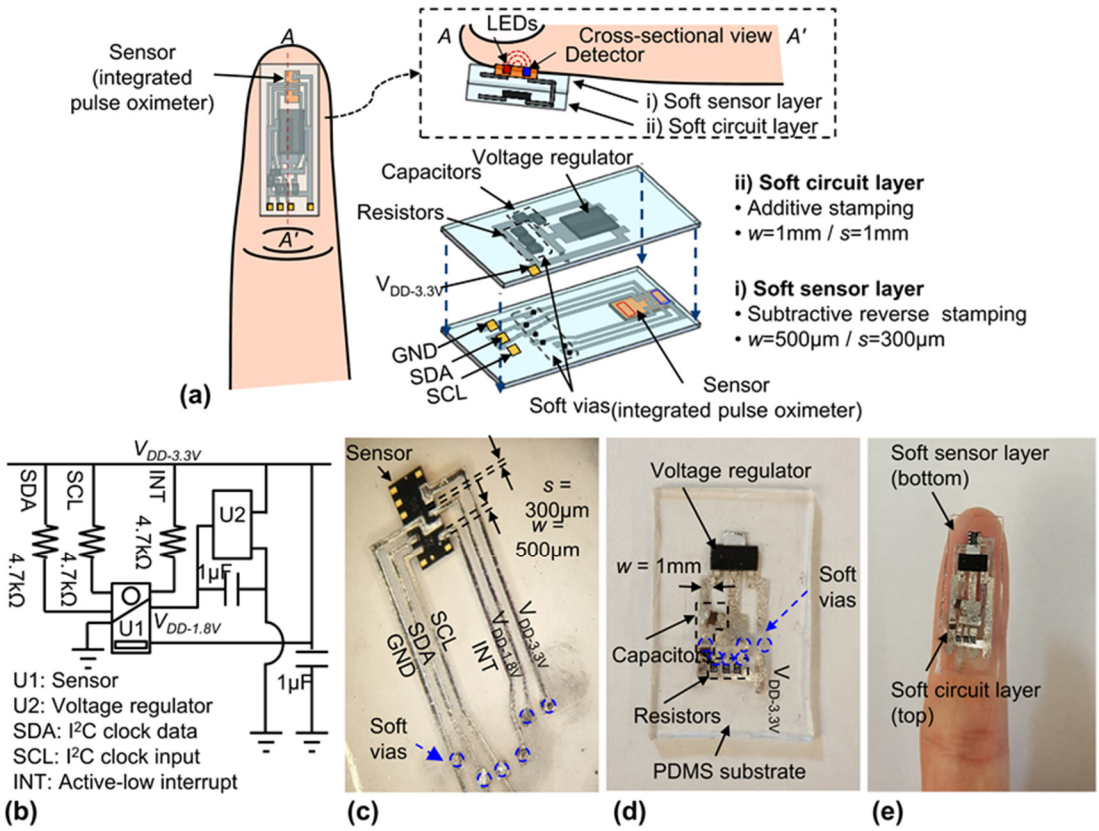

Figure 3.10 (a) Demonstration of fingertip-mountable, soft and 3D-integrated biological sensing platform using integrated pulse oximeter mounted on fingertip; (b) Circuit diagram; Fabrication and electric component integration of (c) soft sensor layer patterned using subtractive reverse stamping technique and (d) soft circuit layer patterned using additive stamping technique; (e) 3D-integrated biological microsystem mounted on fingertip.

To highlight the multiscale EGaIn patterning capabilities, a fingertip-mountable, soft and 3D-integrated biological sensing platform was demonstrated, as shown in Figure 3.10 (a). The soft biological sensing platform, fabricated in a hybrid electronics format, comprises a soft sensing layer with a commercial pulse oximeter and a soft interfacing circuit layer. These soft sensing and circuit layer were vertically interconnected through EGaIn-filled soft vias. Thanks to EGaIn's soft and stretchable properties, the soft biological sensing platform enables conformal skin contact for non-invasive and real-time heart rate and blood oxygen monitoring.

The soft sensor layer was fabricated using the subtractive reverse stamping technique for microscale EGaIn patterning to connect the integrated pulse oximeter (MAX30100, Maxim Integrated Products Inc.). The pulse oximeter is directly in contact with a fingertip, as shown in Figure 3.10 (a)-(c). All electrodes of the integrated pulse oximeter for ground, supply voltage, and I^2C (inter-integrated circuit) communication are connected to patterned EGaIn lines with 500 μm in width and 300 μm in spacing (Figure 3.10 (c)). The fabricated soft sensor layer was then vertically interconnected with the soft interfacing circuit layer through soft vias with 500 μm in diameter. The additive stamping technique was used to fabricate the sPCB for the interfacing circuit, as shown in Figures 3.10 (b) and (d). The electronic components, including a voltage regulator, resistors, and capacitors, were manually attached using a tweezer along the patterned EGaIn lines having 1 mm width and >1 mm spacing, utilizing a stereo microscope for alignment. The soft interfacing circuit layer was then sealed using an additional PDMS casting process. Figure 3.10 (e) shows the fabricated soft biological microsystems mounted on the fingertip of an index finger for heart rate and blood oxygen monitoring.

Photoplethysmogram (PPG) measurement were obtained using the EGaIn-based soft PPG sensing system and compared with a PCB-based rigid PPG sensing system (MIKROE-2000, MikroElektronika Ltd.). Figures 3.11 (a) and (b) show the measured PPG waveforms for the infrared (IR) LED and red LED and the extracted heart rate (HR) and saturation of peripheral oxygen (SpO_2) using the PDMS/EGaIn-based soft sensing system (HR = 79±3.6 bpm and SpO_2 = 97%), demonstrating identical sensing performance compared to the PCB-based rigid sensing system (HR = 79.1±3.1 bpm and SpO_2 = 97%). Moreover, thanks to its softness and light weight, this soft system provides conformal contact and adhesion, more suitable for skin-mountable biological microsystems.

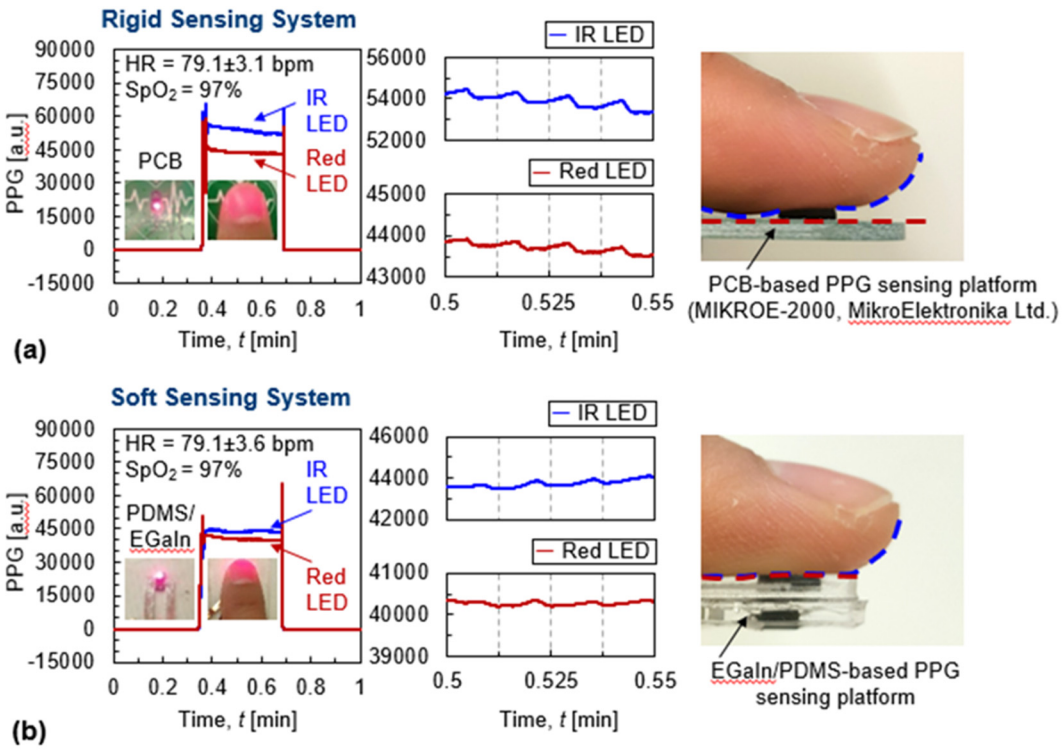

Figure 3.11 Measured photoplethysmogram (PPG) waveforms of infrared (IR) LED and red LED using (a) PCB-based rigid sensing system (heart rate (HR) = 79.1±3.1 bpm and saturation of peripheral oxygen (SpO_2) = 97%) and (b) PDMS/EGaIn-based soft sensing system (HR = 79±3.6 bpm and SpO_2 = 97%).

3.4.2 *Soft Heaters with Localized and Distributed Heating Capability*

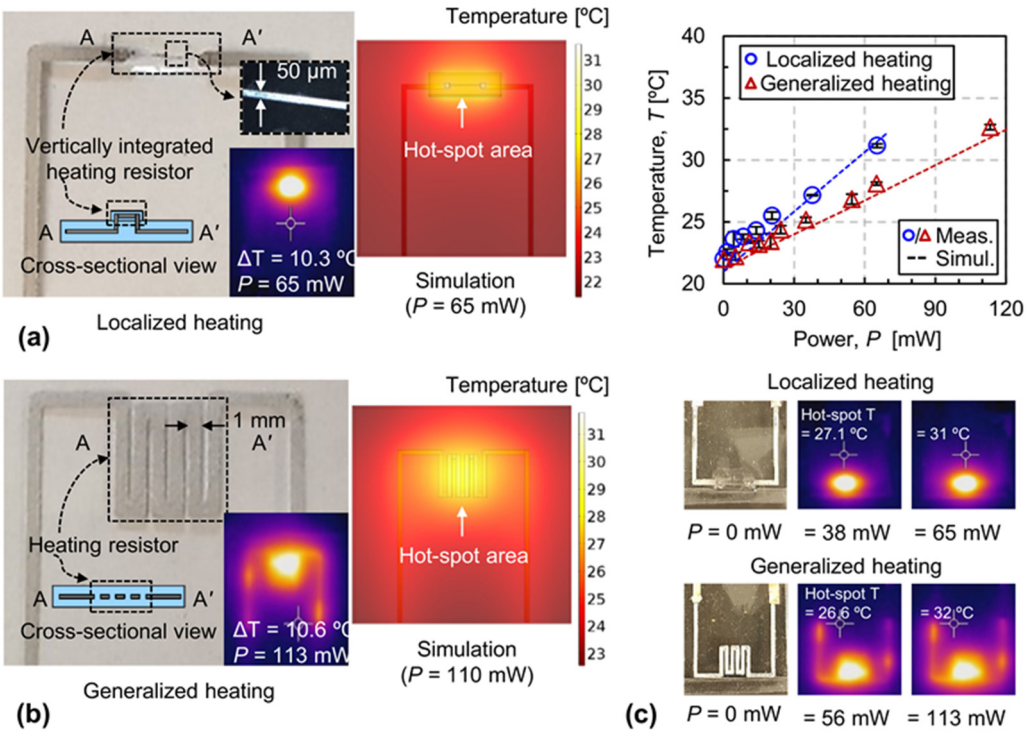

Figure 3.12 Demonstration of wearable and skin-mountable soft heaters for (a) localized and (b) distributed heating applications; (c) Simulated and measured hot-spot temperature as a function of applied heating power.

To highlight the EGaIn thin-film patterning capability, soft heaters based on EGaIn thin-film resistors were demonstrated for localized and distributed heating applications with <60 ºC operating temperature because of the thermal degradation of PDMS at higher temperatures. For the localized heating applications (Figure 3.12 (a)), a 50-µm-wide heating resistor fabricated using the subtractive reverse stamping technique was vertically integrated on a soft circuit. For large area heating applications (Figure 3.11 (b)), a 1-mm-wide serpentine heating resistor fabricated using the additive stamping technique was patterned along with a soft circuit. Figure 3.11 (c) shows the measured and simulated hot-spot temperature as a function of the applied heating power. To reach a temperature

increase of $\Delta T \approx 10$ ºC, the vertically integrated microheater requires 65 mW and heats a localized area, while the serpentine-shaped heater heats a larger area but requires 113 mW. Compared to other literature [92-94], the fabricated soft heaters using thin-film resistors showed x8 higher heating efficiency (0.158 ºC mW^{-1} for the localized heating approach and 0.093 ºC mW^{-1} for the distributed heating approach). In addition to efficient heating, the soft heater provides flexibility and stretchability for wearable and skin-mountable electronics applications.

3.5 Conclusion

This chapter introduces large-area and uniform EGaIn thin-film patterning by utilizing an additive stamping technique based on soft lithography for large-scale soft electronics applications. Considering the size scalability of the thin-film patterning and the possibility to heterogeneously integrate structures, soft electronic components can be fabricated and integrated to form high-density and multifunctional microsystems for physical, chemical, and biological sensing applications.

CHAPTER 4. NANOFABRICATION FOR SUBMICRON-SCALE SOFT ELECTRONIC DEVICES

4.1 Motivation

The moldable characteristics of EGaIn have enabled a wide range of patterning methods based on lithography-assisted fabrication [27-29, 37], fluid injection [35, 36, 95], as well as additive [33, 34] and subtractive [30, 96] patterning processes, as shown in Figure 4.1. Stamping techniques [79, 84] based on soft lithography in combination with wetting/nonwetting surface modifications and 3D integration can solve current EGaIn patterning challenges, by providing i) smooth and uniform deposition of thin films ii) multiscale patterning, and iii) high-density and functional integration, as discussed in Chapters 2 and 3. However, creating submicron-scale (*res* < 2 μm) EGaIn thin-film (*t* < 1 μm) patterns remains challenging [11, 26]. In particular, while micrometer-scale EGaIn thin-film patterning based on soft lithography was demonstrated in Chapter 2, scaling this process down to submicron features is difficult because of the high surface tension (632 mN m^{-1}) of EGaIn.

This Chapter presents a novel fabrication technique to create submicron-scale all-soft electronic devices based on EGaIn by combining electron-beam lithography (EBL) for micro/nanostructure fabrication and soft lithography for EGaIn stamping (Figure 4.1). The proposed hybrid lithography process enables high resolution and high density all-soft electronic passive components and microelectrode arrays. For the first time, submicron-scale EGaIn thin film patterning with feature sizes as small as 180 nm is demonstrated.

Thanks to the intrinsic softness of EGaIn, the fabricated soft devices can endure mechanical deformation, while maintaining electrical functionality.

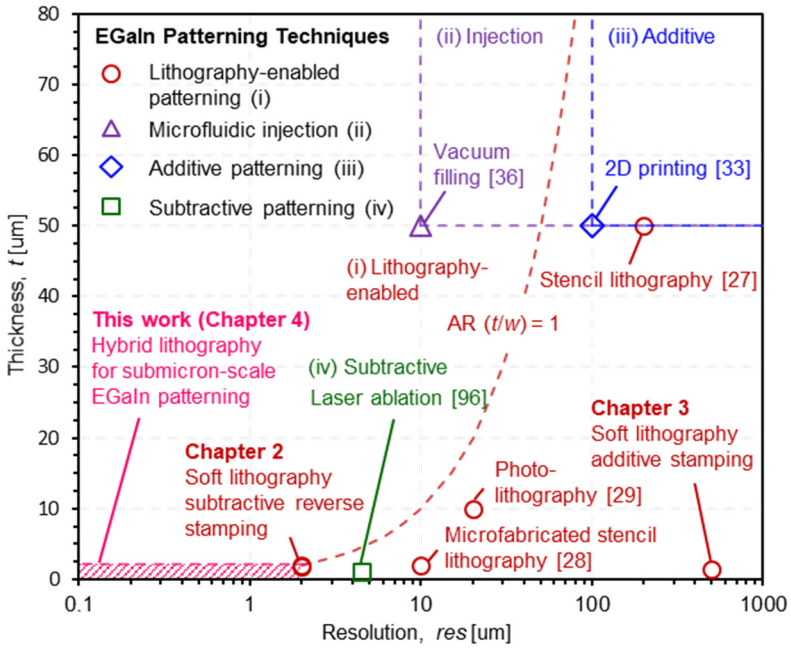

Figure 4.1 Liquid metal patterning technologies: comparison of resolution (line width) and film thickness of conventional liquid metal patterning techniques as well as proposed hybrid lithography for submicron resolution.

4.2 Hybrid Lithography for Sub-Micron Liquid Metal Thin-Film Patterning

4.2.1 Fabrication Process

Figure 4.2 shows the schematic illustration of the investigated hybrid lithography process by combining EBL and soft lithography for submicron-scale EGaIn thin-film patterning. The fabrication process is comprised of three steps: i) nano/microstructure fabrication using EBL (or any other lithography technique able to pattern submicron features), ii) EGaIn stamping, and iii) soft material encapsulation and release process from

the silicon (Si) wafer. The process starts with spin-coating a water-soluble sacrificial layer (poly(acrylic acid), PAA) on a Si wafer at 2000 rpm for 30 s and baking the film at 100 ºC for 60 s, resulting in ≈ 6 μm thickness. Over the PAA sacrificial layer, a 600 nm thick parylene-C film was deposited by chemical vapor deposition (CVD). The parylene-C film was used as a barrier layer to protect the underlying PAA layer during the following EGaIn patterning and during the release of the fabricated soft electronic devices from the Si wafer after the soft material encapsulation process. For nano/microstructure fabrication, EBL was utilized to pattern spin-coated poly(methylmethacrylate) (PMMA) film with thickness ranging from 200 nm to 1 μm. After exposure using the EBL tool (Elionix ELS G-100), the PMMA film is developed using a 1:1 mixture of methyl isobutyl keton (MIBK) and isopropanol. Alternatively, other lithography techniques able to pattern submicron features can be considered for this step. To enhance adhesion and uniformity of EGaIn on the parylene-C-coated substrate, a biphasic structure was adopted [96, 97]. A thin Ti/Au layer (5nm/30nm in thickness) was deposited using an electron-beam evaporator on the patterned nano/microstructure to provide strong adhesion and uniform wetting during the EGaIn stamping process (Figure 4.2 i)). In the next step, a flat PDMS stamp wet with EGaIn was gently pressed 2-3 times onto the Au-deposited nano/microstructures to transfer a thin EGaIn film. Thanks to the hydrophilic nature of Au, the stamped EGaIn was uniformly spread on the Au thin film and fills the concave nano/micropatterns with EGaIn up to the designed PMMA thickness. The stamped EGaIn on Au was then patterned using a PMMA lift-off process with acetone (Figure 4.2 ii)). Finally, the remaining EGaIn patterns were encapsulated with a soft elastomer (e.g. PDMS), and the fabricated soft electronic device were released by submerging the substrate into water >6 hours. After etching the palylene-

C layer using oxygen plasma reactive-ion etching (RIE), the soft electronic device was then encapsulated again with a soft elastomer for backside sealing (Figure 4.2 iii)). It should be noted that optical lithography with a positive-tone photoresist can be utilized as well for the microstructure fabrication. The detailed fabrication process is described in Appendix A3.

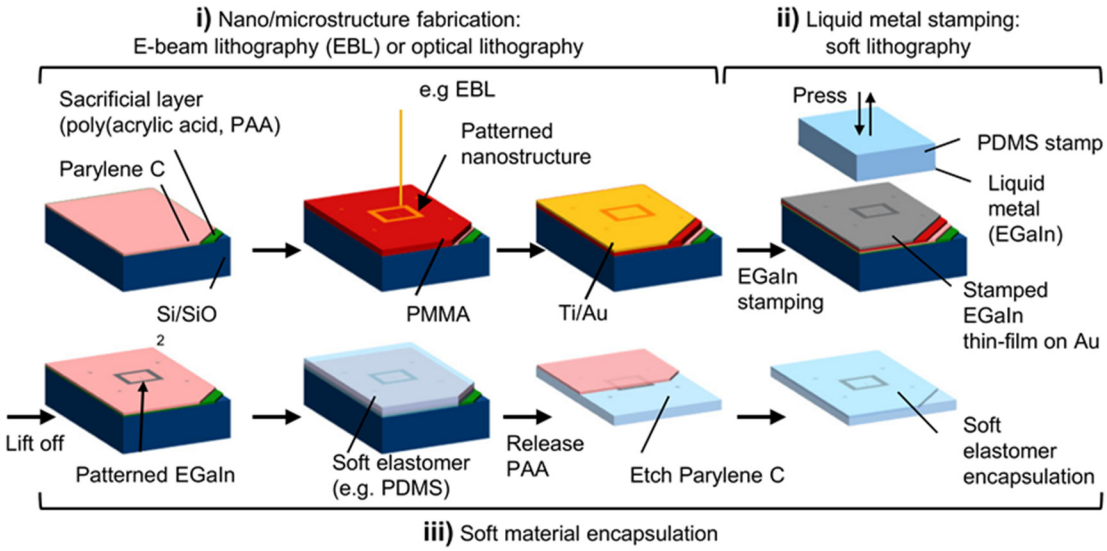

Figure 4.2 Hybrid lithography process by combining electron-beam lithography and soft lithography for submicron-scale soft electronic devices based on EGaIn.

The stamped EGaIn on Au thin film showed uniform wetting characteristics and could be successfully patterned using the PMMA lift-off process without structural deformation. Figure 4.3 (a) shows the i) patterned Au thin film after the lift-off process without EGaIn stamping and ii) the stamped and patterned EGaIn on the Au thin film, demonstrating EGaIn patterning capability using the nano/microstructures patterned using EBL in the PMMA film. Figure 4.3 (b) shows the soft material encapsulation and release process of patterned EGaIn structures. Figure 4.3 (b)-i) shows a patterned EGaIn dot array with dot dimensions ranging from 50 μm down to 500 nm. Similarly, EGaIn electrodes

were patterned on the parylene-C layer (Figure 4.3 (b)-ii)), then encapsulated with PDMS and released from the Si wafer, as illustrated in Figure 4.2-iii). Finally, Figure 4.3 (b)-iii) shows a fabricated submicron-scale, all-soft electronic device based on EGaIn and PDMS attached on the tip of a nail. The thickness of the soft elastomer is adjustable by selecting a proper target spin speed. The tested PDMS thickness was ≈ 50 μm, providing conformal wrapping capability on non-flat surfaces for skin-mountable, bioelectronics applications.

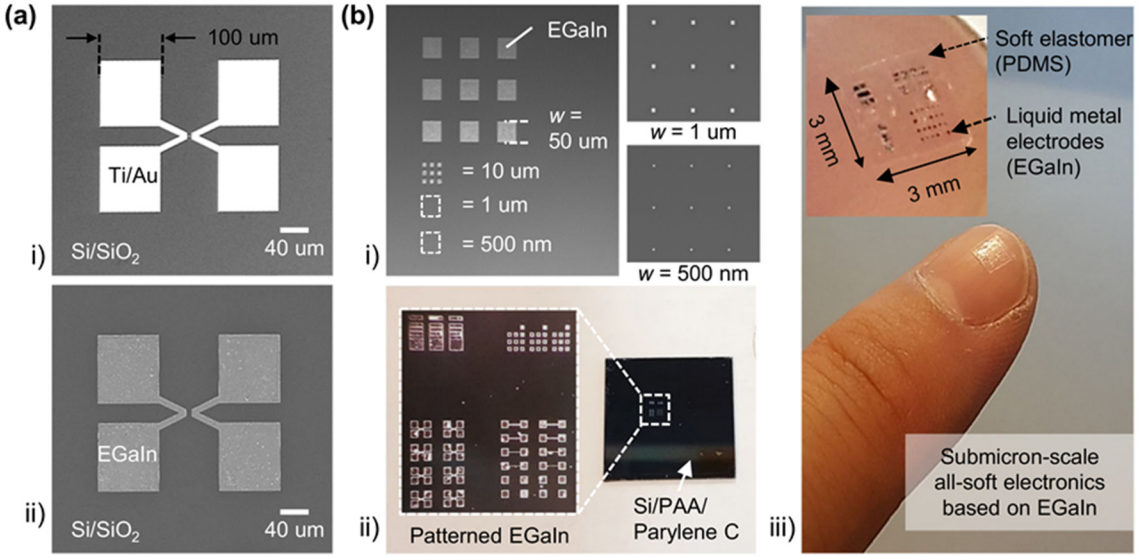

Figure 4.3 (a) Patterned i) Au and ii) EGaIn on Au thin film; (b) i) Patterned EGaIn dot array with dot dimensions ranging from 50 μm down to 500 nm, and ii)-iii) soft material encapsulation and release process of the patterned EGaIn structures.

4.2.2 *Characterization of Patterned Liquid Metal Structures*

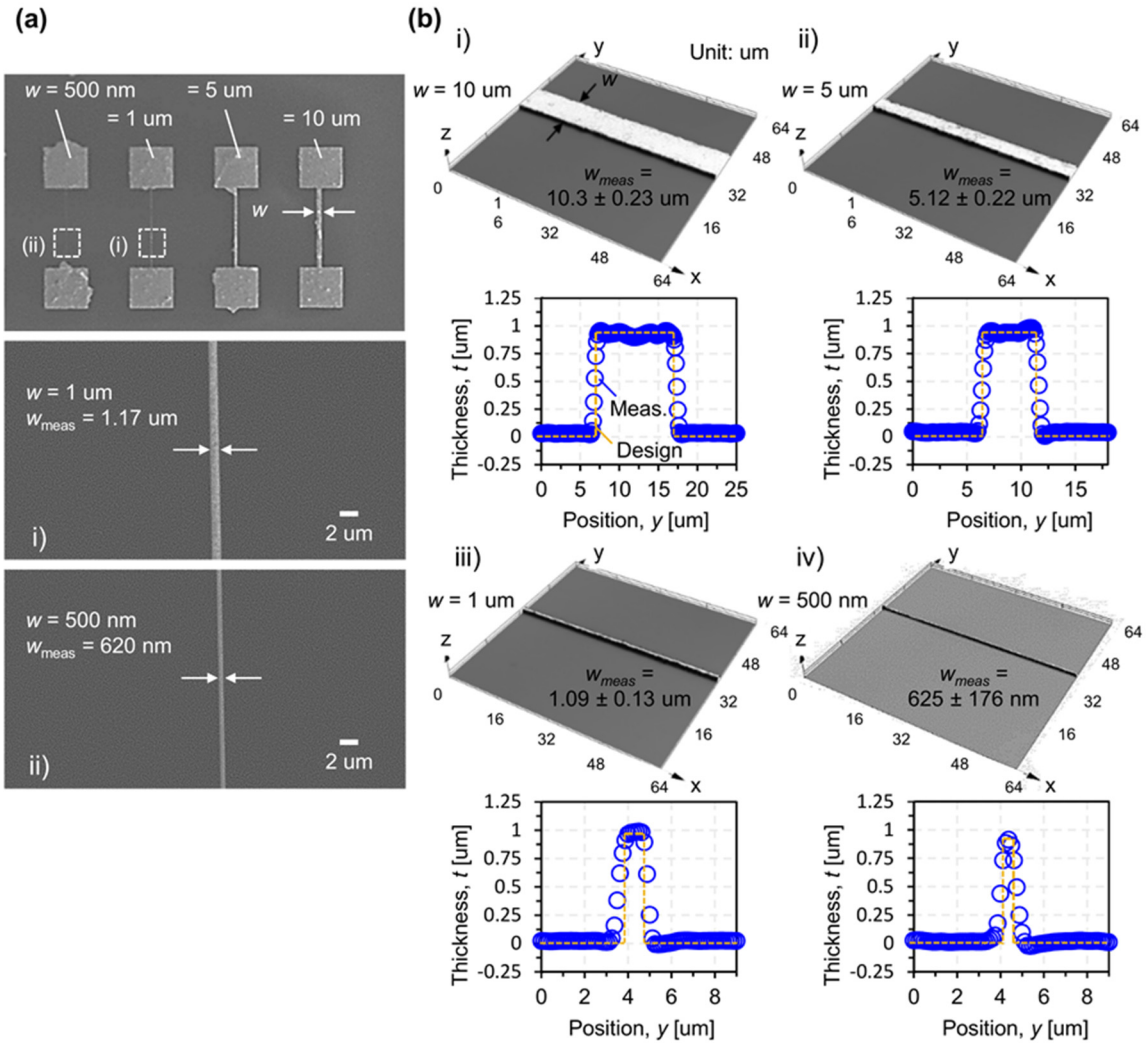

Figure 4.4 (a) SEM images of the test chip after EGaIn patterning and close-up of patterned EGaIn lines with 1 µm and 500 nm width; (b) 3D images and cross-sections of patterned EGaIn lines with width of 500 nm, 1 µm, 5 µm, and 10 µm. The 3D image and cross-sections were obtained using a laser confocal microscope (Olympus, LEXT OLS 4000).

EGaIn lines with different widths, fabricated using the hybrid lithography technique with 1 µm-thick PMMA layer, were investigated to highlight the uniform and sharp-edge patterning capability. Figure 4.4 shows (a) SEM images and (b) 3D profiles of patterned EGaIn lines with width from 500 nm to 10 µm. Thanks to the uniform and strong adhesion between Au and EGaIn, the patterned EGaIn lines shows sharp edges without

EGaIn aggregation or loss during the lift-off process (Figure 4.4 (b)). When the sacrificial PMMA layer is removed during the lift-off process, any EGaIn on the top of it is lifted-off and washed together with the PMMA layer. After the lift-off process, EGaIn remains only in the region where it had direct contact with the Au thin film. As a result, the thickness of the patterned EGaIn will be less than the thickness of the PMMA layer. Figure 4.5 shows the measured EGaIn thickness after the lift-off process as a function of the line width and compares it to the designed PMMA thickness. As expected, the measured EGaIn thickness of ≈ 918 nm is slightly smaller than the PMMA thickness, which was 1 μm in this study. Because of the use of a soft and deformable PDMS stamp for EGaIn transfer, the stamped EGaIn can be uniformly spread on the Au thin film and does not cover all PMMA edges, which makes the lift-off process possible. This result indicates that the EGain thickness can be controlled by controlling the thickness of the PMMA film. Also, the stamped EGaIn film uniformly filled the concave nano/microstructures. Figure 4.6 (a) shows the measured cross-sectional area of patterned EGaIn structures, compared with the designed cross-sectional area, as a function of the measured line width. The measured cross-sectional area of patterned EGaIn matched well with the designed value, which also confirmed that EGaIn was uniformly patterned without EGaIn aggregation or loss during the lift-off process. Therefore, the measured resistance of patterned lines matched well with the calculation. Figure 4.6 (b) shows the measured resistance of the EGaIn lines as a function of the patterned EGaIn line width for lines with 200 μm length. The measured resistance scaled linearly with the 1/width with <12% deviation compared to calculated values based on the bulky resistivity of EGaIn, indicating that the electrical properties of EGaIn dominate the

electrical characteristics of the patterned EGaIn structures even in the presence of the Ti/Au adhesion layer [96].

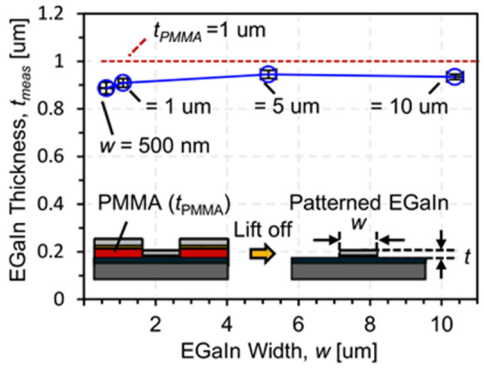

Figure 4.5 Measured thickness of PMMA film and of patterned EGaIn as a function of line width.

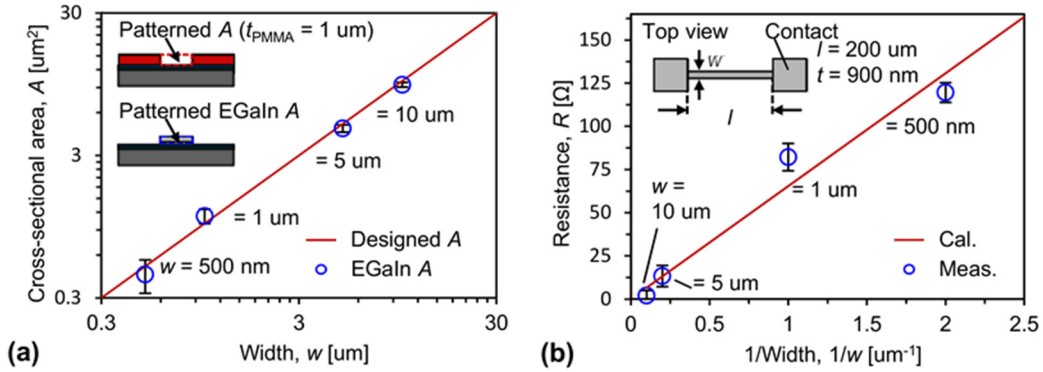

Figure 4.6 (a) Measured cross-sectional area of patterned EGaIn structures with width from 500 nm to 10 µm, compared with the designed cross-sectional area, as a function of the line width; (b) Calculated and measured resistance of patterned EGaIn lines as a function of line width.

4.2.3 Resolution and Spacing of Hybrid Lithography

Figure 4.7 and Figure 4.8 show fabricated EGaIn test patterns to evaluate the lateral resolution and line spacing of the hybrid lithography technique. With 1µm PMMA thickness, designed line widths down to 500 nm with 1µm spacing exhibit ≈ 900 nm EGaIn thickness (see Figure 4.5). However, in the case of 100 nm designed line width, the

patterned EGaIn line collapsed downward after the lift-off process, resulting in 375 nm line width with 350 nm thickness (see measured cross-section in Figure 4.7 (b)). Because the measured cross-sectional area of the patterned EGaIn line matched well with the designed value, it is concluded that the high aspect ratio (AR) >10 of the initial design is responsible for this structural instability, while the amount of EGaIn transferred is as designed. From this observation, the aspect ratio is considered one of the most important factors determining the structural instability of the patterned EGaIn lines.

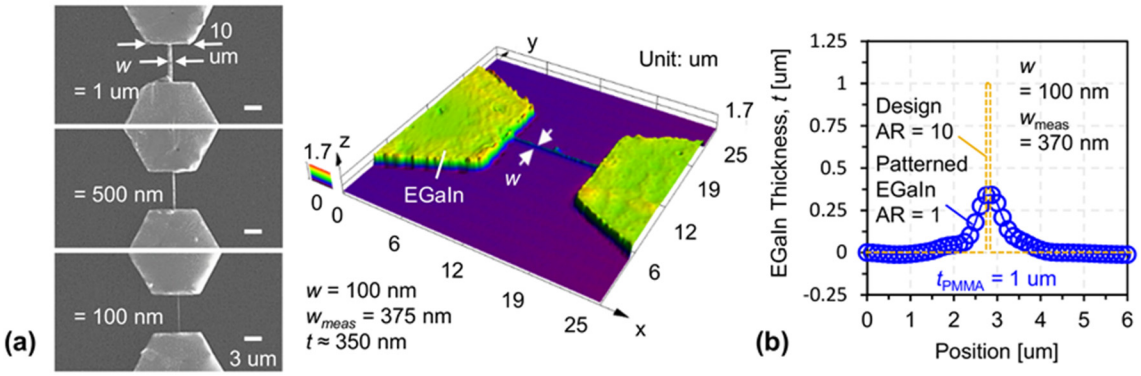

Figure 4.7 (a) SEM images of patterned EGaIn structures with line width of 100 nm, 500 nm, and 1 µm on Si wafer as well as 3D profile of patterned 100 nm line obtained using using a laser confocal microscope (Olympus, LEXT OLS 4000); (b) 3D cross-section profile of EGaIn line with designed 100 nm line width.

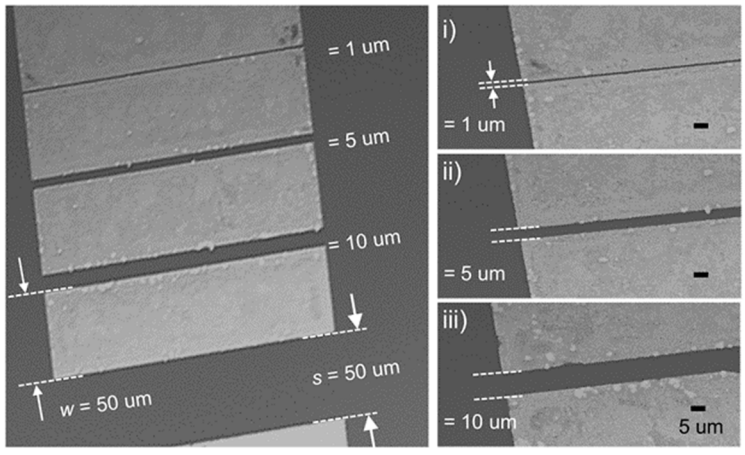

Figure 4.8 Patterned EGaIn test structures on Si wafer to evaluate line spacing limits.

Various PMMA film thicknesses from 1 μm to 300 nm were tested to investigate the structural deformation of patterned EGaIn lines and to minimize the AR effect, especially for 100 nm EGaIn thin-film patterning. Figure 4.9 (a)-i) shows the measured EGaIn thickness as a function of designed EGaIn line width for different thicknesses of the PMMA resist. As expected, EGaIn lines with width >500 nm are patterned as designed without structural deformation because the AR of the lines was <2 for the tested PMMA thicknesses ranging from 1 μm to 300 nm (Figure 4.9. (a)-ii)). In the case of lines with 100 nm width, patterned EGaIn structures for the PMMA thicknesses >600 nm collapsed downward because of the high AR > 6. On the other hand, this mechanical deformation can be minimized by adopting 300 nm PMMA thickness (Figure 4.9 (a)-iii)). In this case, 180 nm EGaIn thin-film patterning can be achieved with 250 nm line thickness, as shown in Figure 4.9 (b).

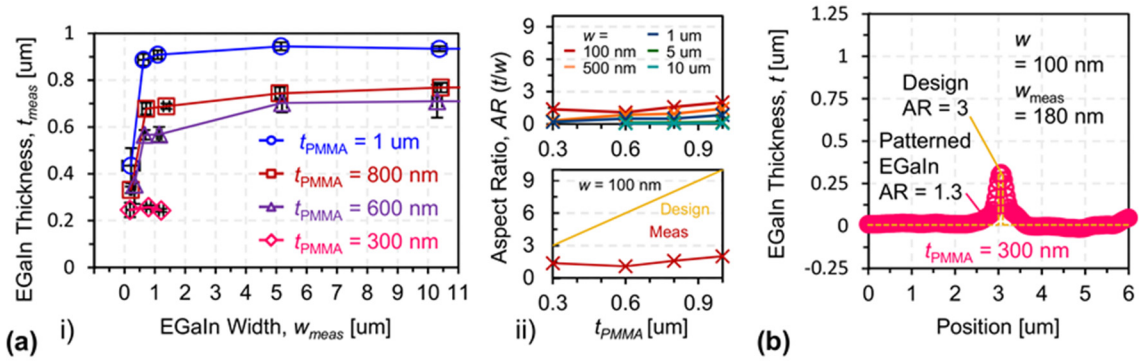

Figure 4.9 (a) i) Measured thickness of patterned EGaIn lines as a function of designed EGaIn width for PMMA resists with different thickness and ii) resulting aspect ratio (AR) of the lines as a function of the PMMA thickness; (b) 3D profile measurement of designed 100 nm wide EGaIn lines in the case of 300 nm PMMA thickness.

4.3 Examples of High-Resolution and High-Density Soft Electronic Devices

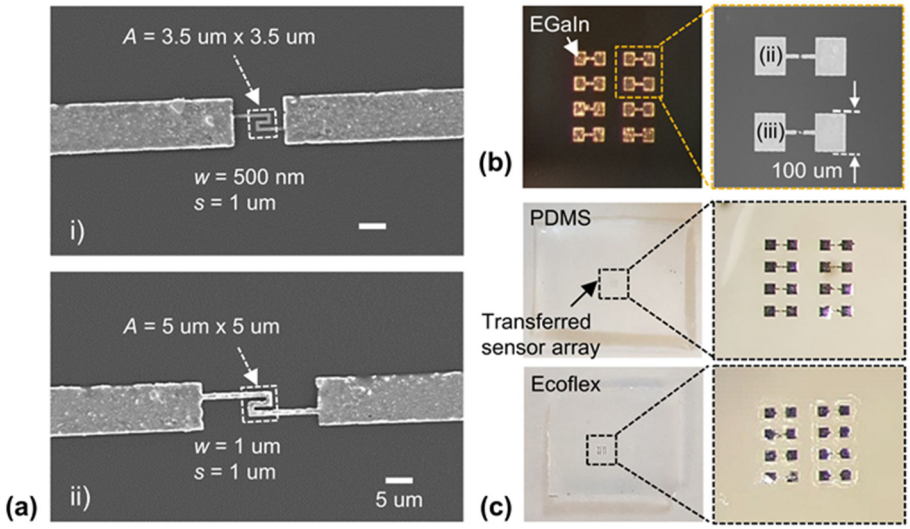

Figure 4.10 (a) High-resolution EGaIn-based soft resistors with i) 500 nm and ii) 1 μm line width; (b) All-soft resistive sensor array on a Si wafer; (c) Encapsulation with soft elastomeric materials, such as PDMS and Ecoflex, and release of soft resistive sensor array from the Si wafer.

To highlight the high-resolution patterning capability, all-soft passive electronic devices, such as soft resistive sensor arrays (Figure 4.10) and soft interdigitated capacitors (Figure 4.11), were demonstrated. Figure 4.10 (a) shows the high-resolution EGaIn-based soft resistors with i) 500 nm and ii) 1 μm line width. A soft resistive sensor array was patterned on a parylene-C layer (Figure 4.10 (b)), then encapsulated with soft elastomers and released from the Si wafer. Soft material encapsulation with both PDMS ($E \approx$ 600-800 kPa) and Ecoflex ($E \approx$ 60-70 kPa) was demonstrated to provide all-soft, resistive sensing platform, as shown in Figure 4.10 (c). Considering the size of a single biological cell, the demonstrated submicron-scale EGaIn patterning capability and its compatibility with soft, biocompatible materials may enable novel, all-soft biological sensing platforms to investigate cell mechanobiology and provide critical information for disease, management

and therapy. Similarly, Figure 4.11 (a) shows a high-resolution, soft interdigitated capacitor. Soft interdigitated capacitors fabricated using the reverse stamping technique were demonstrated with 100 µm line width, 500 µm line spacing, and up to 30 interdigitated electrodes (IDEs) in Chapter 2 and Chapter 6. Here, improved soft interdigitated capacitors with 5 µm line width and line spacing and up to 90 IDEs were demonstrated by utilizing the hybrid lithography technique. Figure 4.11 (b) shows the measured capacitance as a function of frequency up to 1MHz for capacitors with different number of IDEs. The measured capacitance with 10 IDEs was 0.2 pF and linearly increased to 1.1 pF for the capacitor with 90 IDEs. Also, finite element simulations for interdigitated capacitors were conducted using COMSOL Multiphysics (COMSOL Inc., Burlington MA) and an electrostatic physics, as discussed in Subchapter 3.3.2. Thereby, the measured capacitance as a function of the number of IDEs agrees well with the simulated values with < 15% deviation.

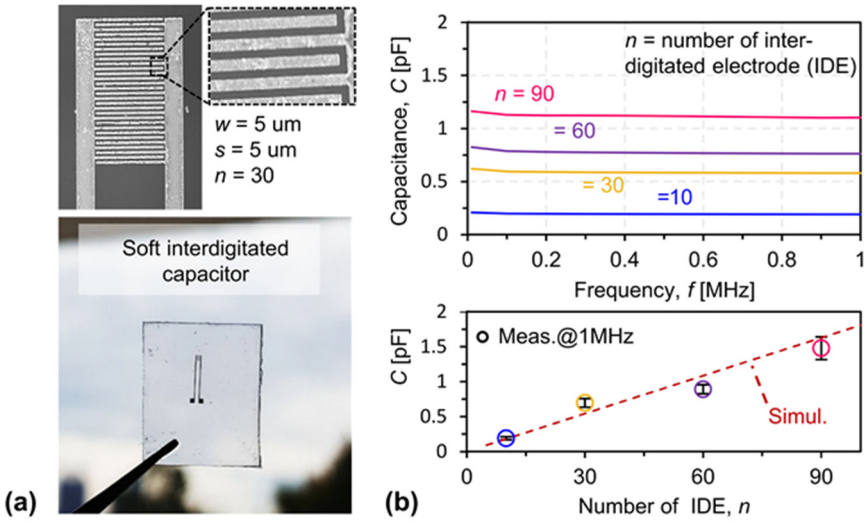

Figure 4.11 (a) Fabricated all-soft interdigitated capacitors with, 5 µm line width and spacing; (b) Measured capacitance as a function of frequency (top) and measured and simulated capacitance (at 1MHz) as a function the number of interdigitated electrodes (bottom).

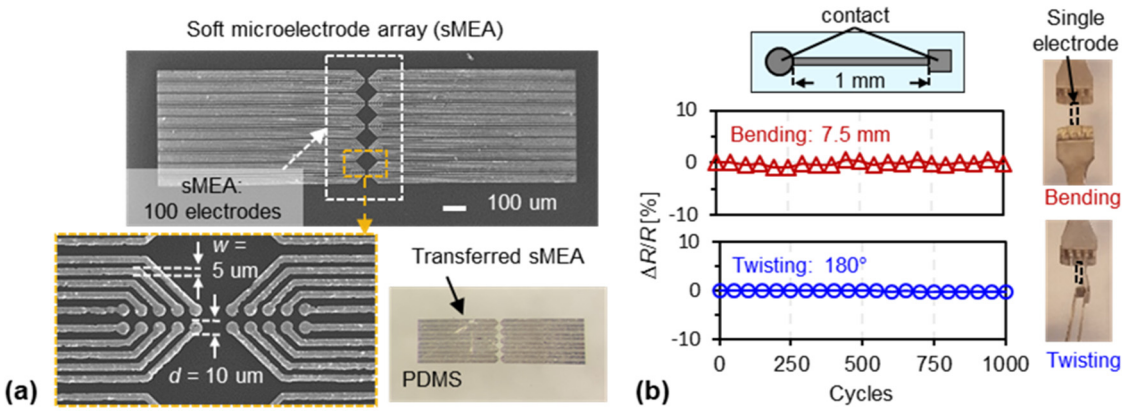

Figure 4.12 (a) All-soft microelectrode array with 100 electrodes; (b) Measured relative resistance change as a function of the number of bending and twisting cycles (bending was performed around a cylinder with 7.5 mm radius, and twisting was performed to a 180˚ angle).

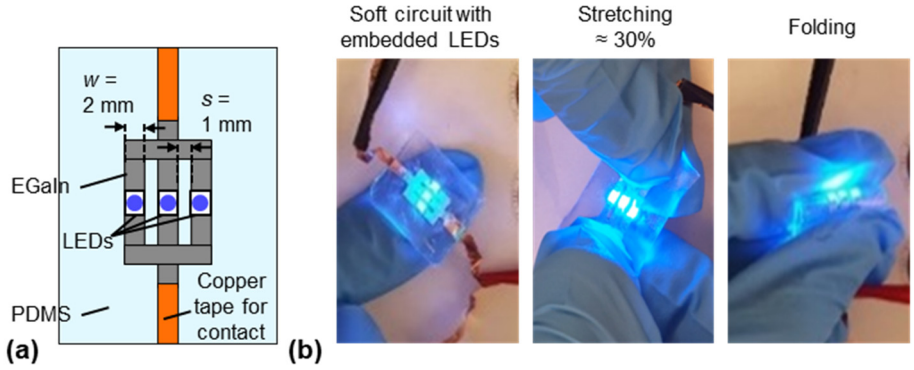

Figure 4.13 (a) Schematic illustration and (b) fabricated soft circuit with embedded LEDs under mechanical stretching and folding deformation.

In addition, an all-soft microelectrode array (sMEA) with 100 sensing electrodes, each 10 μm with 5 μm wide interconnections, was demonstrated to highlight the high-density fabrication capability, as shown in Figure 4.12 (a). The fabricated sMEA was then transferred to a PDMS substrate. As a reliability test, bending and twisting forces were applied and single microelectrode was measured. Figure 4.12 (b) shows the relative resistance changes as a function of the number of bending and twisting cycles. The measured relative resistance changes are less than ±1% for up to 1,000 bending and

twisting cycles. Finally, to demonstrate flexibility and stretchability of the fabricated soft electronic devices, commercial LEDs were integrated with a soft circuit and subjected to stretching and folding deformation (Figure 4.13). Thanks to the intrinsic softness of EGaIn, the fabricated devices can endure mechanical strain > 30% as well as folding deformation, while maintaining electrical functionality.

4.4 Conclusion

This chapter presents a novel fabrication technique to create submicron-scale EGaIn patterns for all-soft electronic devices. The hybrid lithography process combines E-beam lithography with soft lithography and enables high resolution and high density all-soft electronic passive components and microelectrode arrays. For the first time, submicron-scale EGaIn thin-film patterning with feature sizes as small as 180 nm was demonstrated. The fabricated soft electronic devices, such as microelectrode arrays and resistor arrays, can endure mechanical deformation, while maintaining electrical functionality. Considering the high-resolution and high-density EGaIn patterning capabilities, the proposed fabrication technique shows potential for soft and integrated biological sensing applications.

CHAPTER 5. ALL-SOFT PHYSICAL MICROSYSTEMS

5.1 Motivation

The human skin is the largest sensory organ of the human body and highly versatile in its sensing capabilities [1, 98, 99]. In this regard, the sense of touch plays an essential role in interacting with the real world. Sensory signals generated from human skin receptors are transported through nerve fibers and then interpreted by the brain to provide complex information about size, shape, and texture of objects, as well as motions and gestures of the human body. Moreover, the brain can interpret more sophisticated information to distinguish for example, touch and pain, and eventually convey feelings and emotions. Therefore, electronic skins, which can mimic the capability of the sensory receptors of the human skin, can potentially enable broad applications in health-monitoring, human motion detection, and human-machine interfaces [100]. This motivation initiated the development of soft physical sensing system.

One major technical challenge in current electronic skins is their high-density integration and multifunctional sensing capability to mimic human skins [100]. Also, from a systems point of view, although discrete stretchable strain sensing elements have been investigated, they typically require rigid electronic components and/or printed circuit boards (PCBs) for both sensors and readout systems, which limits their ultimate usability and leads to hard-soft material interfacial failure [100, 101].

In this chapter, the aim of the research is to demonstrate integration and multifunctional sensing capabilities of all-soft microsystems based on the reverse stamping process and the 3D integration approach. The proposed soft microsystems are composed

of a soft sensor, a soft interconnect, and a soft readout circuit, all of which are fabricated using the the reverse stamping process and integrated using the the 3D integration technique without the use of rigid components and circuit boards. Two types of 3D-integrated and all-soft physical microsystems are introduced: a finger-mountable strain sensing microsystem with intrinsic temperature compensation in subchapter 5.2 and a fingertip microsystem for simultaneous proximity, touch, and pressure measurements in subchapter 5.3 [102, 103].

5.2 Finger-Mountable Strain Sensing Microsystems

5.2.1 Design and Fabrication of Soft Strain Sensing Microsystems

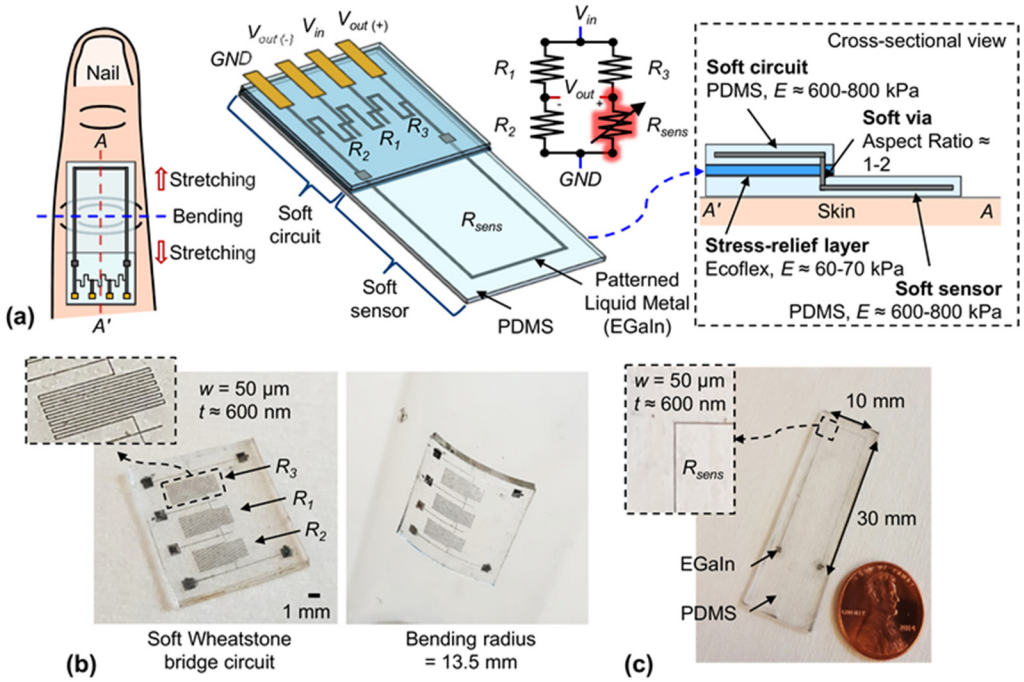

Figure 5.1 (a) Schematic illustration of 3D-integrated and all-soft physical microsystem based on EGaIn and PDMS, composed of soft readout Wheatstone bridge circuit, stress-relief layer with soft vias, and stretchable strain sensor; (b) Fabricated soft Wheatstone bridge circuit with three embedded resistors (R_1 - R_3) in flat and bending conditions; (c) fabricated stretchable strain sensor (R_{sens}).

Figure 5.1 (a) shows the schematic of the 3D-integrated, all-soft strain sensing microsystem, comprising a soft readout Wheatstone bridge (WB) circuit, a stress-relief layer with EGaIn-filled soft vias, and a stretchable strain sensor. The soft WB circuit has three resistors in series (R_1 to R_3) embedded in a PDMS substrate (with Young's modulus $E \approx$ 600-800 kPa) and is integrated on top of the soft microsensor, comprising a single strain-sensitive resistor (R_{sens}) embedded in a PDMS substrate ($E \approx$ 600-800 kPa), which is directly mounted on the skin. The WB circuit and soft microsensor are vertically interconnected using EGaIn-filled soft vias in a softer stress-relieving material (Ecoflex 00-30, $E \approx$ 60-70 kPa) to block stress acting on R_{sens} from the resistors in the soft WB circuit. As a result, the output voltage acquired from the soft circuit is primarily affected by bending and stretching motions of the stretchable strain sensor mounted on a finger. All components were fabricated using the reverse stamping technique based on soft lithography, described in Chapter 2. Figures 5.1 (b) and (c) shows the fabricated soft WB circuit and stretchable strain sensor, respectively. The resistors (R_1 - R_3 and R_{sens}) have the same width (w = 50 μm), length (l = 70 mm), and thickness ($t \approx$ 646±59 nm), yielding the same resistance values ($R \approx$ 0.6±0.07 kΩ) to make a balanced circuit. The detailed device designs and dimensions of the soft WB circuit and the soft strain sensor are shown in Appendix B1.

5.2.2 Electrical and Mechanical Characterization

The strain sensor was stretched up to 30% along the resistor's length direction, and the measured relative resistance change ($\Delta R/R_0$) increases as a function of the applied uniaxial strain, as shown in Figure 5.2. The measured resistance change with applied strain can be explained by the effect of geometry changes on the resistance, with an analytical model given in Equation (3) [46, 104].

$$\frac{\Delta R}{R} = \left(\frac{(1+\varepsilon)^2 x_0/(1-\upsilon\varepsilon)^2 + (1-\upsilon\varepsilon) y_0/(1+\varepsilon)}{(1+\varepsilon)x_0 + (1-\upsilon\varepsilon)y_0} \right) - 1 \quad (3)$$

where ε is the applied strain, υ is the Poisson's ratio of the elastomeric material, $x_0 = L_x/(L_x+L_y)$ and $y_0 = L_y/(L_x+L_y)$ are the ratios of parallel and perpendicular segmental length of the strain sensor, respectively, with L_x and L_y being the lateral and perpendicular length of the strain sensor, respectively.

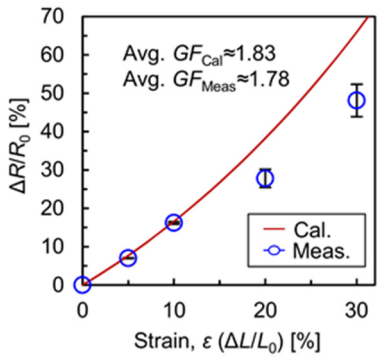

Figure 5.2 Measured relative resistance change as a function of the longitudinal strain, compared with the analytical model shown in Equation (3).

The measured resistance change matches the calculated values (based on Equation (3) well for applied strain <10%. However, the measured $\Delta R/R$ is significantly smaller than the calculated values for large strain >20%, which is believed to be caused by the non-uniform stress distribution in the sensing resistor (e.g., due to necking). Over the investigated strain range, the measured gauge factor $GF_{Meas} = (\Delta R/R)/\varepsilon \approx 1.78$ agrees well with the analytically calculated average $GF_{Cal} \approx 1.83$.

The electrical characteristics of the soft WB circuit were investigated with and without bending deformation of the soft WB circuit, and the measured output voltage was compared with calculated values given in Equation (4) [49].

$$V_{\text{out}} = V_{\text{in}}\left(\frac{R_{\text{sens}}}{R_3 + R_{\text{sens}}} - \frac{R_2}{R_1 + R_2}\right) \quad (4)$$

where V_{out} and V_{in} are the output and input (1 V) voltages, respectively, R_1 - R_3 are the resistors embedded in the soft WB circuit, and R_{sens} is the external variable sensing resistance.

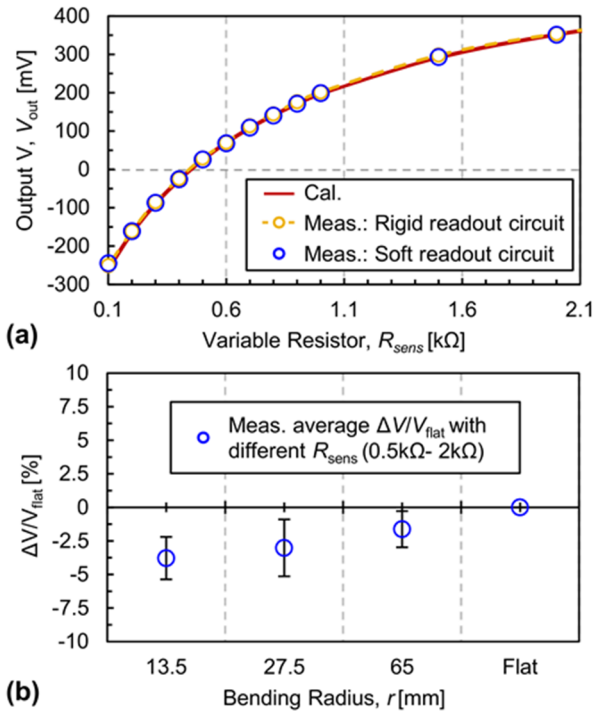

Figure 5.3 (a) Calculated and measured output voltage using the soft Wheatstone bridge readout circuit and a reference rigid readout circuit as a function of the sensor resistance; (b) Measured relative output voltage change ($\Delta V/V_{\text{flat}}$) as a function of the bending radius (65 mm, 27.5 mm, and 13.5 mm), averaged for different sensor resistances.

Figure 5.3 (a) shows the calculated and measured output voltage using the soft WB circuit board and a rigid reference circuit board as a function of a variable sensing resistance without bending deformation. The measured output voltage from the soft WB circuit matches well with the calculated values and shows the identical electrical behavior compared to the rigid circuit board. Thus, the soft WB circuit can replace the rigid WB

circuit. The impact of bending deformation on the soft WB circuit was investigated by attaching it to the surfaces of circular cylinders with radii of 65 mm, 27.5 mm, and 13.5 mm (Figure 5.1 (b) and Figure 5.3 (b)). The measured output voltage for a fixed sensing resistance decreases with decreasing cylinder radius, because of the increase of the resistances R_1 through R_3 upon bending [79]. Overall, the relative output voltage change ($\Delta V/V_{\text{flat}}$) was <6% compared to the flat condition for all bending radii, because of the small increase of the resistances R_1 through R_3 upon bending. Moreover, the output voltage of the soft circuit is more easily changed in response to stretching deformation because of the resulting geometry changes, as observed in the strain sensing characteristics (Figure 5.2). This sensitivity of the soft circuit to bending and stretching deformations requires minimizing the stress and strain acting on the soft WB circuit in a sensing application, while the stress/strain acting on the sensing resistor should be maximized. This motivates the use of a soft stress-relief layer to mechanically decouple the soft WB circuit from the sensing resistor.

5.2.3 3D Integration to Reduce Mechanical Coupling and Temperature Sensitivity

The complete strain sensing microsystem was assembled and tested both mechanically and thermally. The 3D integration approach for the soft strain sensing microsystems enables to compensate mechanical and thermal noise. To prevent strain applied to the stretchable strain sensor from reaching the soft WB circuit, we employed a softer stress-relief layer (Ecoflex 00-30), which has EGaIn-filled soft vias for vertical electrical interconnects between the PDMS-based soft sensor and WB circuit [79]. Figures 5.4 (a) and (b) show details of the fabricated 3D physical microsystem and it being mounted on the proximal-interphalangeal joint of an index finger (see Figure 5.4 (c)). The three

layers of the microsystem were bonded to each other after oxygen-plasma treatment and vertically stacked using alignment marks located at each edge of the soft circuit.

The radius of the soft via was 500 μm, while the thickness of the stress-relief layer was 1-2 mm. Numerical simulations (COMSOL Multiphysics) highlight the effectiveness of the stress-relief layer in significantly reducing the stress acting on the soft circuit as shown in Figure 5.5 (a). Figure 5.5 (a)-i) shows the finite element simulation model and boundary conditions used to evaluate the stress-blocking performance of the stress relief film under bending and stretching deformation using a solid mechanics physics model. The outer surface of the sensor layer at the circuit side was fixed, and boundary load was applied to the opposite surface of the soft sensor layer in both the x-direction and negative z-direction to apply stretching and bending deformation. To experimentally verify the effectiveness of the stress-relief layer, Figure 5.5 (b) shows the measured average relative resistance change ($\Delta R/R_0$) of the WB circuit resistors (R_1 - R_3) as a function of uniaxial strain applied to the strain sensor with and without the stress-relief of either 1 mm and 2 mm thickness. Without the stress-relief layer, strain acting on the strain sensor was directly transferred to the soft circuit (see also simulation Figure 5.5 (a)-ii), resulting in an average resistance increase of 17.4% at 30% strain. On the other hand, by adopting the stress-relief layer, any strain acting on the strain sensor has a much-reduced impact on the stress/strain distribution in the WB circuit, as shown in the simulation (Figure 5.5 (a)-iii and -iv). The measured average resistance change of the resistors of the WB circuit under the 30% strain was <5% with a 1-mm-thick stress-relief layer and <1% with a 2-mm-thick stress-relief layer, demonstrating the stress-blocking performance of the vertically integrated, soft physical microsystem.

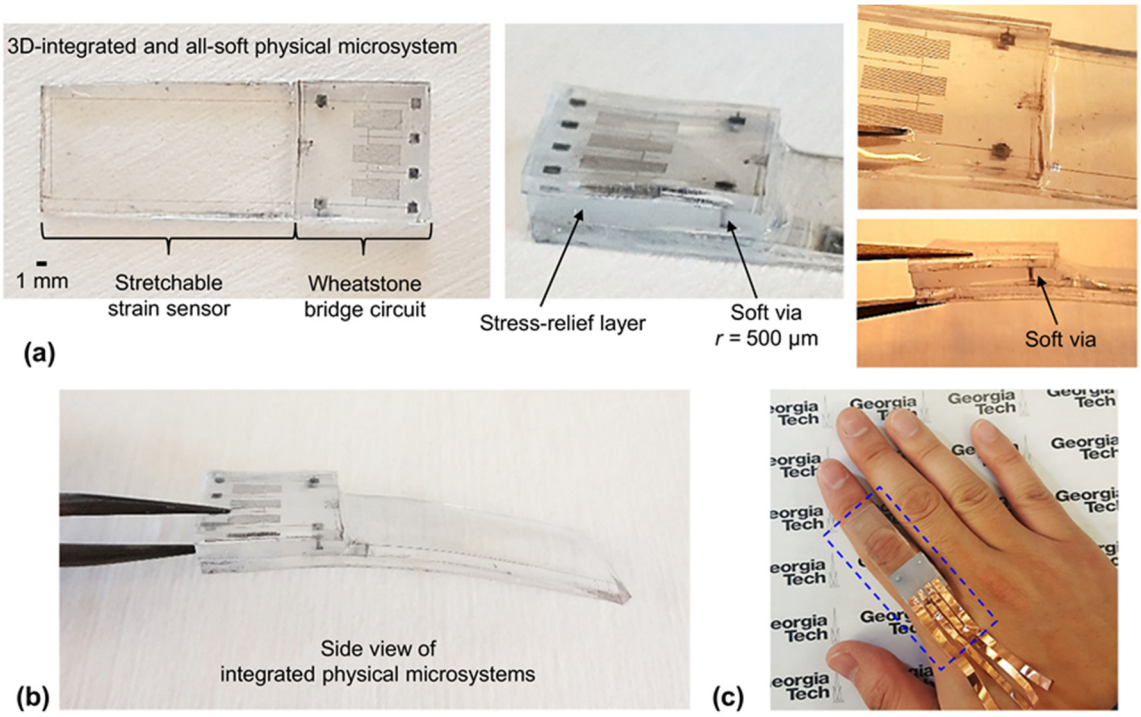

Figure 5.4 (a) Fabricated 3D-integrated and all-soft physical microsystem for skin-mountable strain sensing; (b) Side view of the integrated physical microsystem; (c) Strain microsystem mounted on the proximal-interphalangeal joint of an index finger.

Also, by integrating the strain sensor with the readout circuit to form a full Wheatstone bridge, surrounding temperature effects can be minimized. Figure 5.5 (c) shows the measured relative output voltage change ($\Delta V_{out}/V_{in}$) of the strain sensing microsystem and the measured resistance change ($\Delta R/R_0$) of the single strain sensor as a function of the surrounding temperature. As expected, the output resistance of the strain sensor is susceptible to surrounding temperature changes. The measured $\Delta R/R_0$ of the single strain sensor linearly increased with increasing surrounding temperature and was measured to be ≈ 3.4% for a temperature increase of 40˚C. On the other hand, by integrating the soft strain sensing microsystems, the measured $\Delta V_{out}/V_{in}$ was <0.2% for the same temperature increase of 40˚C, which demonstrated the ability to compensate for

temperature changes, one of the key advantages of the system-level integration of a full Wheatstone bridge compared the use of single strain sensors.

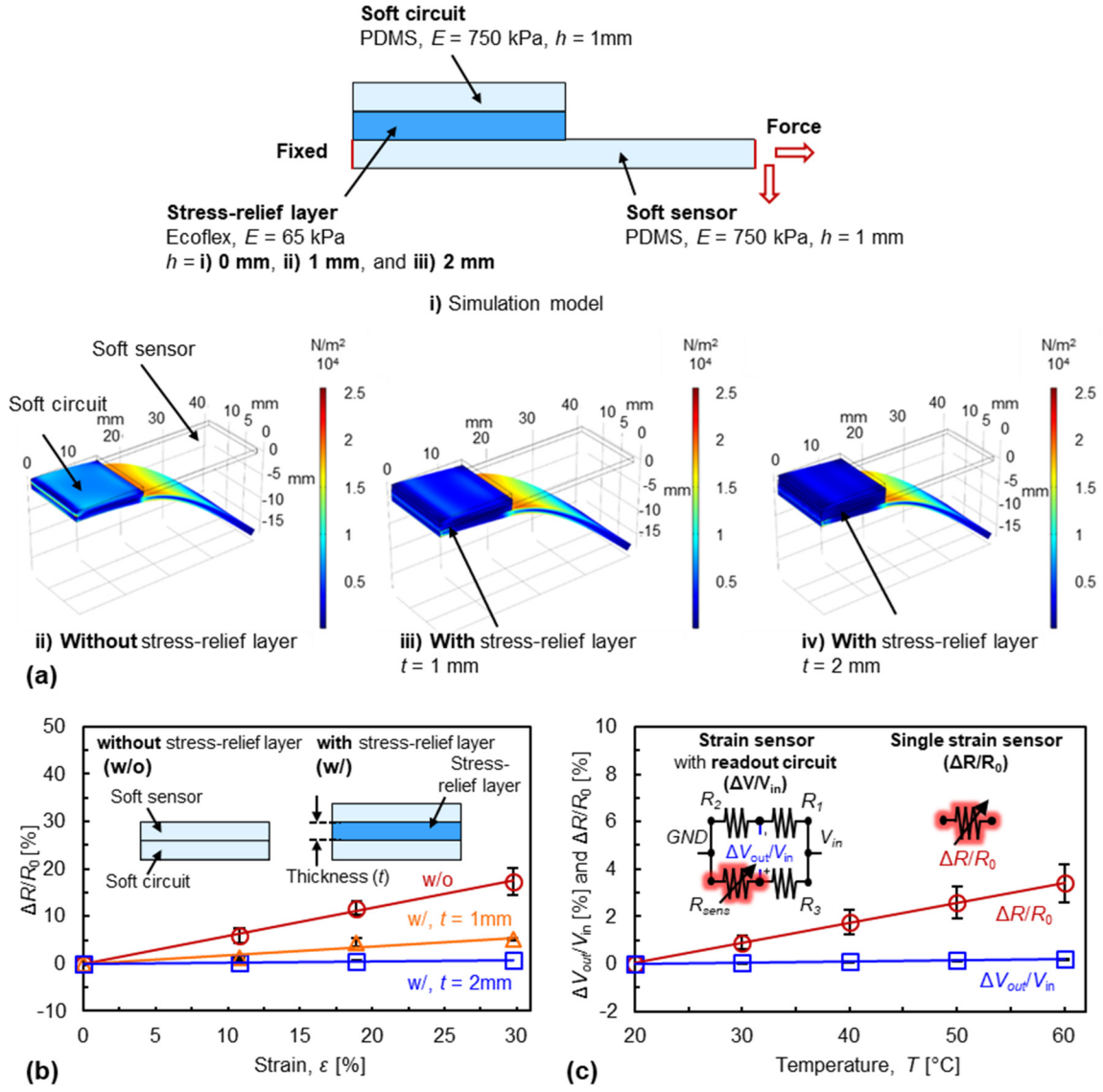

Figure 5.5 (a) Finite element simulations to evaluate the stress-blocking effect under bending and stretching deformation using stress-relief layers with different thicknesses: i) simulation model, ii) without a stress-relief layer, iii) with a 1-mm-thick stress-relief layer, and iv) with a 2-mm-thick stress-relief layer; (b) Measured relative resistance change of the resistors of the soft Wheatstone bridge circuit as a function of the applied uniaxial strain to the soft sensor with/without stress-relief layer having different layer thicknesses; (c) Measured relative output voltage change ($\Delta V_{out}/V_{in}$) of the strain sensing microsystem and measured relative resistance change ($\Delta R/R_0$) of the single strain sensor as a function of the surrounding temperature.

5.2.4 *System-Level Strain Sensing Performance*

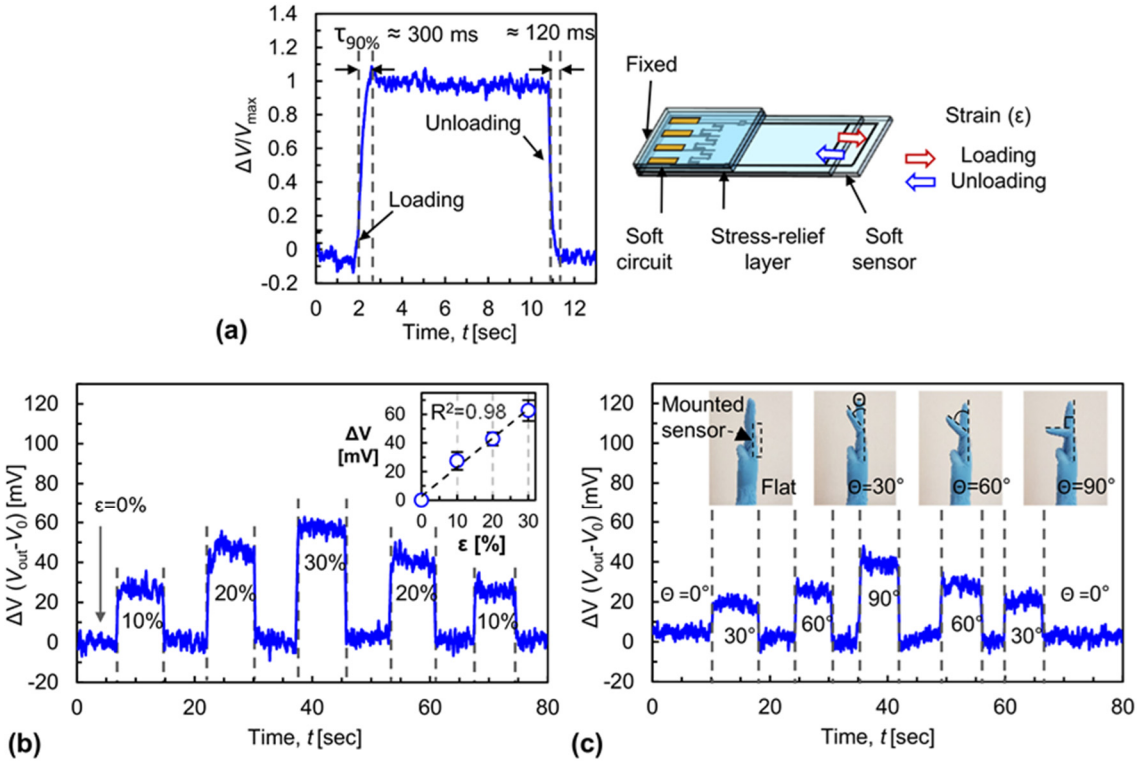

Figure 5.6 (a) Normalized output voltage change of the integrated soft microsystem under loading and unloading conditions; Measured output voltage change of the soft microsystem as a function of time subject to (b) different uniaxial strains and (c) different bending angles of the proximal-interphalangeal joint of an index finger.

Utilizing the benefits of the stress-relief layer and the integrated temperature compensation, the system-level strain sensing performance of microsystems with a 2-mm-thick stress-relief layer was investigated. To evaluate a transient sensor response, Figure 5.6 (a) shows the output voltage change of the microsystem normalized to the maximum output voltage change ($\Delta V/\Delta V_{max}$) as a function of time while loading and unloading the sensor (10% - 30% uniaxial strain). Because of the viscoelastic nature of the elastomeric materials, there is a response delay exhibited by all elastomer-based strain sensors [39]. In the present study, the measured response and recovery times ($\tau_{90\%}$) were 346±56 ms and

150±32 ms for the loading and unloading case, respectively, which are comparable to those of PDMS-based resistive strain sensor reported in the literature [39].

To evaluate system linearity and hysteresis, Figure 5.6 (b) shows the measured output voltage change (ΔV) over time while sequentially loading and unloading the sensor at different uniaxial strain levels. Over the range of the applied strain up to 30%, ΔV increases almost linearly with a little hysteresis during the recovery process. Finally, the soft strain sensing microsystem was mounted on an index finger using adhesive tape, and we measured the output voltage change ΔV at different bending angles of the proximal-interphalangeal joint of an index finger, as shown in Figure 5.6 (c). As expected, ΔV increased with the bending angle as a result of the bending and stretching deformation, which demonstrates the usefulness of the system to gain information on finger motions and gestures. The measured ΔV at a bending angle of 90° corresponds to an average strain of 24.2±1.9%. This strain value is comparable with those reported in the literature [39, 42], and the underlying resistive sensing elements showed high durability under multiple (>500 times) bending and twisting deformations without noticeable degradation [79].

5.3 Fingertip Microsystems for Simultaneous Proximity, Touch, and Pressure Measurements

5.3.1 Design and Fabrication of Fingertip Microsystems

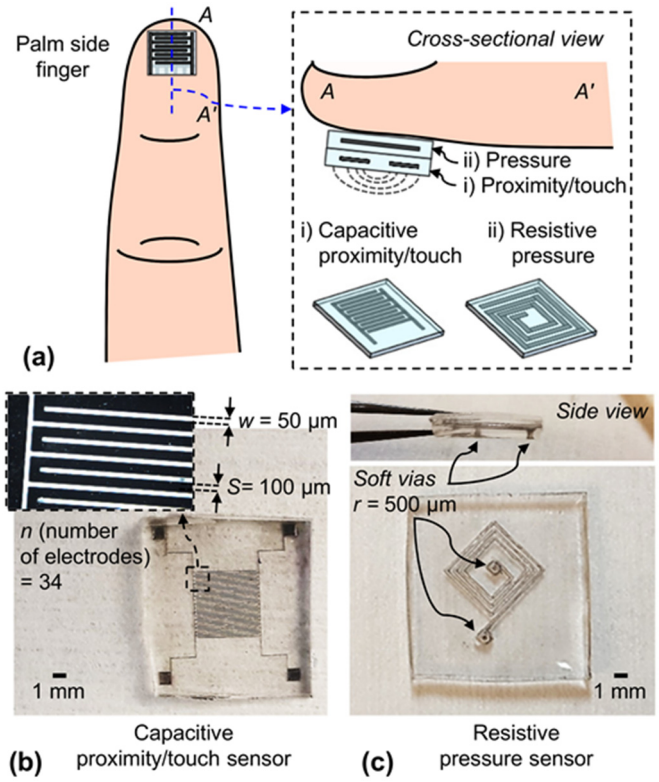

Figure 5.7 (a) Schematic illustration of 3D-integrated fingertip microsystems with capacitive proximity and touch and resistive pressure sensing capabilities; (b)-(c) Fabricated capacitive sensor and resistive sensor.

3D-integrated microsystems enable not only high-density integration but also multifunctional sensing capability. In the human skin, the fingertip is one of the most sensitive areas that can collect high-resolution pressure information [1, 99]. Figure 5.7 (a) shows the schematic illustration of a 3D-integrated fingertip microsystem with capacitive proximity/touch sensing and resistive pressure sensing capabilities to collect a wide-range of proximity, touch, and pressure information. By employing complementary sensing

principles, i.e. capacitance-type sensors for proximity/touch detection and resistive-type sensors for pressure detection, crosstalk effects between the sensors can be minimized while enhancing the sensitivity and functionality. Figures 5.7 (b) and (c) show the fabricated capacitive proximity sensor (line width (w) = 50 μm, line spacing (s) = 100 μm, and number of interdigitated electrode (n) = 34) and the resistive pressure sensor (line width (w) = 500 μm and thickness (t) = 800 μm), respectively. The detailed device designs and dimensions of the soft capacitive and resistive sensors are shown in Appendix B2.

Figure 5.8 (a) shows the 3D-integrated fingertip microsystem with an effective sensing area of 6 mm × 6 mm, where the capacitive sensor is integrated on top of the resistive sensor with soft vias being employed for vertical interconnection. The fabricated soft microsystem was mounted on the fingertip of an index finger for simultaneous proximity, touch, and pressure sensing, as shown in Figure 5.8 (b).

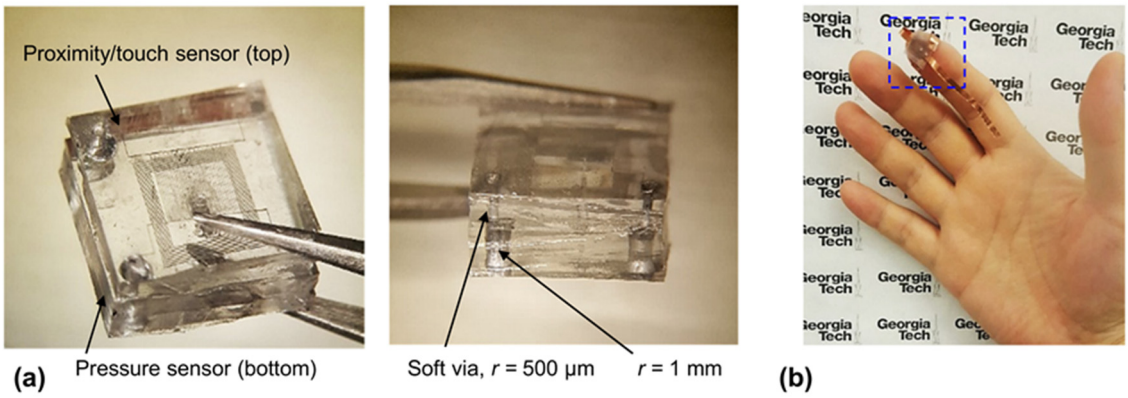

Figure 5.8 (a) Vertically integrated fingertip microsystem; (b) Fingertip microsystem for proximity, touch, and pressure sensing mounted on the fingertip of an index finger.

5.3.2 *Electrical and Mechanical Characterization*

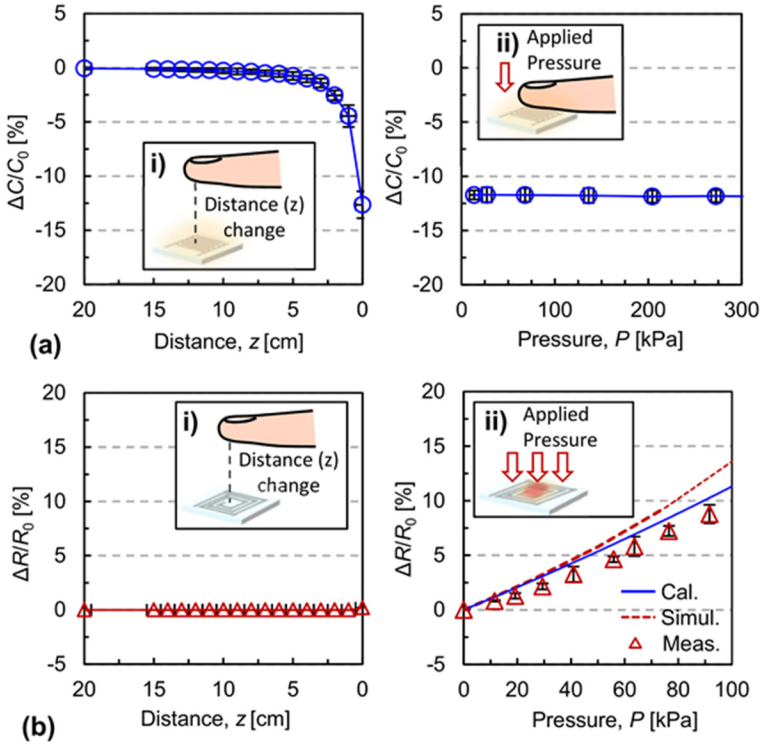

Figure 5.9 (a) Measured relative capacitance change as a function of i) fingertip distance in z-direction and ii) applied pressure for capacitive proximity and touch sensing; (b) Measured relative resistance change as a function of i) fingertip distance in z-direction and ii) applied uniform pressure for resistive pressure sensing and comparison with calculated and simulated behavior.

Again, each sensor was fabricated using the subtractive reverse stamping process highlighted in Chapter 2. The fabricated sensors were subsequently characterized by approaching a fingertip to both sensors for proximity and touch detection and by pressing onto the sensors for pressure detection. Figure 5.9 (a) shows the measured relative capacitance change ($\Delta C/C_0$) as a function of i) the fingertip distance in the z-direction for proximity and touch sensing and ii) the applied pressure for capacitive pressure sensing. As human skin or properly grounded conductors get closer to the capacitive sensor, the fringing electric field generated by the interdigitated capacitor is partially disturbed or

shunted, consequently decreasing the measured capacitance [105, 106]. The measured $\Delta C/C_0$ decreases to -12.6% when the fingertip slightly touched the sensor. However, this capacitive sensor was insensitive to applied pressure because the capacitance change caused by the disturbed electric field is much higher than that caused by the physical deformation in the interdigitated structure. On the other hand, the resistive pressure sensor shows complementary sensing characteristics to the capacitive sensor. Figure 5.9 (b) shows the measured relative resistance change ($\Delta R/R_0$) as a function of i) the fingertip distance change in the z-direction for proximity and touch sensing and ii) the applied uniform pressure for resistive pressure sensing. As expected, the resistance does not change when the finger approaches the sensor. However, pressing the sensing area (1 cm x 1 cm) decreases the cross-sectional area of the microchannel, resulting in an increase in its resistance. The 2D analytical model given in Equation (5) [35, 107] and 3D numerical simulations using COMSOL (COMSOL Multiphysics and Figure 5.10) were used to evaluate $\Delta R/R_0$ as a function of the applied pressure.

$$\frac{\Delta R}{R} = \frac{1}{1 - 2(1 - \upsilon^2)wp\chi/Et} - 1 \tag{5}$$

where p is the applied pressure and χ is a correction factor determined by the lateral offset x between the centerlines of the EGaIn-filled channel and the applied pressure and the distance z from the elastomer surface to the EGaIn surface (Figure 5.10 (a)).

Under the condition that the EGaIn-filled channel is close to the center of the applied pressure ($|x| < a/2$ and $z < a$, where a is the width of the pressure distribution) [107], the calculated correction factor is 0.86 in this analytical model (Figure 5.10 (a)). Finite element simulations were also conducted to evaluate structural deformations and resistance changes

using the fluid-structure interaction physics. Figure 5.10 (a) shows the simulation model and boundary condition: the liquid metal sensor was surrounded by the PDMS chip, the bottom surface of the chip was fixed, and a boundary load with different pressures was applied to the top surface of the soft sensor to apply a uniform deformation (see Figure 5.10 (b)-(d)). Figure 5.9 (b)-ii compares $\Delta R/R_0$ as obtained from Equation (5) and from the 3D numerical simulations (Figure 5.10 (b)-(d)) with the experimental data. Both calculated, simulated, and measured $\Delta R/R_0$ as a function of the applied pressure generally follow a very similar trend over the tested pressure range with a small deviation. We believe that model simplifications, such as the 2D nature of the analytical model and the simplified 3D numerical model, are the main reason for the deviation.

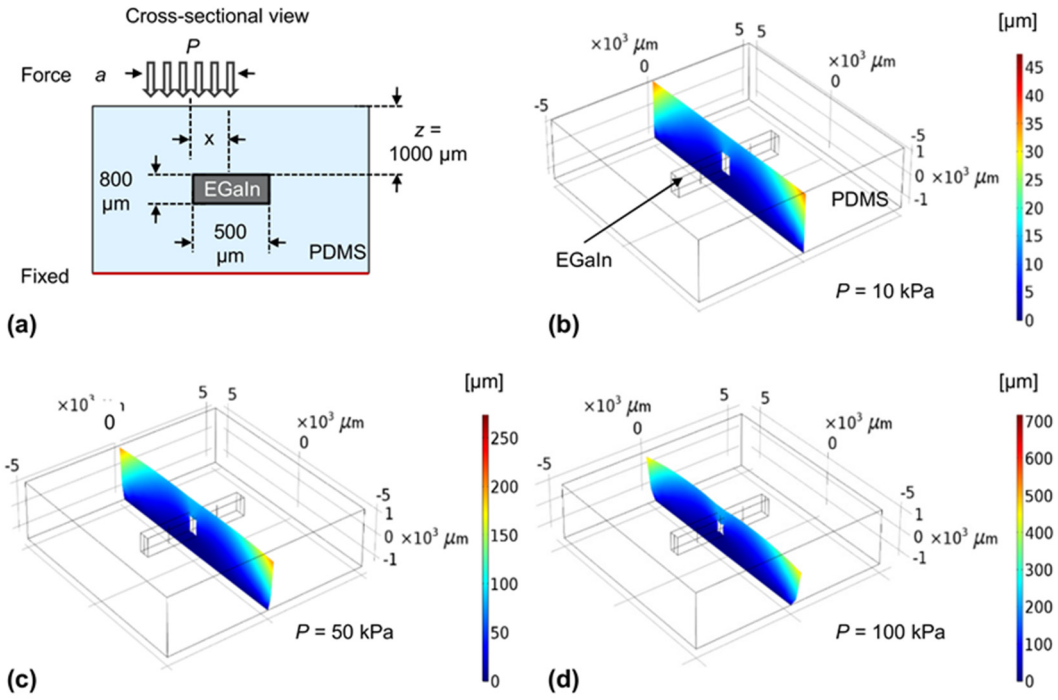

Figure 5.10 Finite element simulations to evaluate the structural deformation and resulting resistance changes with different applied pressure. The bottom surface of the sensor is fixed, and boundary loads are applied to the top surface (1 cm x 1 cm) to apply uniform pressure: (a) geometry, material information, and boundary conditions and (b)-(d) deflection of the EGaIn-filled PDMS channel subject to pressures of 10 kPa, 50 kPa, and 100 kPa, respectively.

5.3.3 *System-Level Proximity, Touch, and Pressure Sensing*

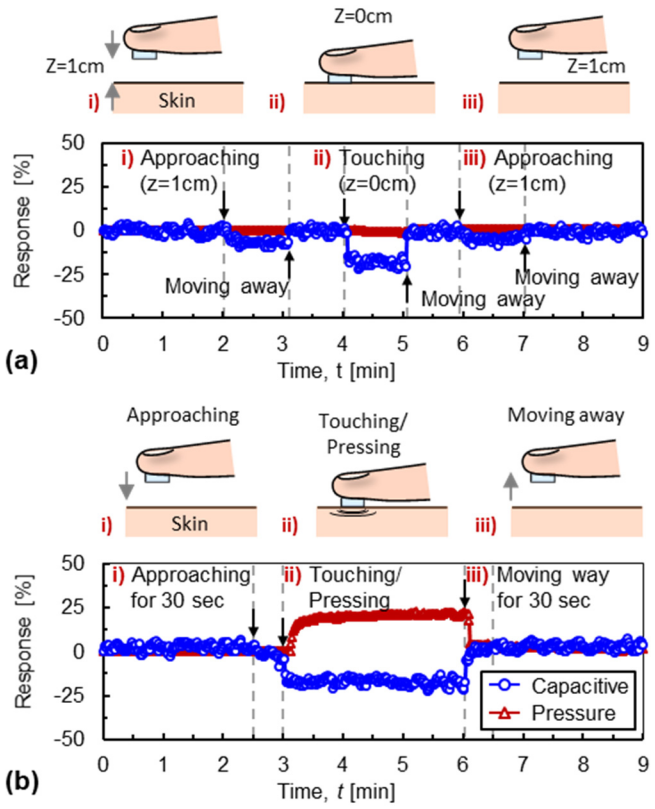

Figure 5.11 Fingertip sensing performances for (a) approaching and touching detection and (b) approaching, touching, and pressing detection.

The integrated fingertip sensing microsystem was finally mounted on the fingertip of an index finger using adhesive tape, and we measured the capacitive and resistive responses simultaneously, as shown in Figure 5.11 (a) and (b). Two different tests were performed using the 3D-integrated fingertip microsystem: (a) approaching (z = 1 cm for 1 minute and moving away) and touching (z = 0 cm for 1 minute and moving away) and (b) approaching, touching, and pressing by a finger or properly grounded conductive surfaces (slowly approaching for 30 seconds, touching and pressing for 3 minutes, and slowly moving away from the object for 30 seconds). In the case of (a), the measured capacitance decreased when the fingertip-mounted sensor is approaching human skin and further

decreased after touching the human skin. The measured resistance does not change, as expected. On the other hand, in the case of (b), the measured capacitance decreased when the fingertip sensor is approaching and touching the human skin, but then maintained the capacitance value after pressing the fingertip sensor. However, the measured resistance increased after pressing the fingertip sensor, and then returned to the initial resistance value when the fingertip sensor was removed from the object. By utilizing these complementary sensing performances, we can collect a wide-range of proximity, touch, and pressure information with/without physical contact of the fingertip for e-skin applications.

5.4 Conclusion

This chapter reports 3D-integrated and multifunctional all-soft physical microsystems based on EGaIn and PDMS and demonstrated skin-mountable and wearable electronics for e-skins with strain, proximity, touch, and pressure sensing performances. A vertical integration approach for soft physical microsystems using soft vias facilitates high-density integration, multifunctional sensing capabilities, as well as system-level flexibility and stretchability. Considering the demonstrated high-density and multifunctional soft physical microsystems, the proposed fabrication and integration approaches have the potential for all-soft and highly integrated wearable microsystems for human-machine interfaces, soft robotics, and healthcare applications.

CHAPTER 6. ALL-SOFT CHEMICAL MICROSYSTEMS

6.1 Motivation

With a growing demand for soft and epidermal electronics, soft and wearable microfluidic sensing platforms have attracted significant attention for healthcare and environmental monitoring [6, 15]. Considering Internet of Things (IoT) applications, wearable sensing platforms enable network connections between users and soft devices without physical wires and bulky batteries [108].

Unlike conventional solid-state sensors, soft electronics would allow a user to change a device's shape as needed, such as skin patches for personal electronics [109]. Therefore, a variety of soft materials and their processing techniques have been investigated for the design and fabrication of soft and wearable sensing platforms [24, 98]. One promising approach is to use EGaIn and PDMS. Thanks to its excellent electrical and mechanical properties, EGaIn-based environmental sensors have been investigated for sensing heavy metal ions, temperature, humidity, and oxygen level [52, 54, 56]. However, because of technical challenges associated with EGaIn patterning and integration, all-soft and wireless chemical sensing microsystems have not yet been demonstrated.

In this chapter, the aim of the research is to develop EGaIn-based all-soft sensing platforms for detection of liquid-phase and gas-phase volatile organic compounds (VOCs) using the same device and demonstrate battery-free and wireless sensing using a 3D-integrated, all-soft inductive-capacitive (*LC*) sensor and a soft readout coil. In the case of liquid-phase chemical sensing, the wireless VOC sensing performance and microfluidic capacitance tuning capability are demonstrated for different dielectric liquids using

analytical, numerical, and experimental approaches. In the case of gas-phase chemical sensing, the sensing performance of the soft sensor is evaluated using different alcohols as analytes and compared to that of a silicon-based, solid-state gas sensor using a PDMS sensing film [110, 111].

6.2 Soft Microfluidic Chemical Sensing Platforms

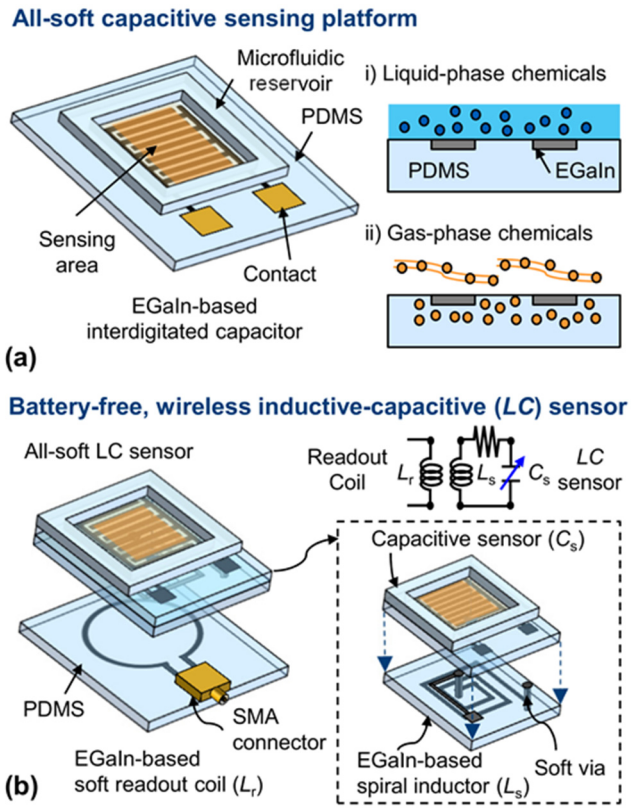

Figure 6.1 (a) All-soft microfluidic chemical sensing platform using EGaIn and PDMS for liquid-phase and gas-phase VOC detection and (b) 3D-integrated, all-soft *LC* passive sensor and soft readout coil for wireless sensing and battery-free operation.

Figure 6.1 (a) shows the all-soft microfluidic capacitive sensing platform, which comprises an EGaIn-based interdigitated capacitive sensor and a PDMS microfluidic reservoir, for liquid-phase and gas-phase VOC detection. The EGaIn-based interdigitated

capacitor is fabricated on a PDMS mold using the reverse stamping technique based on soft lithography and covered with a PDMS microfluidic reservoir with 136.5 µL fluid capacity. The patterned EGaIn interdigitated electrodes were in direct contact with the applied liquid-phase and gas-phase analytes. A passive *LC* sensing platform, comprising a resonant *LC* tank, enables wireless sensing and battery-free operation by inductive coupling between an external readout coil and the inductor [90]. Figure 6.1 (b) shows the 3D-integrated, all-soft *LC* sensor, which is interrogated by an EGaIn-based soft readout coil for wireless sensing of the parameter of interest. The soft *LC* sensor consists of the capacitive sensing component and an EGaIn-based spiral inductor, which is vertically integrated using a soft via.

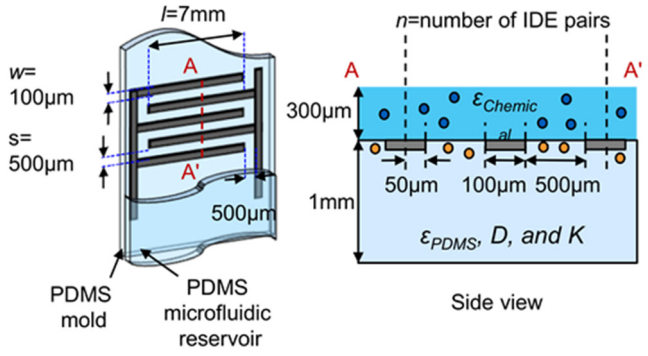

Figure 6.2 Design of EGaIn-based, all-soft interdigitated capacitor for analytical evaluation.

For the design and analytical evaluation of the capacitive sensing component (C_S), a conformal mapping technique was employed, which provides a closed-form expression for the capacitance as a function of the media's relative permittivity by transforming the coplanar line geometry to a parallel-plate structure [90]. Figure 6.2 shows a schematic of the EGaIn-based interdigitated capacitor, which features 100 µm wide (*w*) interdigitated electrodes (IDE) with 500 µm wide gap (*s*) in between the electrodes, in a PDMS mold.

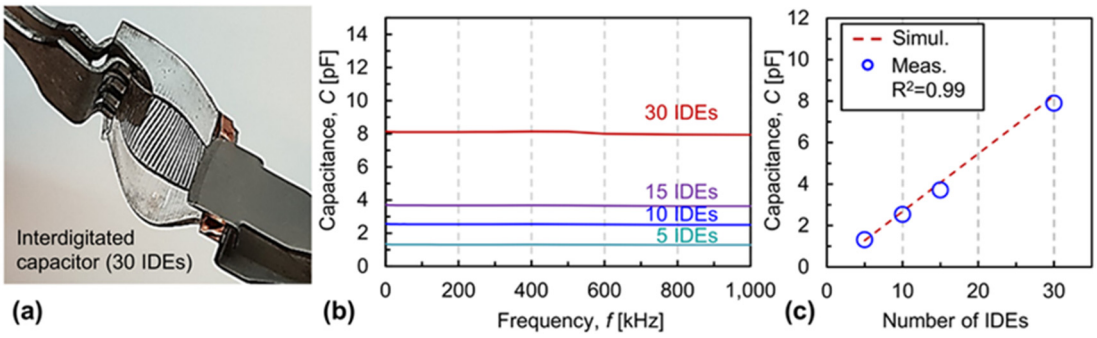

Figure 6.3 (a) Photograph of fabricated interdigitated capacitor; (b) Measured capacitance as a function of frequency up to 1MHz for capacitors with different number of interdigitated electrodes (IDEs); (c) Simulated and measured capacitance as a function of a number of IDEs.

The interdigitated capacitor was fabricated using the subtractive reverse stamping technique introduced in Chapter 2. The total capacitance is the sum of the line capacitance without surrounding dielectrics C_{IDE}, the line capacitance with a dielectric substrate $C_{\mathrm{substrate}}$, and the sensing capacitance with a chemical layer C_{sens}, expressed as [90]:

$$C_{\mathrm{s}} = nl(C_{\mathrm{IDE}} + C_{\mathrm{substrate}} + C_{\mathrm{sens}}) \tag{6}$$

$$C_{\mathrm{IDE}} = 4\varepsilon_0 \frac{K(k_1')}{K(k_1)} \tag{7}$$

$$C_{\mathrm{substrate}} = 2\varepsilon_0(\varepsilon_{\mathrm{substrate}} - 1)\frac{K(k_2')}{K(k_2)} \tag{8}$$

$$C_{\mathrm{sens}} = 2\varepsilon_0(\varepsilon_{\mathrm{chem}} - 1)\frac{K(k_3')}{K(k_3)} \tag{9}$$

where n is the number of IDE pairs, l is the overlapping length, and $K(k_1')/K(k_1)$, $K(k_2')/K(k_2)$, $K(k_3')/K(k_3)$ are the ratios of complete elliptical integrals of air, substrate, and sensing film based on the geometric parameters, respectively. The calculated $K(k_1')/K(k_1)$,

$K(k_2')/K(k_2)$, $K(k_3')/K(k_3)$ are 0.33, 0.33 and 0.29, respectively [90]. ε_0, $\varepsilon_{substrate}$, and ε_{chem} represent the permittivity of free space, substrate and applied chemical, respectively.

Equations (6)-(9) relate the measured capacitance to the geometric parameters of the sensor and the properties of the chemicals applied to the microfluidic reservoir. The electrical characteristics of the EGaIn-based interdigitated capacitor were investigated using both numerical and experimental approaches. Figure 6.3 (a) shows a fabricated interdigitated capacitor, which has 30 interdigitated electrodes (IDEs) with 100 μm width and 500 μm spacing, embedded in the PDMS substrate. Interdigitated capacitors ranging from 5 up to 30 IDEs were fabricated. Figure 6.3 (b) shows the measured capacitance as a function of frequency up to 1MHz for capacitors with different number of IDEs using an LCR meter (Agilent 4284A). The measured capacitance of the capacitor with 5 IDEs was 1.3 pF and linearly increased to 7.9 pF for the capacitor with 30 IDEs, demonstrating how capacitors with a range of capacitances can be designed by adjusting the number of IDEs. To predict the capacitance values of the interdigitated capacitors, finite element modeling was used using COMSOL Multiphysics (COMSOL Inc., Burlington MA). The modeled interdigitated capacitor was surrounded by the PDMS chip, and the electrostatic physics model was used for the simulation. Figure 2.11 (c) compares the measured and simulated capacitance for capacitors with different number of IDEs. The measured capacitances agreed well with the simulated capacitances with <5.2% deviation.

The interdigitated capacitor was then integrated with the microfluidic reservoir for liquid- and gas-phase chemical analysis. In the case of liquid-phase chemical sensing, the relative permittivity of the applied chemicals is the dominant factor, resulting in linear capacitance changes as a function of the applied relative permittivity. In the case of gas-

phase chemical sensing, however, PDMS is used both as a substrate and a sensing film. Therefore, additional parameters, such as the diffusion coefficient D and the partition coefficient K of the analyte in the PDMS, must be considered for the evaluation of the gas sensing performance.

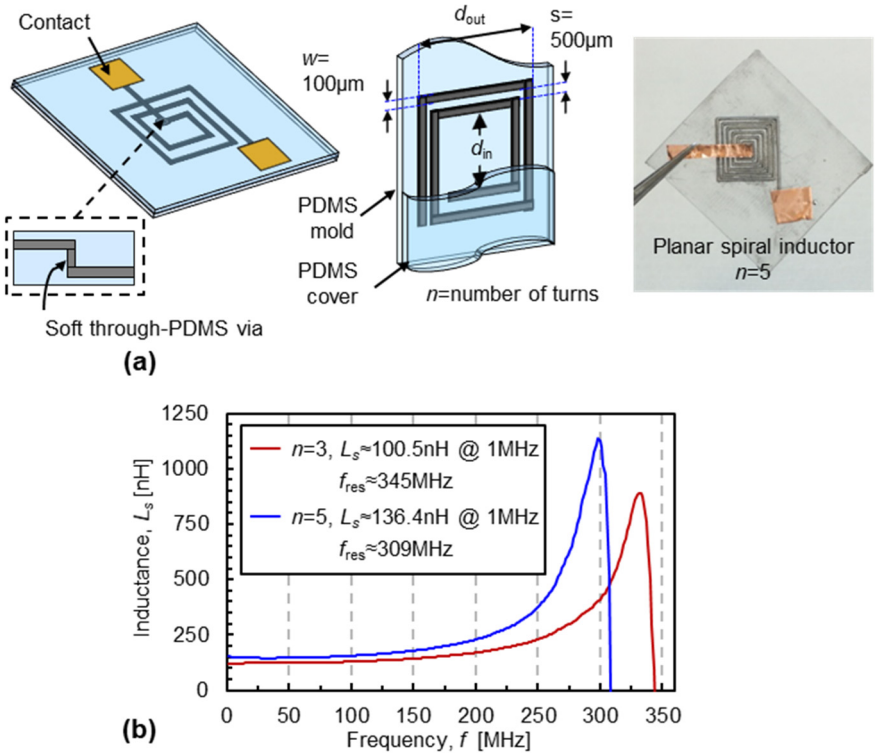

Figure 6.4 (a) Schematic and photograph of fabricated EGaIn-based, all-soft planar spiral inductor and (b) measured inductance for coils with different number of turns as a function of frequency.

To form the all-soft LC sensor, an EGaIn-based planar spiral inductor (L_s) is designed to interrogate with the soft readout coil (L_r) for wireless sensing. For the design and analytical evaluation of the planar spiral inductor, we employed a modified Wheeler formula, specified by the number of turns n and the coil inner and outer diameter din and dout, expressed as [89, 90]:

$$L_s = K_1 \mu_0 \frac{n^2 d_{avg}}{1 + K_2 \rho} \quad (10)$$

where L_s is the total inductance, d_{avg} is the average diameter (= 0.5(d_{out} + d_{in})), and ρ is the fill ratio, defined as ρ = (d_{out} - d_{in})/(d_{out} + d_{in}). The layout dependent coefficients K_1 and K_2 are 2.34 and 2.75 for the square structure, respectively [89].

Figure 6.4 (a) shows schematic and photograph of a fabricated all-soft, EGaIn-based planar spiral inductor. The spiral inductor is formed by a 100 μm wide conductor (w) and 500 μm wide gaps (s) in between the lines, fabricated using the same subtractive reverse stamping technique as the interdigitated capacitor. Inductors with different number of turns (n = 3 and 5) were designed with d_{out} <10 mm and d_{in} >2 mm. The measured inductance of each inductor increases as the frequency increases and reaches a maximum value due to self-resonance, as shown in Figure 6.4 (b). The measured inductances at 1MHz were 100.5 nH for the coil with 3 turns and 136.4 nH for the coil with 5 turns, both obtained using a network analyzer (Rohde&Schwarz, ZVB 4) and matched well with calculated values from Equation (10) with an average 14.6% deviation. Also, the measured self-resonance frequencies (f_{res}) for both inductors were >300MHz. The detailed device designs and dimensions of the soft interdigitated capacitor and planar spiral inductor are shown in Appendix B3.

6.3 Liquid-Phase Chemical Sensing

6.3.1 Liquid-Phase Volatile Organic Compounds (VOC) Sensing

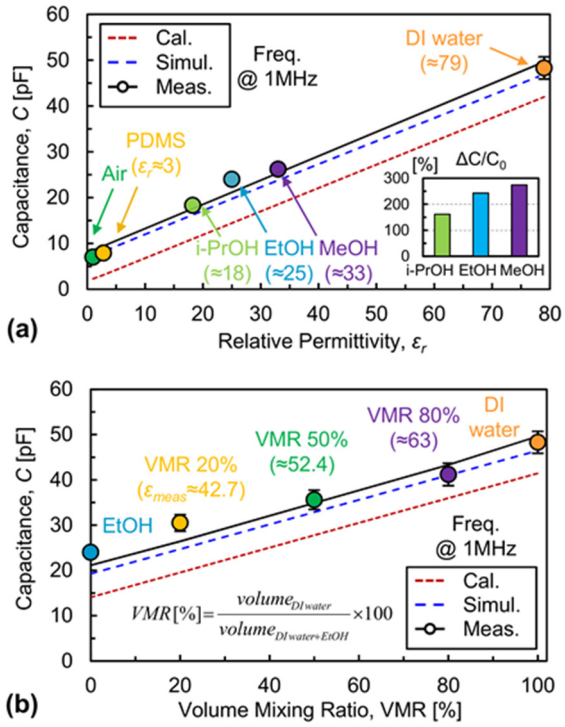

Figure 6.5 (a) Calculated, simulated, and measured capacitance (for isopropanol (i-PrOH), ethanol (EtOH), and methanol (MeOH)) as a function of the relative permittivity of the applied liquid analyte; (b) Calculated, simulated, and measured capacitance as a function of the volume mixing ratio (VMR) of DI water in ethanol.

The soft capacitive sensing platform with 30 IDEs was investigated for liquid-phase VOC detection by applying different solvents, such as isopropanol (i-PrOH, relative permittivity $\varepsilon_r \approx 18$ at room temperature and 1kHz probing frequency), ethanol (EtOH, $\varepsilon_r \approx 25$), and methanol (MeOH, $\varepsilon_r \approx 33$), which were directly in contact with the EGaIn electrodes. As these alcohols have different relative permittivity, they can be selectively detected by measuring the capacitance when the injected liquid volume is constant (100 μL). Because of the pH-neutral property of the tested solvents, thin surface oxides that

formed on the EGaIn electrodes were unimpaired, and the overall shape of the device was maintained even with liquid contact. However, the EGaIn-based capacitive sensing platform is not suitable for acids and bases as the oxide layer can be removed by acids (pH<3) or bases (pH>10), causing the liquid metal to bead up because of the large surface tension of EGaIn [24, 25]. However, in this case, the EGaIn electrodes could potentially be protected by another polymer layer. For proof-of-concept and to demonstrate the wide-range capacitance tunability, we also measured the sensor capacitance in air ($\varepsilon_r = 1$), PDMS ($\varepsilon_r \approx 3$) and deionized (DI) water ($\varepsilon_r \approx 79$).

Figure 6.5 (a) shows the calculated, simulated, and measured capacitance by introducing dielectric liquids having different relative permittivity. Both 3D simulated (COMSOL Multiphysics) and calculated (using Equation (6) - (9)) capacitances increase similarly with increasing permittivity but are slightly offset. The calculated capacitance has an offset of approximately 6.9 pF from the measured values, which can be explained by parasitic capacitances. The simulated capacitance, on the other hand, matches the measured capacitance quite well, with an average 11.2% deviation. The initial capacitance in air (30 IDEs at 1MHz) was 7.0 pF and increased to 18.3 pF with isopropanol (161% change), 24.0 pF with ethanol (243% change), and 26.2 pF with methanol (274% change). Overall, the measured capacitance linearly increases with the relative permittivity of the liquid from 7.0 pF in the air as a reference to almost 50 pF in the case of DI water, demonstrating the wide-range tuning capability of the microfluidic capacitor.

To address the dielectric properties of unknown liquids, the capacitive sensing platform was also investigated by applying mixtures with different volume mixing ratio (VMR), as shown in Figure 6.5 (b). The mixtures were prepared by diluting DI water with

ethanol to obtain 20% ($\varepsilon_{cal} \approx 35.8$), 50% ($\varepsilon_{cal} \approx 52$), and 80% ($\varepsilon_{cal} \approx 68.2$) VMR. The effective permittivity is calculated by the Looyenga formula based on the VMR in the mixture without chemical reactions [112]. As expected, the measured capacitance linearly increases with the VMR, and the extracted relative permittivity (ε_{meas}) of 20%, 50%, and 80% VMR were 42.7, 52.4, and 63, respectively. This measured relative permittivity agreed well with the simulated permittivity, with an average 9.2% deviation.

6.3.2 Battery-Free and Wireless Interrogation for Liquid-Phase VOC Sensing

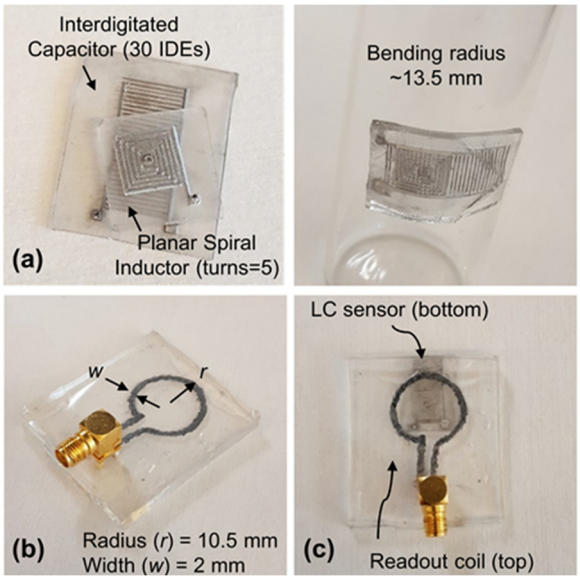

Figure 6.6 (a) Fabricated 3D-integrated, all-soft *LC* sensor components, and assembled *LC* sensor attached to a circular object, (b) fabricated soft readout coil, and (c) physical alignment for wireless interrogation.

Using the capacitive chemical sensing platform, a 3D-integrated, all-soft *LC* sensor is constructed for battery-free and wireless interrogation. As the sensing capacitance changes in response to applied solvents, the resonant frequency of the *LC* tank shifts. The soft readout coil is inductively coupled to the inductor in the *LC* sensor, and the resonant frequency (f_{res}) of the sensor is detected by monitoring the impedance phase ($\angle Z_{in}$) or the

input return loss (S_{11}) of the readout coil. Figure 6.6 (a) shows the fabricated interdigitated capacitor (30 IDEs, $C \approx 7.3$ pF at 1MHz in air) and planar spiral inductor (5 turns, $L \approx 130$ nH at 1MHz), which form the vertically integrated resonant *LC* tank. Made solely of soft materials (EGaIn and PDMS), the fabricated *LC* sensor shows flexible and stretchable characteristics, which is demonstrated by bending the sensor around a circular cylinder. Figure 6.5 (b) shows the fabricated EGaIn-based soft readout coil with a radius of 10.5 mm, which has an SMA connector for the connection to a network analyzer (Rohde&Schwarz, ZVB 4). The readout coil was physically aligned and in contact with the planar spiral inductor of the LC sensor for wireless interrogation, as shown in Figure 6.6 (c).

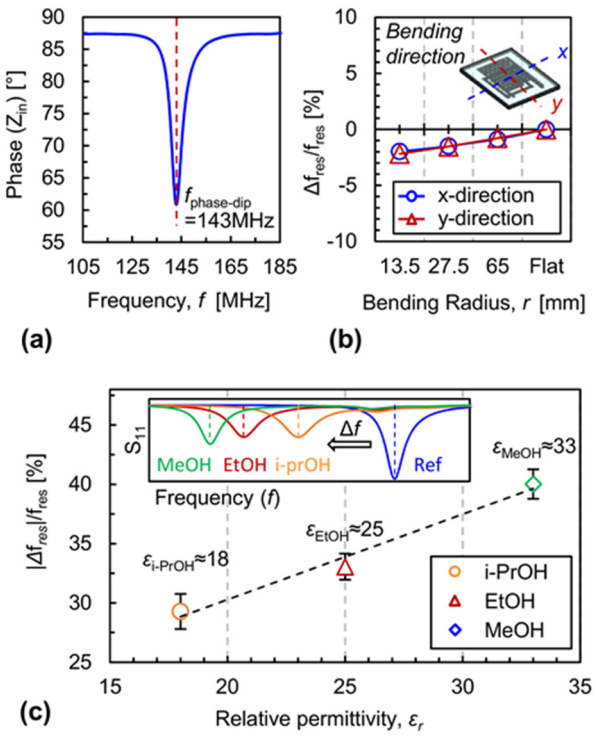

Figure 6.7 (a) Measured phase of input impedance as a function of frequency for the *LC* sensor without dielectric liquid, (b) measured relative frequency changes as a function of bending radius, and (c) measured relative frequency changes as a function of the relative permittivity of the applied solvents with the S_{11} parameter as a function of frequency as insert.

Figure 6.7 (a) shows the measured phase of the input impedance as a function of frequency without dielectric liquid as a reference. The measured resonance frequency was 143MHz, with <12% deviation from the calculated value obtained by [90]:

$$f_{\text{res}} = \frac{1}{2\pi\sqrt{LC}} \tag{11}$$

where f_{res} is the resonance frequency, L is the inductance, and C is the capacitance.

To investigate the electrical characteristic of the *LC* sensor under bending deformation, circular cylinders with different radii were prepared, and the resonance frequency was measured while bending the sensor along the width (x-direction) and length (y-direction) direction. Figure 6.7 (b) shows the measured resonance frequency changes as a function of the bending radius of the cylinders. Overall, this bending deformation has a minor effect on the resonance frequency of the *LC* sensor, with <2.2% relative resonance frequency changes in both width and length direction. The measured resonance frequency decreases as the bending radius becomes smaller, which can be explained by a slight increase in the capacitance and inductance. Finally, to demonstrate battery-free and wireless interrogation, different alcohols, namely isopropanol, ethanol, and methanol, were injected into the PDMS microfluidic reservoir using a pipette (100 μL). Figure 6.7 (c) shows the magnitude of the relative resonance frequency change (with respect to the frequency without fluid) as a function of the relative permittivity of the solvents. The measured resonance frequency decreases in response to the increasing permittivity of the applied solvents because of the increase of the sensing capacitance, while the inductance is maintained. As a result, the magnitude of the relative frequency change increases almost linearly with the relative

permittivity over the range of tested alcohols, with <3.8% deviation from the calculated values using Equation (11).

6.4 Gas-Phase Chemical Sensing

6.4.1 Gas-Phase VOC Sensing Characterization

The all-soft sensing platform was also investigated for gas-phase VOC detection using PDMS both as substrate and sensing material. The resulting steady-state capacitance change is a function of the relative permittivity and the partition coefficient of the VOC in the PDMS sensing film, as mentioned earlier. In addition, the analyte diffusion coefficient in the sensing film determines the sensor's transient behavior.

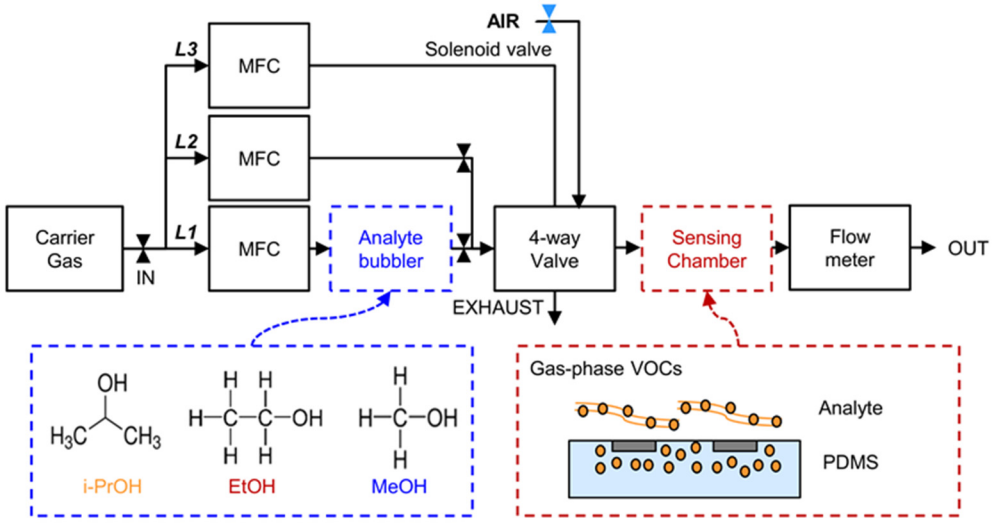

Figure 6.8 Schematic of gas testing setup with mass-flow-controlled (MFC) analyte (*L*1), diluting (*L*2), and reference (*L*3) lines to generate different analyte concentrations and rapidly switch between analyte and reference gas streams using a 4-way valve.

During the measurement, an analyte gas stream with the desired VOC at its saturated vapor pressure, generated by flowing carrier gas through a temperature-controlled

bubbler with analyte-soaked quartz sand, is diluted by a secondary carrier gas stream to change the analyte concentration flowing over the sensor, as shown in Figure 6.8. The total flow rate is kept constant at 80 mL min^{-1}. After each analyte exposure, the measurement chamber was flushed with synthetic air as a reference gas.

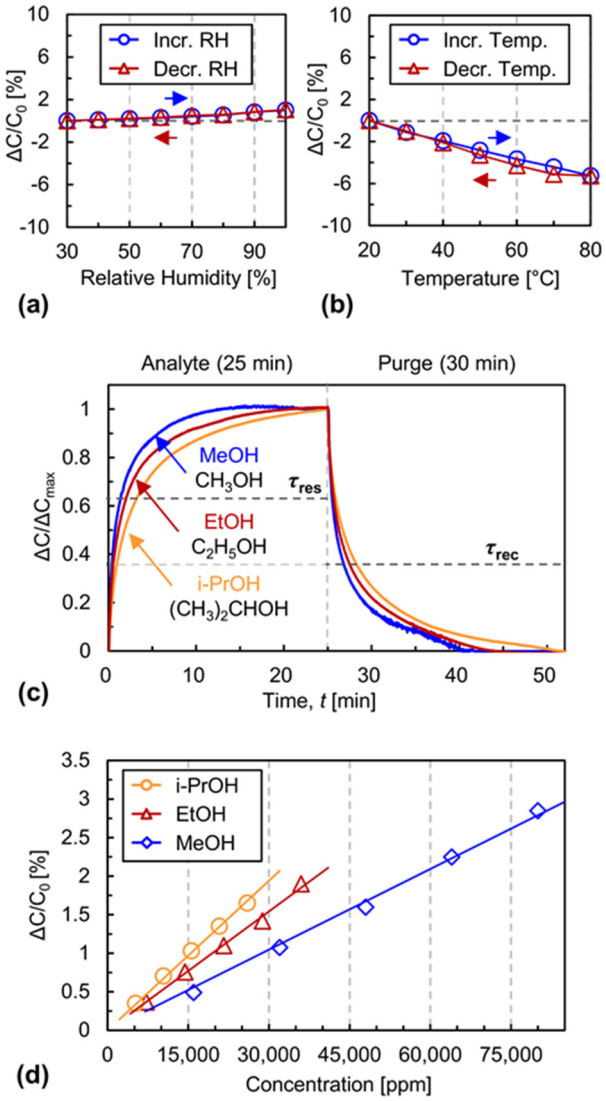

Figure 6.9 (a)-(b) Measured relative capacitance changes as a function of the relative humidity (RH) and the surrounding temperature; (c) Normalized capacitance changes upon exposure to different analytes and (d) relative capacitance changes as a function of the analyte concentrations for isopropanol (i-PrOH), ethanol (EtOH), and methanol (MeOH).

To evaluate environmental influences, Figures 6.9 (a) and (b) show the measured relative capacitance changes as a function of relative humidity (RH) and surrounding temperature, respectively. As expected, the measured capacitance increases with increasing RH because of the large dielectric constant of water, with <1.8% capacitance change when increasing the humidity from 30 to 100% RH. On the other hand, the capacitance decreases with increasing temperature due to the thermal expansion of the PDMS, with <5.8% capacitance change for a 60°C temperature increase. The VOC sensing experiments were carried out at room temperature and close to zero RH.

Figure 6.9 (c) compares the transient sensor responses, i.e. the normalized measured capacitance changes upon exposure to isopropanol, ethanol, and methanol. Upon absorption of the analyte, the change of the effective dielectric constant and the swelling of the PDMS result in a capacitance change. Positive capacitance changes are observed upon analyte sorption because the relative permittivity of the tested analytes is higher than that of PDMS. Analyte-specific response and recovery time constants can be explained by the diffusivity of the different analytes in the PDMS sensing film. For the alcohols tested, the lightest molecule, methanol (CH_3OH), shows the fastest response, while the heaviest molecule, isopropanol ($(CH_3)_2CHOH$), shows the slowest response in both absorption and desorption responses.

Figure 6.9 (d) shows the resulting sensor sensitivities for the three alcohols by displaying the measured relative capacitance changes as a function of the analyte concentrations. The sensor sensitivity is impacted by the partition coefficient K, which gives the ratio of the analyte concentration in the sensing film and analyte concentration in the surrounding gas phase, as well as the relative permittivity of the analyte. The

measurements indicate that the impact of the partition coefficient K for the tested analytes in PDMS ($K_{\text{i-PrOH}} \approx 320$, $K_{\text{EtOH}} \approx 180$, and $K_{\text{MeOH}} \approx 100$ in PDMS [113]) dominates over the contribution from the relative permittivity, as the analyte with the lowest permittivity, isopropanol, exhibits the highest sensitivity. Because isopropanol has the highest partition coefficient of the tested alcohols, it shows the highest sensitivity.

6.4.2 Comparison to Solid-State VOC Gas Sensor

To prove the gas sensing behavior of the soft sensor, a silicon-based capacitive sensor with a PDMS sensing film was fabricated using conventional microfabrication processes and characterized in parallel to the soft sensor. The silicon-based sensor features an interdigitated capacitor (aluminum (Al), t = 200 nm thickness, w = 6 μm, s = 6 μm, n = 167), which is patterned on a silicon wafer covered with a thermally grown silicon dioxide layer (SiO_2, t = 1 μm thickness. A SiO_2 (t = 200 nm thickness) layer was deposited on the interdigitated capacitor for passivation and a PDMS sensing film with a thickness of 5-10 μm in thickness was spin-coated on the sensing area. Table 6.1 summarizes the sensing behavior of the soft sensor and the silicon sensor. The all-soft VOC sensor shows on average x1.65 higher sensitivities than the solid-state sensor, which can be explained by the thick PDMS (t = 1 mm) used both as a substrate and sensing film. This thick PDMS film, however, results in slow response and recovery time constants for the soft sensor compared to the silicon-based sensor. Nevertheless, the all-soft sensor provides flexibility and stretchability, allowing for wearable electronics applications.

Table 6.1. Comparison of VOC gas sensing performance between a solid-state gas sensor and an all-soft gas sensor using PDMS sensing film.

	Solid-state sensor	All-soft sensor
Materials	Substrate: silicon Conductor: aluminum Dielectric: silicon dioxide	Substrate: PDMS Dielectric: PDMS Conductor: EGaIn
Sensing film	PDMS < 10 μm	PDMS ≈ 1 mm
Sensitivity [$\times 10^{-5}$ %/ppm]	Lower sensitivity MeOH: 1.99 EtOH: 3.24 i-PrOH: 3.95	Higher sensitivity: avg. 1.65× times higher MeOH: 3.37 EtOH: 5.14 i-PrOH: 6.59
Time constant for response (τ_{res}) / recovery (τ_{rec}) [min]	Fast response: avg. 17.8× times faster MeOH: 0.08±0.01 / 0.09±0.01 EtOH: 0.13±0.01 / 0.16±0.01 i-PrOH: 0.17±0.01 / 0.22±0.013	Slow response MeOH: 1.45±0.13 / 1.87±0.12 EtOH: 2.12±0.087 / 2.49±0.086 i-PrOH: 3.17±0.12 / 3.44±0.27
Wearability (flexibility and stretchability)	Fragile <1-2% strain Require rigid/hard packaging	Bendable and twistable Soft and lightweight ≈ 0.5 g

6.5 Conclusion

This chapter introduces an all-soft chemical sensing platform for liquid-phase and gas-phase VOC detection. Battery-free and wireless chemical sensing is demonstrated using a 3D-integrated, all-soft LC sensor. In the case of liquid-phase chemical sensing, the wireless VOC sensing capability and capacitance tuning capability were experimentally verified with different dielectric liquids. In parallel, the gas sensing performance was evaluated and compared to that of a solid-state gas sensor using a PDMS sensing film. Thanks to its flexible, stretchable, and lightweight characteristics, this all-soft sensing

platform is suited for wearable sensing applications either on the skin or on clothing and for potential applications in next-generation sensing electronics for the Internet of Everything.

Future work includes improving sensitivity, selectivity, and response/recovery times for the all-soft gas sensor. Faster response/recovery times can be achieved by employing thinner sensing films. However, a trade-off involves high sensitivity or fast response/recovery time. Therefore, optimized sensing layers with more effective capacitive sensing geometry should be investigated. The selectivity may be improved by employing multiple sensing films in all-soft and multifunctional sensor arrays.

6.6 Acknowledgement

This work was done in collaboration with Georgia Tech's GT-Bionics Laboratory in Electrical and Computer Engineering. Prof. Maysam Ghovanloo and Pyungwoo Yeon assisted with the design, fabrication, and characterization of the soft *LC* sensing platform as well as technical discussion.

CHAPTER 7. ALL-SOFT ENERGY STORAGE DEVICES

7.1 Motivation

Soft energy storage systems are a core technology for powering wearable and skin-mountable electronics [58, 114, 115], as shown in Figure 7.1. Supercapacitors are considered promising mobile energy storage devices because of their ultrafast power supply and long cycle life [60, 116, 117]. However, their relatively low energy density compared to Li-ion batteries is their major limitation [116]. Moreover, conventional supercapacitors are manufactured from hard and brittle materials, which fail at less than 2% strain [8, 59]. Thus, interfacial failure between soft skin and rigid electronics is a major limiting factor for wearable and skin-mountable electronics [2, 118, 119]. As a result, a key consideration for realizing novel supercapacitors for wearable applications is that each electrode component must be soft and conductive without sacrificing electrochemical performance [59, 119]. In this respect, the use of liquid-phase conductors, such as EGaIn, can open a new path for all-soft, deformable, and self-healing electrodes for energy storage device applications because of favorable electrical conductivity and unlimited mechanical stretchability [11, 13, 14]. In addition, nanocarbon materials, such as carbon nanotubes (CNTs), have been actively investigated for improving the energy density in energy storage devices [120-124]. To design high-performance and stretchable electrodes for soft supercapacitors, CNTs should be uniformly integrated on patterned EGaIn electrodes without delamination when it is mechanically deformed. However, combining EGaIn with nanocarbon materials is not straightforward due to the phase separation between the hydrophobic CNT surface and the oxophilic EGaIn surface [25, 124]. Chemically incorporated oxygen functional groups on the surface of CNTs, generating oxidized CNTs (O-CNTs), may provide a solution to utilize the strong interaction between the native oxide

layer (Ga_2O_3) on the surface of EGaIn electrodes and the oxygen functional groups on the CNTs [25, 124].

Based on this motivation, Chapter 7 presents all-soft and liquid-phase supercapacitors based on oxygen functionalized CNT-integrated EGaIn electrodes. Soft and stretchable O-CNT-integrated EGaIn electrodes are enabled by large area EGaIn thin-film patterning on PDMS substrates using an additive stamping process and functionalized EGaIn electrodes with O-CNT via a layer-by-layer (LbL) adsorption technique. To demonstrate soft supercapacitors with a parallel-plate configuration, functionalized soft EGaIn electrodes were vertically integrated with a soft separator, comprising a porous and sponge-like PDMS structure filled with liquid electrolyte, as shown schematically in Figure 7.1. The electrochemical and mechanical properties of the fabricated soft supercapacitors are investigated for integrated soft microsystems applications.

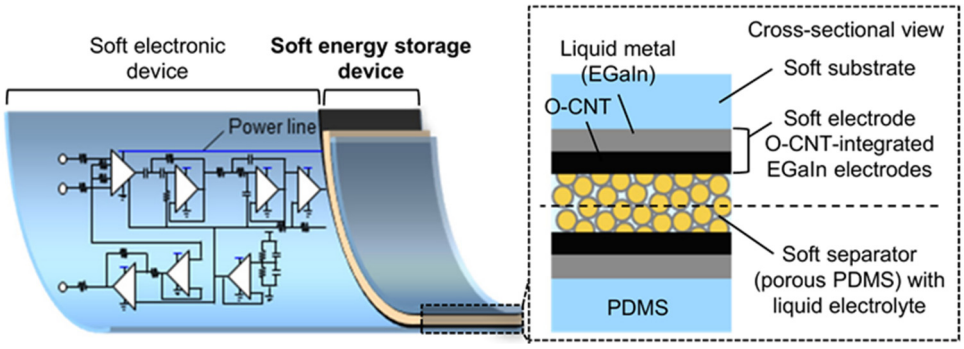

Figure 7.1 Integrated soft microsystems, comprised of soft electronic devices and a soft energy storage element; in the form of an all-soft and liquid-phase supercapacitor, composed of soft electrodes and a soft separator filled with liquid electrolyte.

7.2 Functionalized Liquid Metal Electrodes for Soft Energy Storage Devices

Creating soft and stretchable electrodes, which are electrochemically viable under large deformation, is a fundamental requirement for soft energy storage devices. Figure 7.2 shows the fabrication process for the soft supercapacitors, investigated in this work

comprising i) an additive stamping process based on soft lithography for large-area EGaIn patterning, ii) oxidized CNT (O-CNT) functionalization via a layer-by-layer (LbL) adsorption process, and iii) soft supercapacitor integration to form a parallel-plate configuration. Thereby, the additive stamping approach introduced in Chapter 3 ensures large area (>cm^2) and uniform EGaIn patterning with film thicknesses of ≈ 1.5 μm [84, 85]. The EGaIn patterns serve as electron transport channels and support for the O-CNT adsorption. To enhance the energy density of the electrode, the EGaIn patterns were functionalized by O-CNT. It has been demonstrated that the measured areal capacitance using O-CNT is approximately ten times higher than that of CNT [123, 124]. The high areal capacitance for O-CNT has been attributed to the pseudocapacitance of the oxygen functional groups [123, 124]. O-CNTs were prepared by chemically oxidizing the surface of CNTs using acid treatments for 2 hours [124]. In this study, sub-millimeter-long few-walled CNTs were used, provided by the Noda Laboratory (Waseda University, Japan). Subsequently, O-CNT inks dispersed in ethanol with a concentration of ≈ 0.63 mg mL^{-1} were prepared and subsequently drop casted onto the patterned EGaIn electrodes using a polyimide shadow mask. Multilayer integration was conducted via a layer-by-layer (LbL) adsorption process to enhance the electrochemical performance of the soft supercapacitors [122]. Finally, the O-CNT-functionalized EGaIn electrodes were vertically integrated with a soft separator, comprising a porous and sponge-like PDMS structure filled with liquid electrolyte, to form all-soft and liquid-phase supercapacitors with a parallel-plate configuration [125].

Figure 7.3 (a) shows the PDMS substrates with the paper-textured surface (see Chapter 3 for details on fabrication), used to increase the active surface area and, thus, adhesion between the stamped EGaIn electrode and the soft substrate [84]. Circular-shaped PDMS stamps with diameters ranging from 5 mm to 15 mm were prepared using a conventional PDMS casting process. To demonstrate size scalability, the PDMS stamps inked with EGaIn were gently pressed onto the paper-textured PDMS substrate, with the

stamping process being repeated 5 times to uniformly pattern the EGaIn electrodes, as shown in Figure 7.3 (b). Next, the EGaIn electrodes are functionalized wit O-CNTs using drop casting and LbL adsorption. Figure 7.3 (c) shows the fabricated O-CNT-integrated EGaIn electrodes, demonstrating large-area and uniform soft electrode patterning capability for energy storage devices.

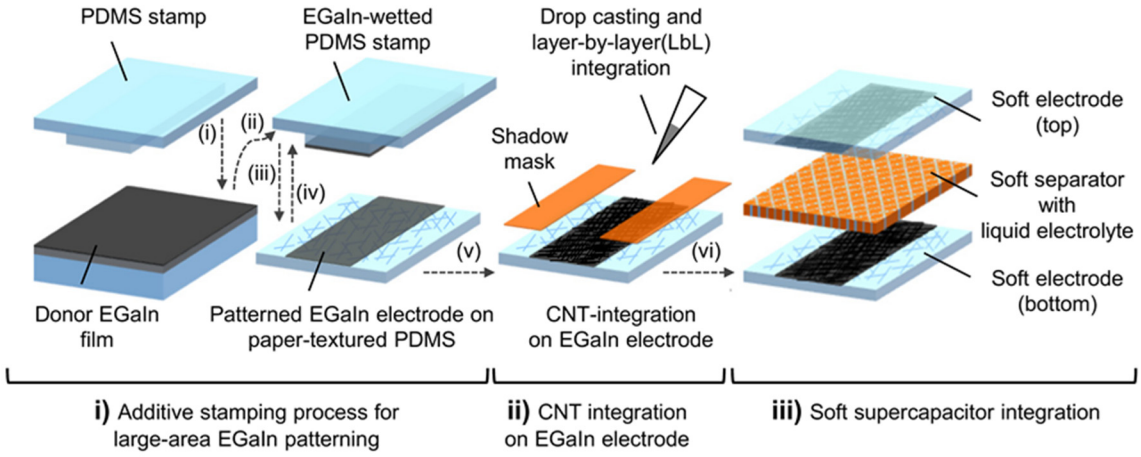

Figure 7.2 Fabrication process for the soft supercapacitors: i) additive stamping process based on soft lithography for large-area EGaIn patterning, ii) O-CNT functionalization via layer-by-layer adsorption process, and iii) soft supercapacitor integration to form parallel-plate configuration.

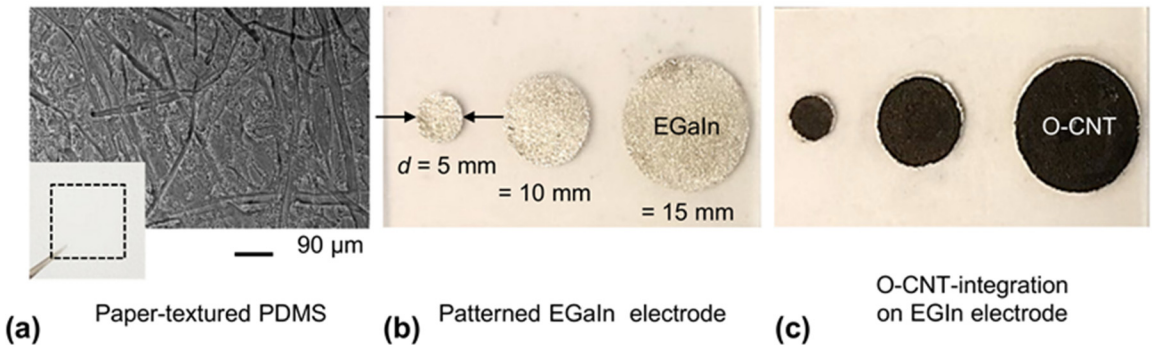

Figure 7.3 Soft O-CNT-functionalized EGaIn electrodes: (a) paper-textured PDMS substrate, (b) patterned EGaIn electrodes with diameters ranging from 5 mm to 15 mm on paper-textured substrate, and (c) O-CNT functionalization on the patterned EGaIn electrodes.

The oxygen functional groups on the CNT enhance the interaction with the native oxide (Ga_2O_3) on the surface of the EGaIn, resulting in a 3D nanostructure network on the

EGaIn surface with strong adhesion. Figure 7.4 demonstrates the mechanical stability of the O-CNT-integrated EGaIn electrodes. While cracks in the O-CNT film were generated upon applied strain, O-CNT films were not delaminated from the EGaIn electrodes while stretching up to 50% and blowing with a nitrogen gun for 5 minutes, as shown in Figure 7.4 (a) and (b). To further highlight the strong adhesion between the O-CNT and the EGaIn electrode, non-oxidized carbon nanoparticle inks dispersed in ethanol were prepared with the same concentration of ≈ 0.63 mg mL^{-1} and drop casted onto patterned EGaIn electrodes using the same fabrication conditions. Because of the hydrophilic nature of the mesoporous carbon nanoparticles, the drop-casted carbon nanoparticles aggregated and did not uniformly cover the EGaIn electrode. Furthermore, the nanoparticle islands easily delaminated from the EGaIn surface subject to flow from a nitrogen gun, as shown in Figure 7.4 (c).

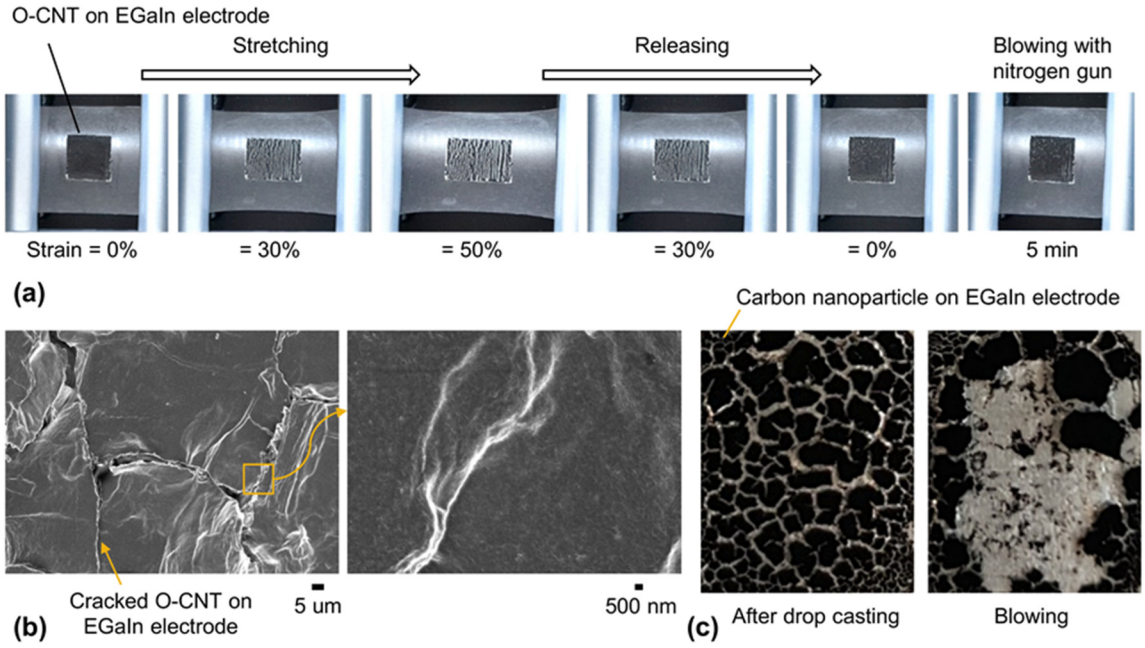

Figure 7.4 (a) Mechanical stability of O-CNT-functionalized EGaIn electrodes under stretching deformation up to 50% and subject to nitrogen flow from nitrogen gun for 5 minutes; (b) SEM images of cracked O-CNT film on EGaIn electrode; (c) Mechanical stability of carbon-nanoparticle-functionalized EGaIn electrodes.

7.3 All-Soft and Liquid-Phase Supercapacitors Based on O-CNT-Functionalized Liquid Metal Electrodes

7.3.1 Integration of All-Soft and Liquid-Phase Supercapacitors

In order to evaluate the energy storage performance of the fabricated O-CNT-functionalized EGaIn electrodes, soft supercapacitors with a parallel-plate configuration were integrated using a porous PDMS layer impregnated with liquid electrolyte as a separator (see schematic in Figure 7.1). The soft separator, comprising a porous and sponge-like PDMS structure, is used to physically separate the two soft electrodes to prevent a short circuit when the supercapacitor is mechanically deformed. Also, thanks to its hydrophilic properties, the soft separator can be filled with the injected ionic liquid providing conducting paths for ions to minimize equivalent series resistance (ESR). In this work, ionic liquid, $PYR_{14}TFSI$ (1-Butyl-1-methylpyrrolidinium bis (trifluoromethanesulfonyl)imide), was used as an electrolyte and injected into the PDMS separator to form all-soft and liquid-phase supercapacitor. Figures 7.5 (a)-(c) illustrate the fabricated soft components, namely the soft electrodes and soft separators, as well as the fully integrated soft supercapacitor. Figure 7.5 (a) shows photographs of fabricated O-CNT-functionalized EGaIn electrodes with an increasing number of LbL adsorption steps. The calculated areal density of the O-CNT films on top of the EGaIn electrodes increases from 0.25 mg cm^{-2} to 7.52 mg cm^{-2} as the number of LbL steps increases from 1 to 30, respectively.

To fabricate the soft separator, a sugar template was prepared using a molding process at 70 °C for 6 hours (Figure 8.5 (b)) [126]. To this end, sugar particles were added onto a circular-shaped PMMA mold (fabricated using a CO_2 laser cutter) to shape the sugar template for the soft separator. Then, liquid PDMS (10:1 ratio of PDMS pre-polymer and curing agent) was applied to the sugar template under vacuum for >2 hours and thermally

cured at 60 °C for 6 hours. After the curing process, the sugar was dissolved and washed away by soaking in water at 70 °C for 4 hours. The resulting porous and sponge-like PDMS structure has typical void sizes of approximately 400-500 μm. Figure 7.5 (b) shows the fabricated soft separators, which are 8 mm in diameter. To integrate them into microfluidic channels, the sugar template soaked with PDMS was cured inside of the pre-fabricated PDMS microfluidic channel at 60 °C for 6 hours. Thanks to its soft and stretchable characteristics, the fabricated soft separator can endure large mechanical deformation. Next, the soft components were vertically integrated and sealed using semi-dried liquid PDMS and thermally cured to obtain suitable crosslinking between the interfaces. Finally, ionic-liquid-based electrolyte ($PYR_{14}TFSI$) was injected into the PDMS channel, and the inlet and outlet holes were sealed using semi-dried liquid PDMS, as shown in Figure 7.5 (c).

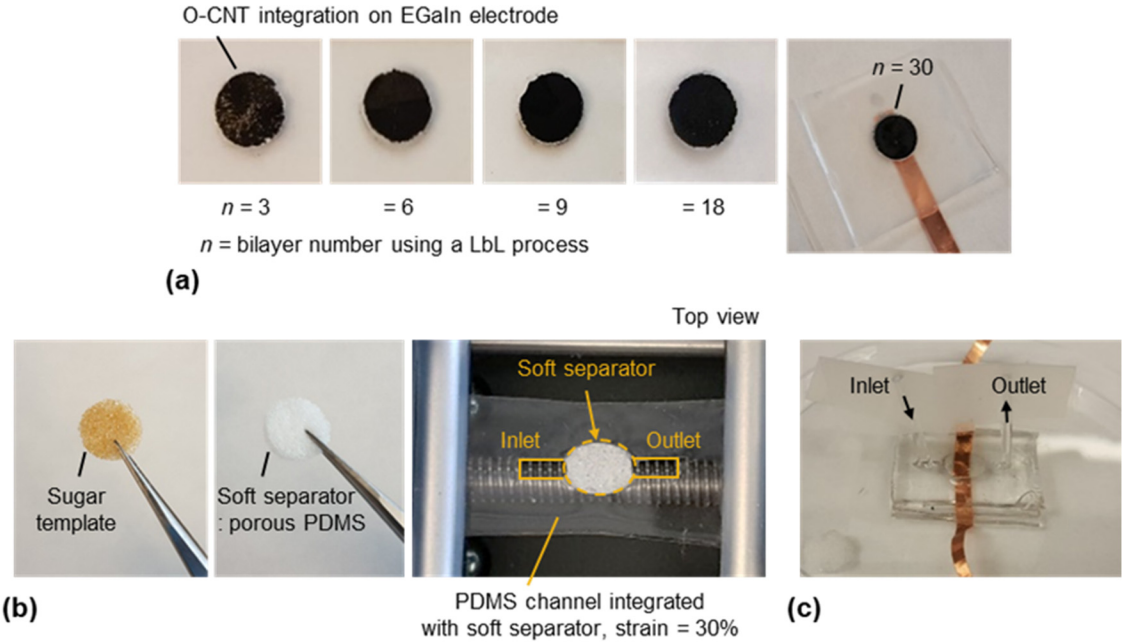

Figure 7.5 (a) Fabricated O-CNT-functionalized EGaIn electrodes with the number of LbL adsorption steps; (b) Fabricated soft separator, comprising a porous and sponge-like PDMS structure obtained using a sugar template, and fabricated PDMS channel integrated with a soft separator; (c) Assembled soft supercapacitor.

7.3.2 *Electrochemical Characterization*

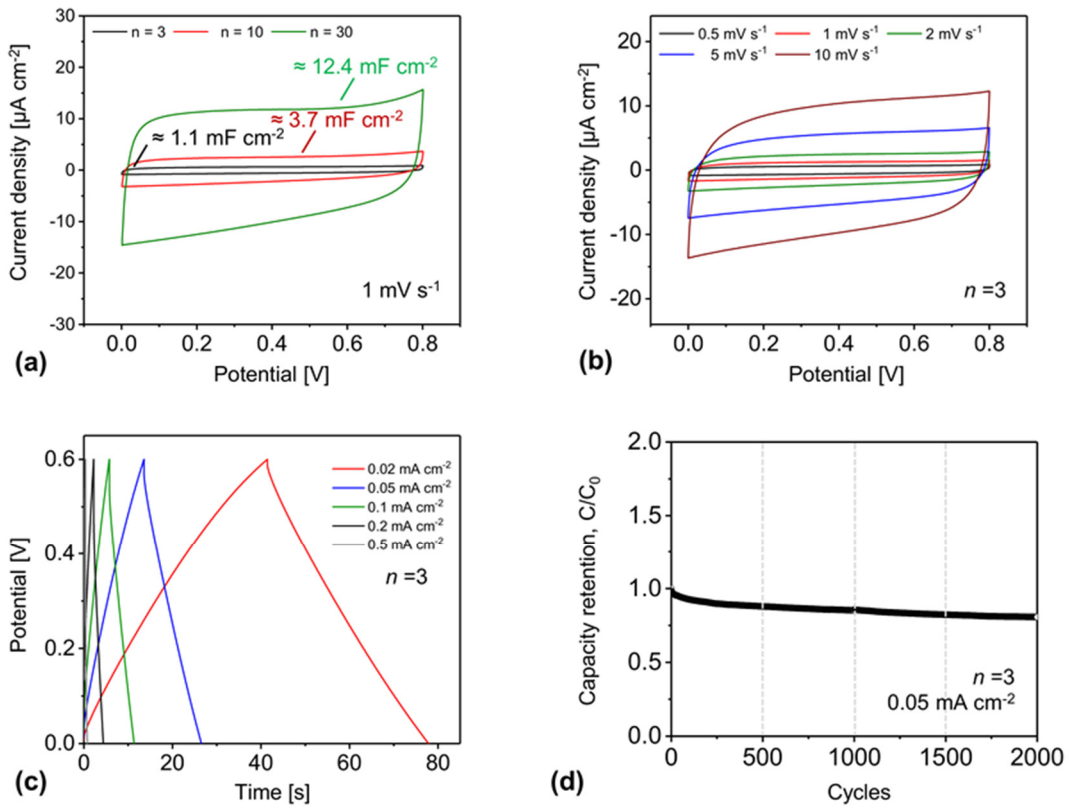

Figure 7.6 (a) Cyclic voltammograms for different bilayer numbers from 3 to 30 using a constant scan rate of 1mV s^{-1} and a constant potential window from 0 to 0.8 V; (b) Cyclic voltammograms for different scan rates from 0.5 to 10 mV s^{-1} for supercapacitor with O-CNT surface coated with n = 3 LbL steps, (c) galvanostatic charge/discharge curves for current densities ranging from 0.02 to 0.5 mA cm^{-2} for supercapacitor with O-CNT surface coated with n = 3 LbL steps, and (d) cycling retention, i.e. capacity retention C/C_0, as a function of charging and discharging cycles for supercapacitor with O-CNT surface coated with n = 3 steps.

The electrochemical properties of the fabricated soft supercapacitors were characterized using cyclic voltammetry (CV) and galvanostatic charge/discharge measurements. To this end, electrical contacts were made to the EGaIn electrodes using copper tape (see Figure 7.5 (c)). Figure 7.6 (a) displays the measured cyclic voltammograms recorded in the voltage window from 0 to 0.8 V at a scan rate of 1 mV s^{-1} as a function of the bilayer number and, thus, the density of the O-CNT layers. The

capacitance of a symmetric supercapacitor (C) and its specific capacitance (C_{sp}) can be calculated from the CV curves using Equation (12) and Equation (13), respectively [127]:

$$C = \frac{Q}{2V} = \frac{1}{2VS}\int_{V-}^{V+} i(V)\mathrm{d}V \tag{12}$$

$$C_{\mathrm{sp}} = 2\frac{C}{A} \tag{13}$$

Here, Q is the total charge obtained by integrating the positive and negative branches of the CV curves, $i(V)$ is the current, S is the scan rate, V is the potential window, and A is the area of one electrode, respectively.

To evaluate the fundamental electrochemical properties of the fabricated supercapacitors, the capacitance should be normalized considering the geometric area. The resulting measured areal capacitance in case of O-CNT functionalization with 3 LbL steps was ≈ 1.12 mF cm^{-2}. The specific capacitance increases almost linearly with the number of LbL adsorption steps with a measured areal capacitance ≈ 12.4 mF cm^{-2} with 30 LbL steps. Figure 7.6 (b) highlights the measured cyclic voltammograms for supercapacitors fabricated with 3 LbL steps at different scan rates from 0.5 mV s^{-1} to 10 mV s^{-1}. The rectangular shapes of the CV curves at varying scan rates illustrate the good electrochemical performance of the fabricated supercapacitors [127]. At low scan rates, the charge accumulation process is slow, thus resulting in higher capacitance values. Also, the current responds rapidly to voltage reversal, indicating the fast diffusion of ions in the electrodes. Figure 7.6 (c) shows the galvanostatic charge/discharge curves for supercapacitors with 3 LbL steps at different scan rate. The measured charge/discharge curves showed triangular features, indicating favorable capacitive behavior. Ultimately, the stability of a supercapacitor subject to multiple charging and discharging cycles is a critical parameter in evaluating its potential for practical applications. Figure 7.6 (d) shows

the capacitance retention, i.e. the ratio of the measured capacitance after multiple charging and discharging cycles to the initial capacitance at a scan rate of 0.05 mV s^{-1}. The measured capacitance drops by less than 10% as the number of cycles increases to >2,000 cycles, demonstrating excellent electrochemical stability of the soft supercapacitors.

7.3.3 Mechanical Characterization

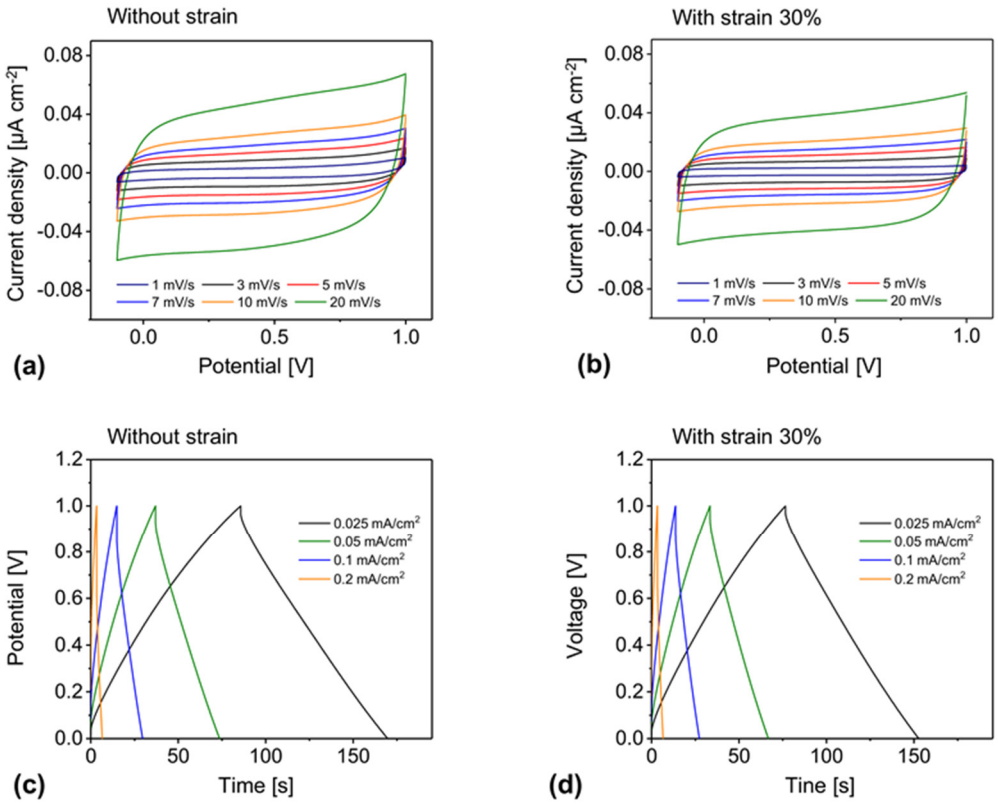

Figure 7.7 Cyclic voltammograms for different scan rates from 1 to 20 mV s^{-1} for supercapacitors with O-CNT surface coated with n = 9 LbL steps (a) without strain and (b) with applied strain of 30%; Galvanostatic charge/discharge curves for current densities ranging from 0.025 to 0.2 mA cm^{-2} for supercapacitors with O-CNT surface coated with n = 9 LbL steps (c) without strain and (d) with applied strain of 30%.

One of the main requirements for soft energy storage devices is to maintain their electrochemical properties during deformation. To evaluate their mechanical effects, soft supercapacitor fabricated with 9 LbL steps were subjected to strain up to 30%, and their electrochemical properties were measured. Figures 7.7 (a) and (b) compare the measured

cyclic voltammograms obtained at different scan rates from 1 mV s^{-1} to 20 mV s^{-1} without and with applied strain of 30%, respectively. The measured CV curves under mechanical deformation retain their rectangular shapes and maintain almost unchanged compared to the CV measurements without stain, indicating the remarkable stability of the soft supercapacitors under mechanical deformation. Moreover, galvanostatic charge/discharge curves measured under applied strain of 30% showed almost the same performances compared to the charge/discharge curves without applied strain, as shown in Figure 7.7 (c) and (d). Figure 7.8 compares the extracted areal capacitance as a function of the current density for the strained and unstrained supercapacitor, demonstrating the performance stability with an average 6.5% of capacitance reduction under applied strain. Finally, the capacitance retention of soft supercapacitors without and with applied strain of 30% is demonstrated in Figure 7.9. The devices show excellent cycling stability, retaining 95% of their initial capacitance after 2,000 cycles in stretching conditions. As a result, the proposed EGaIn-based soft supercapacitors showed excellent electrochemical and mechanical performance without significant reduction in their electrochemical properties under applied strain. Table 7.1 summarizes and compares the performance of the supercapacitors developed here to other types of stretchable electrodes and their supercapacitor performance under similar measurement conditions.

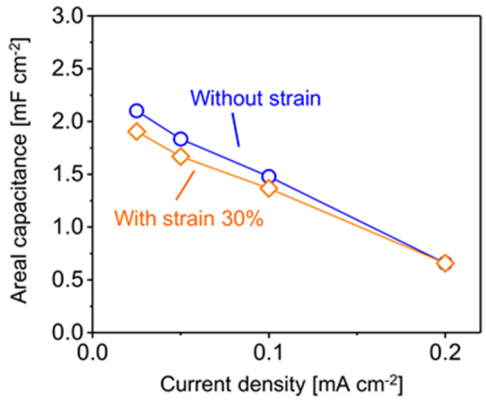

Figure 7.8 Areal capacitance as a function of the current density for supercapacitors with 9 LbL steps with/without applied strain of 30%.

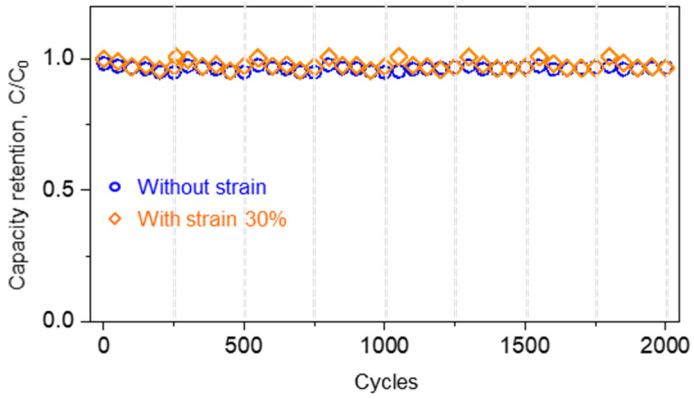

Figure 7.9 Cycling retention for supercapacitors with 9 LbL steps with/without applied strain of 30% every 250 cycles for up to 2000 charging and discharging cycles. After each 250 cycle, slight capacitance recovery was observed because of a redistribution of electrical charges.

Table 7.1. Comparison of stretchable supercapacitors in the literature.

Stretchable electrode	Fabrication method	Capacitance	Strain	Cycling with strain
soft electrode (Ch. 7): O-CNT/EGaIn/PDMS	Soft lithography & LbL deposition	12.4 mF cm^{-2} at 1 mV s^{-1}	30%	2,000 cycles
Carbon electrode [128]: CNT/PDMS	Transfer deposition	0.6 mF cm^{-2} at 100mV s^{-1}	100%	200 cycles
Carbon electrode [127]: Graphene/PDMS	Laser ablation	650 µF cm^{-2} at 50 mV s^{-1}	50%	1,000 cycles
Solid electrode [74]: SWNT/Au/PDMS	Photolithography & LbL deposition	100 µF at 500 mV s^{-1}	30%	-

7.4 Conclusion

This chapter introduces all-soft and liquid-phase supercapacitors based on O-CNT-functionalized EGaIn electrodes. The EGaIn patterns serve as the electron transport channel and support for CNT adsorption. The oxygen functional groups on the CNT enhance the energy density of the electrodes as well as their interaction with the native

oxide (Ga_2O_3) on the surface of the EGaIn, resulting in a 3D network of nanostructures on the EGaIn surface with strong adhesion even at 50% applied strain. To demonstrate supercapacitors with a parallel-plate configuration, O-CNT-functionalized EGaIn electrodes were vertically integrated with a soft separator, comprising a porous PDMS structure filled with ionic liquid. The ionic-liquid-filled soft separator enables physical separation between the two electrodes for all-soft and liquid-phase supercapacitors. Our preliminary data show that the areal capacitance increases almost linearly with the number of LbL adsorption steps with a measured areal capacitance ≈12.4 mF cm^{-2} with 30 LbL steps. Moreover, the specific capacitances remain nearly unchanged under mechanical deformation, which indicates excellent electrochemical and mechanical stability. The demonstrated all-soft and liquid-phase supercapacitors overcome the limitation of rigid supercapacitor configuration.

Future work includes improving areal capacitance and voltage window for high-performance, soft supercapacitors for fully-integrated soft microsystems. High areal capacitance (> 100 mF cm^{-2}) can be achieved by adding pseudocapacitive nanomaterials [129-131]. Also, the wide-range voltage operation (> 3 volts) can be improved by utilizing serial/parallel capacitor interconnection [132, 133].

7.5 Acknowledgement

This work was done in collaboration with Georgia Tech's Energy Storage and Conversion Lab in The George W. Woodruff School of Mechanical Engineering. Prof. Seung Woo Lee and Dr. Byeongyong Lee assisted with the design, fabrication, and characterization of the soft supercapacitors, in particular the material characterization and electrochemical performance evaluation of the fabricated soft supercapacitors, as well as technical discussion.

CHAPTER 8. CONCLUSIONS AND FUTURE WORK

8.1 Contributions to Liquid-Metal-Based Soft Electronic Devices and Integrated Microsystems

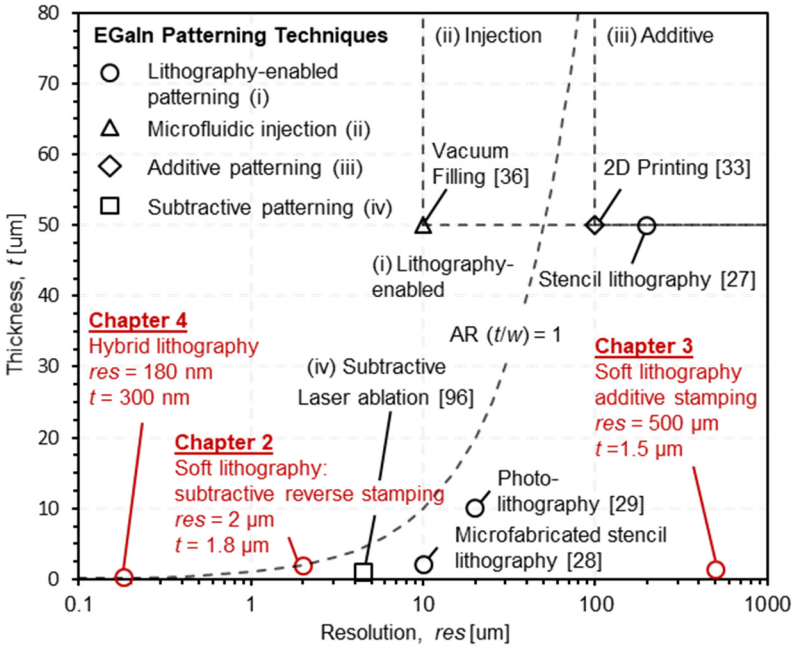

Figure 8.1 Comparison of liquid metal patterning technologies demonstrated in this work, namely soft lithography using subtractive reverse stamping (Chapter 2) and additive stamping (Chapter 3) and hybrid lithography (Chapter 4), with technologies demonstrated in the literature in terms of film thickness (y-axis) and lateral resolution (x-axis).

This thesis work reported high-resolution and multiscale liquid metal (EGaIn) patterning and vertical integration techniques and their application to soft passive circuit elements, soft physical and chemical sensors, and soft energy storage devices. Figure 8.1 compares the obtainable lateral resolution and film thickness of EGaIn patterning methods reported in the literature with those of the EGaIn patterning techniques investigated in this work based on soft lithography (subtractive reverse stamping in Chapter 2 and additive stamping in Chapter 3) and hybrid lithography (Chapter 4). The performance of each of

the three developed technologies will be compared to the state of the art in more detail in the following sections, highlighting key research contributions (Sections 8.1.1-8.1.3).

Combining the scalable fabrication and vertical integration techniques, 3D-integrated, soft functional microsystems were demonstrated for physical sensing (Chapter 5) and chemical sensing (Chapter 6) applications. In addition, high-performance, soft supercapacitors were demonstrated (Chapter 7) to ultimately realize fully-integrated soft microsystems. Again, key research contributions are summarized below (Sections 8.1.4 and 8.1.5).

8.1.1 Microscale EGaIn Patterning using Subtractive Reverse Stamping Based on Soft Lithography

In Chapter 2, microscale EGaIn thin-film patterning using a subtractive reverse stamping technique based on soft lithography was developed to create size-scalable and high-density soft passive components and circuits. Because of the high surface tension and unique wetting properties of EGaIn, creating microscale and scalable EGaIn patterns has been a challenge: prior to this work, only microtransfer molding [37] has been used to pattern 1 μm thick EGaIn films with a 2 μm resolution (see also Table 1.2), but the method suffered from liquid-metal residues. The subtractive reverse stamping process developed here uses a chemical surface modification to remove residues in a residue transfer processes and demonstrates, for the first time, high-resolution (>=2 μm), size-scalable (μm to 1-2 mm), uniform, and residue-free EGaIn thin-film patterning at room temperature and under ambient pressure. The smallest patterned feature size was 2 μm with a film thickness of <1.8 μm, being on par with the best EGaIn resolution demonstrated before while also providing a residue free patterning (see Figure 8.1 and Table 1.2).

However, for channel widths >2 mm, EGaIn is not effectively transferred to the inside of the PDMS channels using the subtractive reverse stamping process because of the sagging deformation of wide channels during the pressure-based molding process. Therefore, the reverse stamping technique can be applied for the fabrication of microscale soft electronic devices and sensing platform for physical, chemical, and biological applications with dimensions ranging from 2 μm to 2 mm.

8.1.2 Centimeter-Scale EGaIn Patterning using Additive Stamping Technique Based on Soft Lithography

In Chapter 3, uniform, large-area EGaIn thin-film patterning was demonstrated using an additive stamping technique based on soft lithography. Stamp lithography for EGaIn has often been regarded as the lowest resolution and least reliable technique among the additive printing methods [32, 83]. Generally, the limited wettability of EGaIn caused by the surface oxide yields non-uniform films over large areas. However, the present work demonstrates that proper physical surface modification of PDMS substrate, such as the use of paper-textured surfaces, increases the surface area and adhesion forces, and ultimately enhances the wettability to enable printing of uniform and smooth EGaIn thin films. Thereby, the PDMS stamp wet with EGaIn is stamped onto paper-textured PDMS. The patterned smallest feature size was 500 μm with film thickness of ≈ 1.5 μm. Although this additive stamping technique showed relatively poor resolution, it is suitable for uniform, large-area EGaIn thin-film patterning, needed for the fabrication of soft printed circuit boards (sPCB) and soft energy storage devices. To highlight the patterning capabilities ranging from μm to cm by combining the additive and subtractive stamping techniques, two functional soft microsystems were demonstrated: a fingertip-mountable, soft

biological microsystem and soft heaters with localized and distributed heating capability. Finally, this additive stamping technique for EGaIn patterning is used for soft energy storage devices, described in Chapter 7.

8.1.3 Nanofabrication for Submicron-Scale Soft Electronic Devices

Chapter 4 introduced a novel hybrid fabrication technique using electron-beam lithography for micro/nanostructure fabrication and soft lithography for EGaIn stamping to create, for the first time, submicrometer-scale EGaIn patterns. Scaling the reverse subtractive stamping technique described in Chapter 2 to sub-micrometer patterns is difficult because of the high surface tension of EGaIn and the deformation of PDMS micro/nanochannels during the molding process. To overcome this limitation, a hybrid approach based on nanolithography and soft lithography was applied using a biphasic structure, comprising a gold adhesion layer coated with EGaIn. It was found that stamped EGaIn is uniformly spread on the Au thin film and fills concave nano/micropatterns with EGaIn up to the designed PMMA thickness. For the first time, submicron-scale EGaIn thin film patterning with feature sizes as small as 180 nm was achieved, resulting in the highest resolution EGaIn patterning technique to date (see Figure 8.1 and comparison in Table 1.2).

The developed hybrid EGaIn patterning technique shows very competitive performance in terms of resolution, wiring density, as well as strain limit, if compared to other types of stretchable conductors, namely serpentine solid metals and nanomaterial composites, as summarized in Table 8.1. Serpentine solid metal patterns on a soft elastomer exhibit excellent electrical conductivity and can endure large mechanical strain. However, the necessary serpentine wires increase space requirements and, thus, lower the achievable wiring density compared to EGaIn wires at the same lateral resolution. On the other hand,

printing conductive nanomaterials enables simple and inexpensive fabrication of conductors without the need for serpentine geometry. However, the limited resolution combined with the low material conductivity are major drawbacks. In this respect, the use of intrinsically soft liquid metal patterned by the developed hybrid lithography technique offers a currently unrivaled combination of resolution, electrical conductivity, and resulting electronic/wiring density. The demonstrated submicron-scale and high-density soft passive electronic devices and sensor arrays based on EGaIn fabricated using the hybrid lithography process are currently difficult if not impossible to build with other fabrication methods. Moreover, thanks to EGaIn's fluidic properties, very large stretchability ≈ 700% has been demonstrated with Ecoflex or SEBS (Poly[styrene-*b*-(ethylene-*co*-butylene)-*b*-styrene]) encapsulation. It should be noted that the maximum achievable strain is determined by the encasing material. Considering the demonstrated high-resolution and high-density EGaIn patterning capabilities, the proposed fabrication technique opens a path for all-soft and integrated biological sensing platforms for single-cell mechanobiology.

Table 8.1. Comparison of fabrication approaches for stretchable conductors (adapted from [11]).

	Serpentine solid metal	Nanomaterial composite	Liquid metal (EGaIn)
Material and fabrication	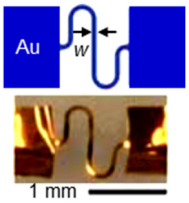 Serpentine Au [134]	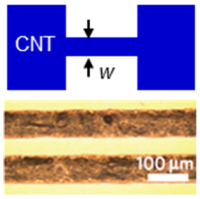 CNT network [17]	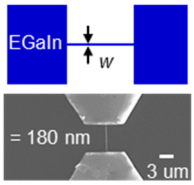 EGaIn (this work)
Minimum feature size	w = 10 µm transfer printing [135]	$w \approx$ 100 µm spray printing [18]	w =180 nm hybrid lithography
Electrical conductivity	Au: 4×10^7 S m^{-1}	Varying with strain 6 S m^{-1} @ 134% applied strain [76]	EGaIn: 3.4×10^6 S m^{-1}
Strain limit	20% wavy w/ PDMS [20] 300% serpentine w/ Ecoflex [136]	134% w/ PDMS [76]	Determined by the encasing materials ≈ 200% w/ PDMS [137] ≈ 700% w/ Ecoflex [46] ≈ 700% w/ SEBS [138]
Limitation	Low electronic density	Limited resolution Low conductivity	Encapsulation

8.1.4 All-soft Physical and Chemical Microsystems

Combining the scalable fabrication and integration techniques, 3D-integrated, soft functional microsystems were demonstrated for physical and chemical sensing applications. In Chapter 5, all-soft and 3D-integrated physical microsystems, composed of a soft sensor, a soft interconnector, and a soft readout circuit, are demonstrated by utilizing the subtractive reverse stamping process and the 3D integration technique. Prior to this

work, single sensing elements have been demonstrated using EGaIn-filled microchannels to detect strain [46, 47] or pressure [35]. With EGaIn being a liquid, the observed resistance change versus applied strain originates from geometrical effects, resulting in relatively low sensitivity ($GF \approx 2$). Building on the subtractive reverse stamping EGaIn patterning technique and the 3D integration approach developed in this work, the demonstrated soft physical sensing microsystems improve over a single sensor [46, 47] by enabling high-density integration as well as multifunctional sensing capabilities. Two types of all-soft physical microsystems were highlighted in this chapter: a finger-mountable strain sensing microsystem with suppressed mechanical cross-talk and compensation for temperature effects and a fingertip microsystem for simultaneous proximity, touch, and pressure measurements.

Moreover, an all-soft capacitive chemical sensing platform and a 3D-integrated *LC* sensor were demonstrated in Chapter 6 for liquid-phase and gas-phase VOC detection. In previous work, EGaIn-based droplet electrodes [53-55] and injected bulk electrodes [52, 56] have been demonstrated for chemical sensing applications. Because of technical challenges associated with fine, uniform, and residue-free EGaIn patterning, all-soft and highly integrated chemical sensing microsystems have not yet been investigated and the present work demonstrates, for the first time, all-soft and integrated chemical sensing platforms based on EGaIn. In the case of liquid-phase chemical sensing, the wireless VOC sensing performance and microfluidic capacitance tuning capability were investigated for different dielectric liquids. In the case of gas-phase chemical sensing, the sensing performance of the soft sensor was evaluated using different alcohols as analytes and compared to that of a silicon-based, solid-state gas sensor using a PDMS sensing film. Compared to the silicon-based gas sensor (see also Table 6.1), the soft sensor shows higher sensitivities than the solid-state sensor, which can be explained by the thick PDMS used both as a substrate and sensing film. This thick PDMS film, however, results in slow response and recovery time constants for the soft sensor compared to the silicon-based

sensor. Therefore, optimized sensing film geometries should be investigated in the future to reduce response times while maintaining the sensor sensitivity. Nevertheless, the all-soft sensor provides flexibility and stretchability, allowing for wearable electronics applications.

8.1.5 All-soft Energy Storage Components

All-soft and liquid-phase supercapacitors based on O-CNT-functionalized EGaIn electrodes were investigated in Chapter 7. To design high-performance and stretchable electrodes for soft supercapacitors, carbon nanomaterials should be uniformly integrated on the current collectors without delamination when mechanically deformed. However, combining EGaIn with nanocarbon materials is not straightforward due to the phase separation between the hydrophobic CNT surface and the oxophilic EGaIn surface. In this study, it is demonstrated that oxygen functional groups on the surface of CNTs provide a strong interaction with the native oxide layer (Ga_2O_3) on the surface of EGaIn electrodes. As a result, integrated O-CNT films did not delaminate from the EGaIn electrodes while stretching up to 50% and blowing with a nitrogen gun for 5 minutes. To demonstrate soft supercapacitors with a parallel-plate configuration, functionalized soft EGaIn electrodes were vertically integrated with a soft separator, comprising a porous and sponge-like PDMS structure filled with liquid electrolyte. To our best knowledge, it is the first demonstration of an all-soft platform based on EGaIn for high-performance and wearable energy storage devices. The fabricated EGaIn-based supercapacitor showed an areal capacitance of 12.4 F cm^{-2} at 1 mV s^{-1}, demonstrating higher areal capacitance values compared to other types of stretchable supercapacitors [74, 127, 128], as summarized in Table 7.1. Furthermore, high electrochemical performance can be achieved by utilizing the strong interaction between the functionalized carbon/pseudocapacitive nanomaterials and the EGaIn electrodes, which cannot be done using other types of stretchable electrodes because of the delamination challenge. The electrochemical performance of the fabricated

soft supercapacitors was evaluated with/without applied strain of 30% to highlight the mechanical stability up to 2,000 cycles.

8.2 Future Work

This work has demonstrated novel fabrication techniques to pattern EGaIn films with dimensions from the nanometer scale to the centimeter scale and applied these patterning techniques to fabricate soft electronic components and circuits, soft sensors, and soft energy storage components. To demonstrate the full potential of the developed EGaIn fabrication techniques, future research activities should target a low-cost fabrication technique for EGaIn structures that can be applied to large substrate sizes as well as the system-level integration of circuits, sensors, and energy storage components to realize all-soft and fully-integrated microsystems.

Low-cost EGaIn patterning process: The demonstrated high-resolution EGaIn patterns and resulting high-density soft electronic devices heavily rely on conventional lithography-enabled processes, requiring expensive cleanroom facilities and limiting substrate sizes. Therefore, lowering the fabrication cost has practical significance. Roll-to-roll and printing processes are possible solutions for low cost, high throughput, and mass manufacturing. However, these processes are currently limited by the achievable resolution or uniformity. Therefore, an optimized printing process using EGaIn-dispersed inks could be investigated for reliable EGaIn patterning over large substrate areas.

System integration toward all-soft and fully-integrated microsystems: The knowledge acquired in this work can be applied to develop and demonstrate all-soft, integrated microsystems, which interface with the soft tissues of the human body for electrophysiological sensing. The soft functional components will be fabricated either all-soft or in a hybrid electronic format based on EGaIn and PDMS and vertically integrated

to form 3D structures using soft vias. An all-soft sensor will measure a physiological signal, such as electrocardiography (ECG) or electromyography (EMG), via skin-interfaced ionic-liquid based electrodes. Measured electrophysiological data pass through commercial analog amplifiers and filters prior to wireless transmission using a Bluetooth system on a chip. An all-soft wireless power transfer unit will charge an all-soft supercapacitor, and then supply regulated power to the entire system.

APPENDIX A. FABRICATION PROCESSES

In the following, a detailed description is provided for the EGaIn patterning processes with material information. The fabrication processes were conducted in iSenSys Lab and cleanroom facilities of the Institute for Electronics and Nanotechnology (IEN) at the Georgia Institute of Technology.

A.1. Subtractive Reverse Stamping Process Based on Soft Lithography

PDMS microchannel preparation and chemical surface modification process

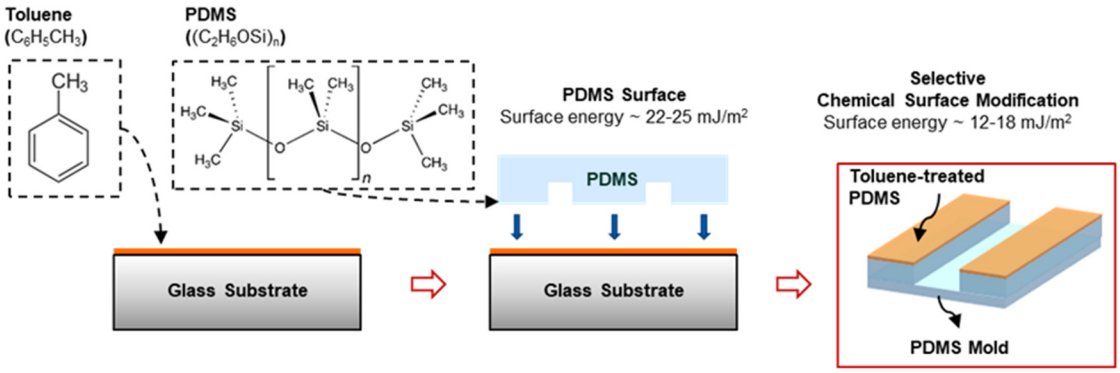

Figure A1.1 Selective chemical surface modification using drop-casted toluene for selective wetting.

PDMS (Sylgard 184, Dow Corning) was prepared with a 10:1 ratio of PDMS pre-polymer and curing agent, and PDMS molds were fabricated using a normal replica molding process. To avoid the formation of unwanted EGaIn residue, the surfaces of the PDMS molds were selectively chemically modified. To this end, a 500 µl droplet of toluene (Toluene, ACS, VWR International) was drop-coated on a glass substrate and subsequently dried at room temperature and under atmospheric pressure for 5-10 minutes to minimize swelling of the PDMS mold. Then, the PDMS mold was placed on the glass substrate for

chemical surface modification. After approximately 5-10 minutes, the PDMS mold and glass slide were separated. To characterize the hydrophobicity of the treated PDMS surfaces, the surface energies of modified and non-modified surfaces were measured using a contact angle measurement system (Ramé-hart Model 250 goniometer).

Microtransfer molding and residue transfer process

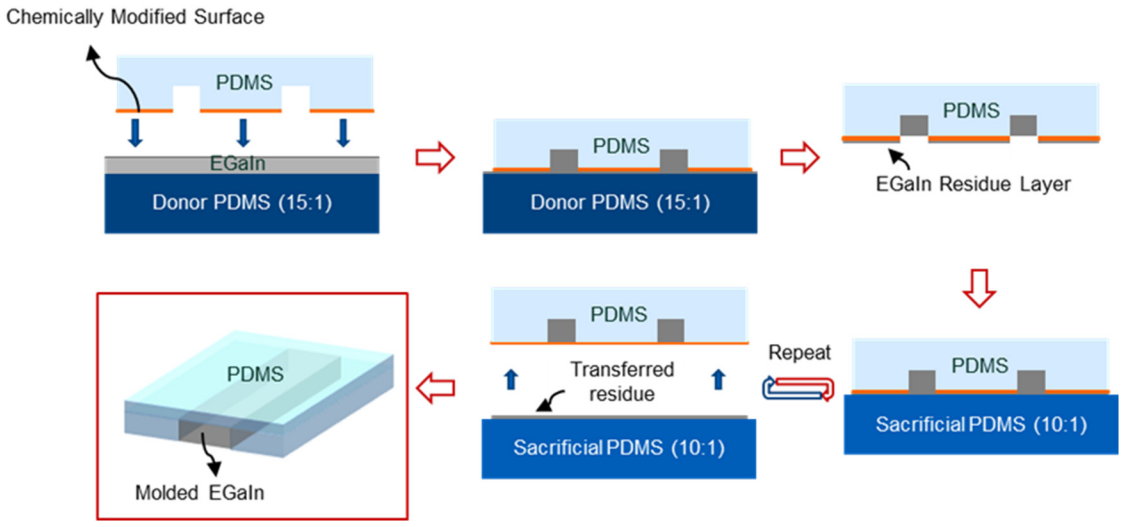

Figure A.1.2 Liquid metal residue transfer process: unwanted liquid metal residue on the outside of the channel can be transferred to a sacrificial PDMS substrate, and by repeating this process several times all unwanted liquid metal residue is removed.

In the microtransfer molding process, EGaIn (Gallium-Indium eutectic, >%99.99 trace metal basis, Sigma-Aldrich) was dispensed on a donor PDMS substrate (15:1 mass ratio to improve wettability). using a syringe, and spread and flattened using a PDMS roller (10:1 mass ratio). Next, the PDMS mold was gently pressed onto the EGaIn thin film and separated from it. Unwanted liquid metal residue on the outside of the channel areas was transferred to a sacrificial PDMS layer (10:1 mass ratio). This transfer process was repeated several times (≈ 15 times) until all residue was removed. The EGaIn-filled PDMS mold

was finally bonded to an additional PDMS layer, with embedded liquid-metal-filled through-PDMS vias, by oxygen-plasma treatment. Commercial copper tape was used for electrical contacts. All PDMS samples were polymerized at 60 °C for 8 hours.

A.2 Additive Stamping Process Based on Soft Lithography

PDMS stamp preparation: An acrylic master with critical dimension of 500 μm was fabricated using a CO_2 laser cutter (Hermes LS500XL), and liquid PDMS (10:1 ratio of PDMS pre-polymer and curing agent, Sylgard 184, Dow Corning) was drop-casted on the fabricated molds and cured at 60 °C for 8 hours.

Paper-textured PDMS preparation: A small piece of standard printing paper (Office Depot #348-037) was taped on a flat substrate, and liquid PDMS (10:1 ratio of PDMS pre-polymer and curing agent, Sylgard 184, Dow Corning) was either drop-casted or spin-coated on the paper substrate. After curing at 60 °C for 8 hours, the polymerized PDMS was gently peeled off from the paper substrate. With this process, the micro cellulose fiber structures on the paper can be effectively transferred to the PDMS surface.

Additive stamping process: EGaIn (gallium-indium eutectic, >99.99% trace metal basis, Sigma-Aldrich) was dispensed and spread using a PDMS roller on a donor PDMS substrate. The PDMS stamp was gently pressed onto the EGaIn film, and then the EGaIn film was stamped to the paper-textured PDMS substrate. The patterned EGaIn films on the paper-textured PDMS were then sealed by an additional PDMS layer using either drop casting or spin coating, and commercial copper tape was used for electrical contacts. All PDMS samples were polymerized at 60 °C for 8 hours.

A.3 Hybrid Lithography Based on EBL and Soft Lithography

Nano/microstructure fabrication process: A water-soluble sacrificial layer (poly(acrylic acid), PAA, Polyscience, Inc.) was spun on a Si wafer at 2000 rpm for 30 s and baked at 100 ºC for 60 s, resulting in ≈ 6 μm thickness. Over the PAA sacrificial layer, a parylene-C film with 600 nm thickness was deposited by chemical vapor deposition (CVD, SCS Labcoter PDS 2010) process. For nano/microstructure fabrication, electron-beam lithography (EBL, Elionix ELS G-100) was mainly utilized to pattern spin-coated poly(methylmethacrylate) (PMMA) films with thicknesses ranging from 300 nm to 1 μm. Finally, a thin Ti/Au layer was deposited on the patterned nano/microstructures using an electron-beam evaporator (Denton Explorer) with a target thicknesses of 5nm/30nm.

EGaIn Stamping Process: For PDMS stamp fabrication, a rectangular acrylic master (size: 1 cm × 1 cm) was fabricated using a CO_2 laser cutter (Hermes LS500XL), and liquid PDMS (10:1 ratio of PDMS pre-polymer and curing agent, Sylgard 184, Dow Corning) was drop-casted on the fabricated molds and cured at 60 °C for 8 hours. In the next step, the fabricated PDMS stamp were wet with EGaIn and gently pressed 2-3 times onto the Au-deposited nano/microstructures to transfer the EGaIn thin film. The stamped EGaIn on Au were finally patterned using a PMMA lift-off process with acetone.

Soft material encapsulation and release process: The patterned EGaIn structures were encapsulated with liquid PDMS (10:1 ratio of PDMS pre-polymer and curing agent, Sylgard 184, Dow Corning) either by spin coating or drop casting. The fabricated soft electronic devices were then released by submerging the samples into water for >6 hours. The fabricated soft devices were naturally floating on the water surface and gently placed on a glass substrate to etch the parylene-C layer. The parylene-C layer was etched using

oxygen plasma in a reactive-ion etching system (RIE, Vision 320 RIE) for >7 minutes or until the parylene-C film was completely removed. Under the etching conditions of 200 mTorr pressure and 200 W power, the tested parylene-C etch rate using oxygen plasma was ≈ 100 nm min^{-1}. After etching the palylene-C layer, the soft electronic devices were encapsulated again with PDMS for backside sealing.

APPENDIX B. DIMENSIONS OF SOFT DEVICES

B.1 Dimensions of the Finger-Mountable Strain Sensing Microsystems

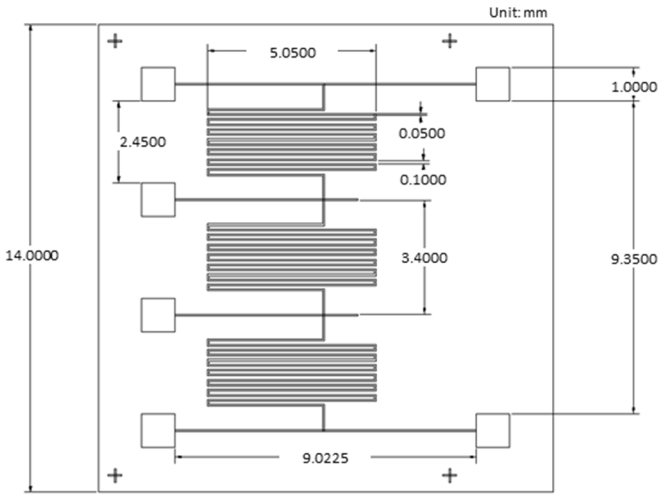

Figure B.1.1 Dimensions of the soft readout Wheatstone bridge circuit. The numbers shown are in millimeters.

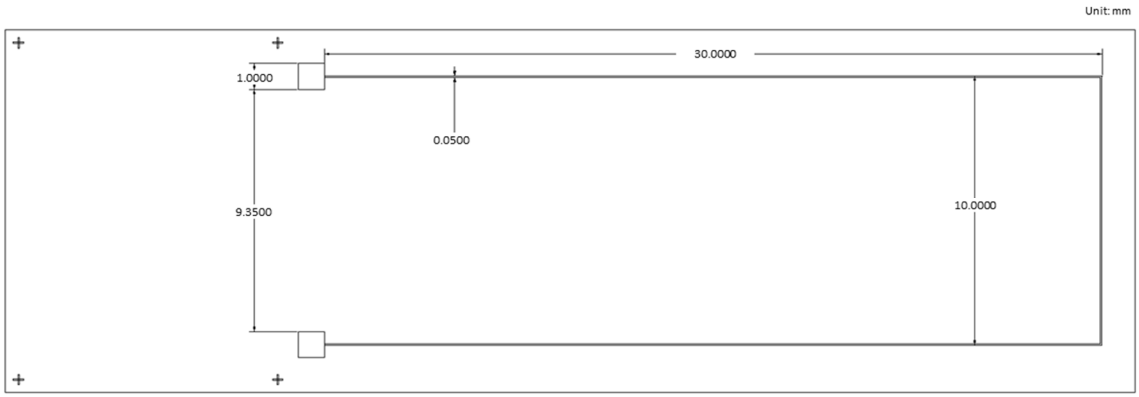

Figure B.1.2 Dimensions of the soft strain sensor. The numbers shown are in millimeters.

B.2 Dimensions of the Fingertip Microsystem

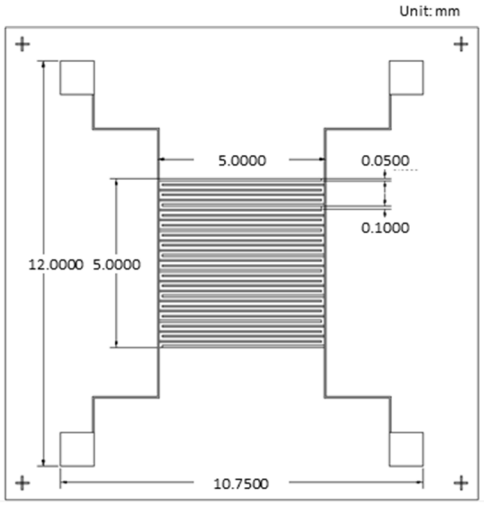

Figure B.2.1 Dimensions of the soft capacitive sensor. The numbers shown are in millimeters.

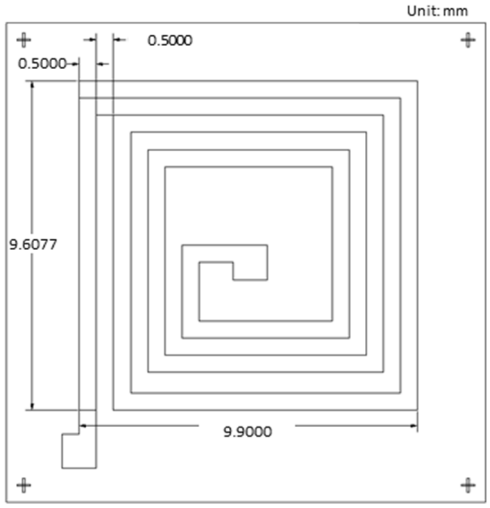

Figure B.2.2 Dimensions of the soft resistive sensor. The numbers shown are in millimeters.

B.3 Dimensions of the Chemical Microsystem

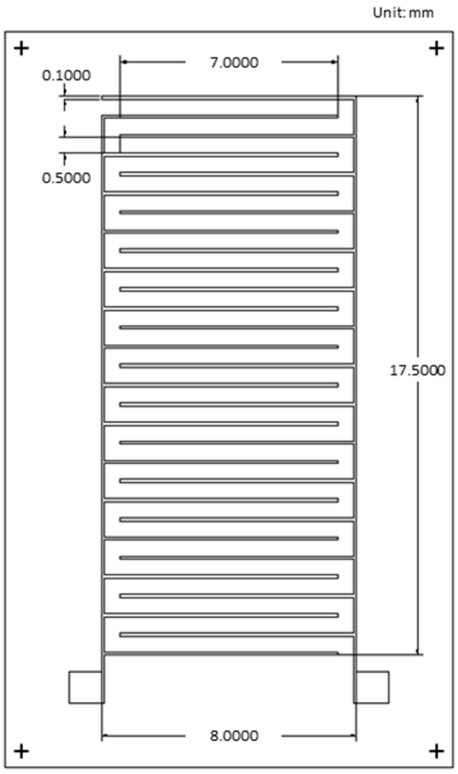

Figure B.3.1 Dimensions of the soft interdigitated capacitor. The numbers shown are in millimeters.

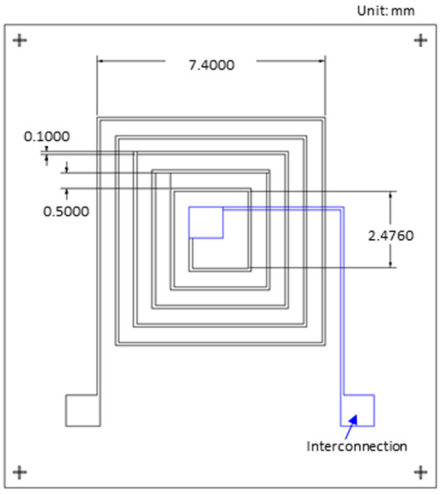

Figure B.3.2 Dimensions of the soft planar spiral inductor. The numbers shown are in millimeters.

REFERENCES

[1] A. Chortos, J. Liu, Z. Bao, "Pursuing prosthetic electronic skin", *Nat. Mater.* 15, 937 (2016).

[2] A. Chortos, Z. Bao, "Skin-inspired electronic devices", *Mater. Today* 17, 321 (2014).

[3] Y. Liu, M. Pharr, G. A. Salvatore, "Lab-on-skin: a review of flexible and stretchable electronics for wearable health monitoring", *ACS Nano* 11, 9614 (2017).

[4] J. Wang, M.-F. Lin, S. Park, P. S. Lee, "Deformable conductors for human–machine interface", *Mater. Today* 21, 508 (2018).

[5] D. Barrettino, "Look into my eyes", *IEEE Spectrum* 54, 38 (2017).

[6] W. Gao, S. Emaminejad, H. Y. Y. Nyein, S. Challa, K. Chen, A. Peck, H. M. Fahad, H. Ota, H. Shiraki, D. Kiriya, D. H. Lien, G. A. Brooks, R. W. Davis, A. Javey, "Fully integrated wearable sensor arrays for multiplexed in situ perspiration analysis", *Nature* 529, 509 (2016).

[7] T. Q. Trung, N. E. Lee, "Recent progress on stretchable electronic devices with intrinsically stretchable components", *Adv. Mater.* 29, 1603167 (2017).

[8] S. Wagner, S. Bauer, "Materials for stretchable electronics", *MRS Bull.* 37, 207 (2012).

[9] Z. Suo, "Mechanics of stretchable electronics and soft machines", *MRS Bull.* 37, 218 (2012).

[10] J. A. Rogers, T. Someya, Y. Huang, "Materials and mechanics for stretchable electronics", *Science* 327, 1603 (2010).

[11] M. D. Dickey, "Stretchable and soft electronics using liquid metals", *Adv. Mater.* 29, 1606425 (2017).

[12] N. Kazem, T. Hellebrekers, C. Majidi, "Soft multifunctional composites and emulsions with liquid metals", *Adv. Mater.* 29, 1605985 (2017).

[13] M. D. Dickey, R. C. Chiechi, R. J. Larsen, E. A. Weiss, D. A. Weitz, G. M. Whitesides, "Eutectic gallium-indium (EGaIn): a liquid metal alloy for the formation of stable structures in microchannels at room temperature", *Adv. Funct. Mater.* 18, 1097 (2008).

[14] R. C. Chiechi, E. A. Weiss, M. D. Dickey, G. M. Whitesides, "Eutectic gallium-indium (EGaIn): a moldable liquid metal for electrical characterization of self-assembled monolayers", *Angew. Chem. Int. Ed. Engl.* 47, 142 (2008).

[15] S. Xu, Y. Zhang, L. Jia, K. E. Mathewson, K. I. Jang, J. Kim, H. Fu, X. Huang, P. Chava, R. Wang, S. Bhole, L. Wang, Y. J. Na, Y. Guan, M. Flavin, Z. Han, Y. Huang, J. A. Rogers, "Soft microfluidic assemblies of sensors, circuits, and radios for the skin", *Science* 344, 70 (2014).

[16] K. I. Jang, K. Li, H. U. Chung, S. Xu, H. N. Jung, Y. Yang, J. W. Kwak, H. H. Jung, J. Song, C. Yang, A. Wang, Z. Liu, J. Y. Lee, B. H. Kim, J. H. Kim, J. Lee, Y. Yu, B. J. Kim, H. Jang, K. J. Yu, J. Kim, J. W. Lee, J. W. Jeong, Y. M. Song, Y. Huang, Y. Zhang, J. A. Rogers, "Self-assembled three dimensional network designs for soft electronics", *Nat. Commun.* 8, 15894 (2017).

[17] T. Sekitani, H. Nakajima, H. Maeda, T. Fukushima, T. Aida, K. Hata, T. Someya, "Stretchable active-matrix organic light-emitting diode display using printable elastic conductors", *Nat. Mater.* 8, 494 (2009).

[18] S. Wang, J. Xu, W. Wang, G. N. Wang, R. Rastak, F. Molina-Lopez, J. W. Chung, S. Niu, V. R. Feig, J. Lopez, T. Lei, S. K. Kwon, Y. Kim, A. M. Foudeh, A. Ehrlich, A. Gasperini, Y. Yun, B. Murmann, J. B. Tok, Z. Bao, "Skin electronics from scalable fabrication of an intrinsically stretchable transistor array", *Nature* 555, 83 (2018).

[19] T. Someya, *Stretchable Electronics*, Wiley-VCH Verlag GmbH & Co. KGaA, 2012.

[20] D.-H. Kim, J. A. Rogers, "Stretchable electronics: materials strategies and devices", *Adv. Mater.* 20, 4887 (2008).

[21] S. Xu, Z. Yan, K. I. Jang, W. Huang, H. Fu, J. Kim, Z. Wei, M. Flavin, J. McCracken, R. Wang, A. Badea, Y. Liu, D. Xiao, G. Zhou, J. Lee, H. U. Chung, H. Cheng, W. Ren, A. Banks, X. Li, U. Paik, R. G. Nuzzo, Y. Huang, Y. Zhang, J. A. Rogers, "Assembly of micro/nanomaterials into complex, three-dimensional architectures by compressive buckling", *Science* 347, 154 (2015).

[22] T. Sekitani, T. Someya, "Stretchable, large-area organic electronics", *Adv. Mater.* 22, 2228 (2010).

[23] K. Chen, W. Gao, S. Emaminejad, D. Kiriya, H. Ota, H. Y. Nyein, K. Takei, A. Javey, "Printed carbon nanotube electronics and sensor systems", *Adv. Mater.* 28, 4397 (2016).

[24] K. Khoshmanesh, S. Y. Tang, J. Y. Zhu, S. Schaefer, A. Mitchell, K. Kalantar-Zadeh, M. D. Dickey, "Liquid metal enabled microfluidics", *Lab Chip* 17, 974 (2017).

[25] M. D. Dickey, "Emerging applications of liquid metals featuring surface oxides", *ACS Appl. Mater. Interfaces* 6, 18369 (2014).

[26] I. D. Joshipura, H. R. Ayers, C. Majidi, M. D. Dickey, "Methods to pattern liquid metals", *J. Mater. Chem. C* 3, 3834 (2015).

[27] S. H. Jeong, A. Hagman, K. Hjort, M. Jobs, J. Sundqvist, Z. Wu, "Liquid alloy printing of microfluidic stretchable electronics", *Lab Chip* 12, 4657 (2012).

[28] N. Lazarus, S. S. Bedair, I. M. Kierzewski, "Ultrafine pitch stencil printing of liquid metal alloys", *ACS Appl. Mater. Interfaces* 9, 1178 (2017).

[29] C. W. Park, Y. G. Moon, H. Seong, S. W. Jung, J. Y. Oh, B. S. Na, N. M. Park, S. S. Lee, S. G. Im, J. B. Koo, "Photolithography-based patterning of liquid metal interconnects for monolithically integrated stretchable circuits", *ACS Appl. Mater. Interfaces* 8, 15459 (2016).

[30] T. Lu, E. J. Markvicka, Y. Jin, C. Majidi, "Soft-matter printed circuit board with UV laser micropatterning", *ACS Appl. Mater. Interfaces* 9, 22055 (2017).

[31] M. R. Khan, C. B. Eaker, E. F. Bowden, M. D. Dickey, "Giant and switchable surface activity of liquid metal via surface oxidation", *Proc. Natl. Acad. Sci. U.S.A.* 111, 14047 (2014).

[32] A. Tabatabai, A. Fassler, C. Usiak, C. Majidi, "Liquid-phase gallium-indium alloy electronics with microcontact printing", *Langmuir* 29, 6194 (2013).

[33] J. W. Boley, E. L. White, G. T. C. Chiu, R. K. Kramer, "Direct writing of gallium-indium alloy for stretchable electronics", *Adv. Funct. Mater.* 24, 3501 (2014).

[34] C. Ladd, J. H. So, J. Muth, M. D. Dickey, "3D printing of free standing liquid metal microstructures", *Adv. Mater.* 25, 5081 (2013).

[35] Y.-L. Park, C. Bor-Rong, R. J. Wood, "Design and fabrication of soft artificial Skin using embedded microchannels and liquid conductors", *IEEE Sens. J.* 12, 2711 (2012).

[36] Y. Lin, O. Gordon, M. R. Khan, N. Vasquez, J. Genzer, M. D. Dickey, "Vacuum filling of complex microchannels with liquid metal", *Lab Chip* 17, 3043 (2017).

[37] B. A. Gozen, A. Tabatabai, O. B. Ozdoganlar, C. Majidi, "High-density soft-matter electronics with micron-scale line width", *Adv. Mater.* 26, 5211 (2014).

[38] J. A. Rogers, R. Ghaffari, D.-H. Kim, *Stretchable Bioelectronics for Medical Devices and Systems*, Springer International Publishing, 2016.

[39] M. Amjadi, K. U. Kyung, I. Park, M. Sitti, "Stretchable, skin-mountable, and wearable wtrain sensors and their potential applications: A Review", *Adv. Funct. Mater.* 26, 1678 (2016).

[40] T. Yamada, Y. Hayamizu, Y. Yamamoto, Y. Yomogida, A. Izadi-Najafabadi, D. N. Futaba, K. Hata, "A stretchable carbon nanotube strain sensor for human-motion detection", *Nat. Nanotechnol.* 6, 296 (2011).

[41] N. Lu, C. Lu, S. Yang, J. Rogers, "Highly sensitive skin-mountable strain gauges based entirely on elastomers", *Adv. Funct. Mater.* 22, 4044 (2012).

[42] M. Amjadi, A. Pichitpajongkit, S. Lee, S. Ryu, I. Park, "Highly stretchable and sensitive strain sensor based on silver nanowire-elastomer nanocomposite", *ACS Nano* 8, 5154 (2014).

[43] X. Xiao, L. Yuan, J. Zhong, T. Ding, Y. Liu, Z. Cai, Y. Rong, H. Han, J. Zhou, Z. L. Wang, "High-strain sensors based on ZnO nanowire/polystyrene hybridized flexible films", *Adv. Mater.* 23, 5440 (2011).

[44] J. Lee, S. Kim, J. Lee, D. Yang, B. C. Park, S. Ryu, I. Park, "A stretchable strain sensor based on a metal nanoparticle thin film for human motion detection", *Nanoscale* 6, 11932 (2014).

[45] M. Segev-Bar, H. Haick, "Flexible sensors based on nanoparticles", *ACS Nano* 7, 8366 (2013).

[46] S. Kim, J. Lee, B. Choi, "Stretching and twisting sensing with liquid-metal strain gauges printed on silicone elastomers", *IEEE Sens. J.* 15, 6077 (2015).

[47] R. Matsuzaki, K. Tabayashi, "Highly stretchable, global, and distributed local strain sensing line using GaInSn electrodes for wearable electronics", *Adv. Funct. Mater.* 25, 3806 (2015).

[48] J. T. Muth, D. M. Vogt, R. L. Truby, Y. Menguc, D. B. Kolesky, R. J. Wood, J. A. Lewis, "Embedded 3D printing of strain sensors within highly stretchable elastomers", *Adv. Mater.* 26, 6307 (2014).

[49] J. Park, I. You, S. Shin, U. Jeong, "Material approaches to stretchable strain sensors", *ChemPhysChem* 16, 1155 (2015).

[50] Y. Lu, Q. Hu, Y. Lin, D. B. Pacardo, C. Wang, W. Sun, F. S. Ligler, M. D. Dickey, Z. Gu, "Transformable liquid-metal nanomedicine", *Nat. Commun.* 6, 10066 (2015).

[51] N. Hallfors, A. Khan, M. D. Dickey, A. M. Taylor, "Integration of pre-aligned liquid metal electrodes for neural stimulation within a user-friendly microfluidic platform", *Lab Chip* 13, 522 (2013).

[52] J. H. So, M. D. Dickey, "Inherently aligned microfluidic electrodes composed of liquid metal", *Lab Chip* 11, 905 (2011).

[53] P. Surmann, H. Zeyat, "Voltammetric analysis using a self-renewable non-mercury electrode", *Anal. Bioanal. Chem.* 383, 1009 (2005).

[54] V. Sivan, S.-Y. Tang, A. P. O'Mullane, P. Petersen, N. Eshtiaghi, K. Kalantar-zadeh, A. Mitchell, "Liquid metal marbles", *Adv. Funct. Mater.* 23, 144 (2013).

[55] S. Y. Tang, B. Ayan, N. Nama, Y. Bian, J. P. Lata, X. Guo, T. J. Huang, "On-chip production of size-controllable liquid metal microdroplets using acoustic waves", *Small* 12, 3861 (2016).

[56] H. Ota, K. Chen, Y. Lin, D. Kiriya, H. Shiraki, Z. Yu, T. J. Ha, A. Javey, "Highly deformable liquid-state heterojunction sensors", *Nat. Commun.* 5, 5032 (2014).

[57] S. Imani, A. J. Bandodkar, A. M. Mohan, R. Kumar, S. Yu, J. Wang, P. P. Mercier, "A wearable chemical-electrophysiological hybrid biosensing system for real-time health and fitness monitoring", *Nat. Commun.* 7, 11650 (2016).

[58] P. Simon, Y. Gogotsi, "Materials for electrochemical capacitors", *Nat. Mater.* 7, 845 (2008).

[59] W. Liu, M. S. Song, B. Kong, Y. Cui, "Flexible and stretchable energy storage: recent advances and future perspectives", *Adv. Mater.* 29, 1603436 (2017).

[60] Y. Zhang, Y. Huang, J. A. Rogers, "Mechanics of stretchable batteries and supercapacitors", *Curr. Opin. Solid State Mater. Sci.* 19, 190 (2015).

[61] N. A. Kyerematen, T. Brousse, D. Pech, "Microsupercapacitors as miniaturized energy-storage components for on-chip electronics", *Nat. Nanotechnol.* 12, 7 (2017).

[62] S. W. Lee, B. M. Gallant, H. R. Byon, P. T. Hammond, Y. Shao-Horn, "Nanostructured carbon-based electrodes: bridging the gap between thin-film lithium-ion batteries and electrochemical capacitors", *Energy Environ. Sci.* 4, 1972 (2011).

[63] C. Yan, P. S. Lee, "Stretchable energy storage and conversion devices", *Small* 10, 3443 (2014).

[64] C. Yu, C. Masarapu, J. Rong, B. Wei, H. Jiang, "Stretchable supercapacitors based on buckled single-walled carbon-nanotube macrofilms", *Adv. Mater.* 21, 4793 (2009).

[65] Z. Niu, H. Dong, B. Zhu, J. Li, H. H. Hng, W. Zhou, X. Chen, S. Xie, "Highly stretchable, integrated supercapacitors based on single-walled carbon nanotube films with continuous reticulate architecture", *Adv. Mater.* 25, 1058 (2013).

[66] X. Chen, H. Lin, P. Chen, G. Guan, J. Deng, H. Peng, "Smart, stretchable supercapacitors", *Adv. Mater.* 26, 4444 (2014).

[67] J. Zang, C. Cao, Y. Feng, J. Liu, X. Zhao, "Stretchable and high-performance supercapacitors with crumpled graphene papers", *Sci. Rep.* 4, 6492 (2014).

[68] F. Xiao, S. Yang, Z. Zhang, H. Liu, J. Xiao, L. Wan, J. Luo, S. Wang, Y. Liu, "Scalable synthesis of freestanding sandwich-structured graphene/polyaniline/graphene nanocomposite paper for flexible all-solid-state supercapacitor", *Sci. Rep.* 5, 9359 (2015).

[69] L. Liu, Z. Niu, L. Zhang, W. Zhou, X. Chen, S. Xie, "Nanostructured graphene composite papers for highly flexible and foldable supercapacitors", *Adv. Mater.* 26, 4855 (2014).

[70] L. L. Zhang, X. Zhao, M. D. Stoller, Y. Zhu, H. Ji, S. Murali, Y. Wu, S. Perales, B. Clevenger, R. S. Ruoff, "Highly conductive and porous activated reduced graphene oxide films for high-power supercapacitors", *Nano Lett.* 12, 1806 (2012).

[71] L. Hu, M. Pasta, F. L. Mantia, L. Cui, S. Jeong, H. D. Deshazer, J. W. Choi, S. M. Han, Y. Cui, "Stretchable, porous, and conductive energy textiles", *Nano Lett.* 10, 708 (2010).

[72] M. Kaempgen, C. K. Chan, J. Ma, Y. Cui, G. Gruner, "Printable thin film supercapacitors using single-walled carbon nanotubes", *Nano Lett.* 9, 1872 (2009).

[73] P. Xu, T. Gu, Z. Cao, B. Wei, J. Yu, F. Li, J.-H. Byun, W. Lu, Q. Li, T.-W. Chou, "Carbon nanotube fiber based stretchable wire-shaped supercapacitors", *Adv. Energy Mater.* 4, 1300759 (2014).

[74] D. Kim, G. Shin, Y. J. Kang, W. Kim, J. S. Ha, "Fabrication of a stretchable solid-state micro-supercapacitor array", *ACS Nano* 7, 7975 (2013).

[75] D. Kim, J. Yun, G. Lee, J. S. Ha, "Fabrication of high performance flexible micro-supercapacitor arrays with hybrid electrodes of MWNT/V2O5 nanowires integrated with a SnO2 nanowire UV sensor", *Nanoscale* 6, 12034 (2014).

[76] T. Sekitani, Y. Noguchi, K. Hata, T. Fukushima, T. Aida, T. Someya, "A rubberlike stretchable active matrix using elastic conductors", *Science* 321, 1468 (2008).

[77] L. Guo, S. P. DeWeerth, "High-density stretchable electronics: toward an integrated multilayer composite", *Adv. Mater.* 22, 4030 (2010).

[78] M. Motoyoshi, "Through-Silicon Via (TSV)", *Proc. IEEE* 97, 43 (2009).

[79] M.-g. Kim, H. Alrowais, S. Pavlidis, O. Brand, "Size-scalable and high-density liquid-metal-based soft electronic passive components and circuits using soft lithography", *Adv. Funct. Mater.* 27, 1604466 (2017).

[80] M.-g. Kim, H. Alrowais, S. Pavlidis, Oliver Brand, "Scalable liquid metal thin line patterning for passive electronic components using soft lithography", presented at *The 16th Solid-State Sensors, Actuators and Microsystems Workshop*, 62-63, Hilton Head, USA, 2016.

[81] D. Qin, Y. Xia, G. M. Whitesides, "Soft lithography for micro- and nanoscale patterning", *Nat. Protoc.* 5, 491 (2010).

[82] J. T. B. Overvelde, Y. Mengüç, P. Polygerinos, Y. Wang, Z. Wang, C. J. Walsh, R. J. Wood, K. Bertoldi, "Mechanical and electrical numerical analysis of soft liquid-embedded deformation sensors analysis", *Extreme Mech. Lett.* 1, 42 (2014).

[83] M. A. H. Khondoker, D. Sameoto, "Fabrication methods and applications of microstructured gallium based liquid metal alloys", *Smart Mater. Struct.* 25, 093001 (2016).

[84] M.-g. Kim, C. Kim, H. Alrowais, O. Brand, "Multiscale and uniform liquid metal thin-film patterning based on soft lithography for 3D heterogeneous integrated soft microsystems: additive stamping and subtractive reverse stamping", *Adv. Mater. Technol.* 3, 1800061 (2018).

[85] M.-g. Kim, C. Kim, H. Alrowais, O. Brand, "Multiscale liquid metal thin-film patterning based on soft lithography for skin-mountable, soft and 3D-integrated biological microsystems", presented at *The 17th Solid-State Sensors, Actuators and Microsystems Workshop*, 42-45, Hilton Head, USA, 2018.

[86] D. Kim, Y. Lee, D.-W. Lee, W. Choi, K. Yoo, J.-B. Lee, "Hydrochloric acid-impregnated paper for gallium-based liquid metal microfluidics", *Sens. Actuators B-Chem.* 207, 199 (2015).

[87] G. Li, M. Parmar, D. W. Lee, "An oxidized liquid metal-based microfluidic platform for tunable electronic device applications", *Lab Chip* 15, 766 (2015).

[88] A. Fassler, C. Majidi, "Soft-matter capacitors and inductors for hyperelastic strain sensing and stretchable electronics", *Smart Mater. Struct.* 22, 055023 (2013).

[89] F. Yu-Min, Y. R. Liang, C. Yu-Ting, W. Pu-Wei, "A combined process of liftoff and printing for the fabrication of scalable inkjet printed microstructures on a flexible substrate", *IEEE Trans. Electron Devices* 62, 1248 (2015).

[90] Q.-A. Huang, L. Dong, L.-F. Wang, "LC passive wireless sensors toward a wireless sensing platform: status, prospects, and challenges", *J. Microelectromech. Syst.* 25, 822 (2016).

[91] N. Lazarus, C. D. Meyer, S. S. Bedair, H. Nochetto, I. M. Kierzewski, "Multilayer liquid metal stretchable inductors", *Smart Mater. Struct.* 23, 085036 (2014).

[92] J. Jinsol, L. Jungchul, "Design, fabrication, and characterization of liquid metal microheaters", *J. Microelectromech. Syst.* 23, 1156 (2014).

[93] H. Ota, S. Emaminejad, Y. Gao, A. Zhao, E. Wu, S. Challa, K. Chen, H. M. Fahad, A. K. Jha, D. Kiriya, W. Gao, H. Shiraki, K. Morioka, A. R. Ferguson, K. E. Healy, R. W. Davis, A. Javey, "Application of 3D printing for smart objects with embedded electronic sensors and systems", *Adv. Mater. Technol.* 1, 1600013 (2016).

[94] N. Lazarus, B. Hanrahan, "Thermotherapy platform based on a highly stretchable wireless heater", *Adv. Mater. Technol.* 1, 1600130 (2016).

[95] D. P. Parekh, C. Ladd, L. Panich, K. Moussa, M. D. Dickey, "3D printing of liquid metals as fugitive inks for fabrication of 3D microfluidic channels", *Lab Chip* 16, 1812 (2016).

[96] C. Pan, K. Kumar, J. Li, E. J. Markvicka, P. R. Herman, C. Majidi, "Visually imperceptible liquid-metal circuits for transparent, stretchable electronics with direct laser Writing", *Adv. Mater.* 30, 1706937 (2018).

[97] A. Hirsch, H. O. Michaud, A. P. Gerratt, S. de Mulatier, S. P. Lacour, "Intrinsically stretchable biphasic (Solid-Liquid) thin metal films", *Adv. Mater.* 28, 4507 (2016).

[98] S. Zhao, J. Li, D. Cao, G. Zhang, J. Li, K. Li, Y. Yang, W. Wang, Y. Jin, R. Sun, C. P. Wong, "Recent advancements in flexible and stretchable electrodes for electromechanical sensors: strategies, materials, and features", *ACS Appl. Mater. Interfaces* 9, 12147 (2017).

[99] V. E. Abraira, D. D. Ginty, "The sensory neurons of touch", *Neuron* 79, 618 (2013).

[100] M. L. Hammock, A. Chortos, B. C. Tee, J. B. Tok, Z. Bao, "The evolution of electronic skin (e-skin): a brief history, design considerations, and recent progress", *Adv. Mater.* 25, 5997 (2013).

[101] S. P. Lacour, G. Courtine, J. Guck, "Materials and technologies for soft implantable neuroprostheses", *Nat. Rev. Mater.* 1, 16063 (2016).

[102] M.-g. Kim, H. Alrowais, O. Brand, "3D-Integrated and multifunctional all-soft physical microsystems based on liquid metal for electronic skin applications", *Adv. Electron. Mater.* 4, 1700434 (2018).

[103] M.-g. Kim, H. Alrowais, O. Brand, "All-soft physical and chemical microsystems based on liquid metal for wearable electronics applications", presented at *The 30th International Conference on Micro Electro Mechanical Systems*, 1162-1165, Las Vegas, USA, 2017.

[104] F. Pineda, F. Bottausci, B. Icard, L. Malaquin, Y. Fouillet, "Using electrofluidic devices as hyper-elastic strain sensors: Experimental and theoretical analysis", *Microelectron. Eng.* 144, 27 (2015).

[105] J. M. Nassar, M. D. Cordero, A. T. Kutbee, M. A. Karimi, G. A. T. Sevilla, A. M. Hussain, A. Shamim, M. M. Hussain, "Paper skin multisensory platform for simultaneous environmental monitoring", *Adv. Mater. Technol.* 1, 1600004 (2016).

[106] S. Yao, Y. Zhu, "Wearable multifunctional sensors using printed stretchable conductors made of silver nanowires", *Nanoscale* 6, 2345 (2014).

[107] Y.-L. Park, C. Majidi, R. Kramer, P. Bérard, R. J. Wood, "Hyperelastic pressure sensing with a liquid-embedded elastomer", *J. Micromech. Microeng.* 20, 125029 (2010).

[108] R. Zhu, J. M. Azzarelli, T. M. Swager, "Wireless hazard badges to detect nerve-agent simulants", *Angew. Chem. Int. Ed. Engl.* 55, 9662 (2016).

[109] D. H. Kim, N. Lu, R. Ma, Y. S. Kim, R. H. Kim, S. Wang, J. Wu, S. M. Won, H. Tao, A. Islam, K. J. Yu, T. I. Kim, R. Chowdhury, M. Ying, L. Xu, M. Li, H. J. Chung, H. Keum, M. McCormick, P. Liu, Y. W. Zhang, F. G. Omenetto, Y. Huang, T. Coleman, J. A. Rogers, "Epidermal electronics", *Science* 333, 838 (2011).

[110] M.-g. Kim, H. Alrowais, C. Kim, P. Yeon, M. Ghovanloo, O. Brand, "All-soft, battery-free, and wireless chemical sensing platform based on liquid metal for liquid- and gas-phase VOC detection", *Lab Chip* 17, 2323 (2017).

[111] M.-g. Kim, H. Alrowais, C. Kim, O. Brand, "All-soft sensing platform based on liquid metal for liquid- and gas-phase VOC detection", presented at *IEEE Sensors 2016*, 76-78, Orlando, USA, 2016.

[112] A. Sihvola, "Mixing rules with complex dielectric coefficients", *Subsurface Sensing Technologies and Applications* 1, 393 (2000).

[113] D. Lange, O. Brand, H. Baltes, *CMOS Cantilever Sensor Systems*, Springer-Verlag Berlin Heidelberg, 2002.

[114] L. L. Zhang, X. S. Zhao, "Carbon-based materials as supercapacitor electrodes", *Chem. Soc. Rev.* 38, 2520 (2009).

[115] L. Dong, C. Xu, Y. Li, Z.-H. Huang, F. Kang, Q.-H. Yang, X. Zhao, "Flexible electrodes and supercapacitors for wearable energy storage: a review by category", *J. Mater. Chem. A* 4, 4659 (2016).

[116] S. W. Lee, N. Yabuuchi, B. M. Gallant, S. Chen, B. S. Kim, P. T. Hammond, Y. Shao-Horn, "High-power lithium batteries from functionalized carbon-nanotube electrodes", *Nat. Nanotechnol.* 5, 531 (2010).

[117] C. W. Shen, S. X. Xu, Y. X. Xie, M. Sanghadasa, X. H. Wang, L. W. Lin, "A review of on-chip micro supercapacitors for integrated self-powering systems", *J. Microelectromech. Syst.* 26, 949 (2017).

[118] X. Wang, L. Dong, H. Zhang, R. Yu, C. Pan, Z. L. Wang, "Recent progress in electronic skin", *Adv. Sci.* 2, 1500169 (2015).

[119] S. Hong, J. Lee, K. Do, M. Lee, J. H. Kim, S. Lee, D.-H. Kim, "Stretchable electrode based on laterally combed carbon nanotubes for wearable energy harvesting and storage devices", *Adv. Funct. Mater.* 27, 1704353 (2017).

[120] J. Yu, W. Lu, S. Pei, K. Gong, L. Wang, L. Meng, Y. Huang, J. P. Smith, K. S. Booksh, Q. Li, J. H. Byun, Y. Oh, Y. Yan, T. W. Chou, "Omnidirectionally stretchable high-performance supercapacitor based on isotropic buckled carbon nanotube films", *ACS Nano* 10, 5204 (2016).

[121] Y. Rangom, X. Tang, L. F. Nazar, "Carbon nanotube-based supercapacitors with excellent ac line filtering and rate capability via improved interfacial impedance", *ACS Nano* 9, 7248 (2015).

[122] S. W. Lee, J. Kim, S. Chen, P. T. Hammond, Y. Shao-Horn, "Carbon nanotube/manganese oxide ultrathin film electrodes for electrochemical capacitors", *ACS Nano* 4, 3889 (2010).

[123] S. W. Lee, B.-S. Kim, S. Chen, Y. Shao-Horn, P. T. Hammond, "Layer-by-layer assembly of all carbon nanotube ultrathin films for electrochemical applications", *J. Am. Chem. Soc.* 131, 671 (2009).

[124] S. W. Lee, B. M. Gallant, Y. Lee, N. Yoshida, D. Y. Kim, Y. Yamada, S. Noda, A. Yamada, Y. Shao-Horn, "Self-standing positive electrodes of oxidized few-walled carbon nanotubes for light-weight and high-power lithium batteries", *Energy Environ. Sci.* 5, 5437 (2012).

[125] A. Brandt, S. Pohlmann, A. Varzi, A. Balducci, S. Passerini, "Ionic liquids in supercapacitors", *MRS Bull.* 38, 554 (2013).

[126] S. J. Choi, T. H. Kwon, H. Im, D. I. Moon, D. J. Baek, M. L. Seol, J. P. Duarte, Y. K. Choi, "A polydimethylsiloxane (PDMS) sponge for the selective absorption of oil from water", *ACS Appl. Mater. Interfaces* 3, 4552 (2011).

[127] A. Lamberti, F. Clerici, M. Fontana, L. Scaltrito, "A highly stretchable supercapacitor using laser-induced graphene electrodes onto elastomeric substrate", *Adv. Energy Mater.* 6, 1600050 (2016).

[128] R. Zhang, J. Ding, C. Liu, E.-H. Yang, "Highly stretchable supercapacitors enabled by interwoven CNTs partially embedded in PDMS", *ACS Appl. Energy Mater.* 1, 2048 (2018).

[129] X. Yu, S. Yun, J. S. Yeon, P. Bhattacharya, L. B. Wang, S. W. Lee, X. L. Hu, H. S. Park, "Emergent pseudocapacitance of 2D nanomaterials", *Adv. Energy Mater.* 8, 1702930 (2018).

[130] T. Lv, Y. Yao, N. Li, T. Chen, "Highly stretchable supercapacitors based on aligned carbon nanotube/molybdenum disulfide composites", *Angew. Chem. Int. Ed. Engl.* 55, 9191 (2016).

[131] Y. Ko, M. Kwon, W. K. Bae, B. Lee, S. W. Lee, J. Cho, "Flexible supercapacitor electrodes based on real metal-like cellulose papers", *Nat. Commun.* 8, 536 (2017).

[132] Y. Huang, M. Zhong, Y. Huang, M. Zhu, Z. Pei, Z. Wang, Q. Xue, X. Xie, C. Zhi, "A self-healable and highly stretchable supercapacitor based on a dual crosslinked polyelectrolyte", *Nat. Commun.* 6, 10310 (2015).

[133] F. Li, J. Chen, X. Wang, M. Xue, G. F. Chen, "Stretchable supercapacitor with adjustable volumetric capacitance based on 3D interdigital electrodes", *Adv. Funct. Mater.* 25, 4601 (2015).

[134] Y. Zhang, S. Xu, H. Fu, J. Lee, J. Su, K. C. Hwang, J. A. Rogers, Y. Huang, "Buckling in serpentine microstructures and applications in elastomer-supported ultra-stretchable electronics with high areal coverage", *Soft Matter* 9, 8062 (2013).

[135] W. H. Yeo, Y. S. Kim, J. Lee, A. Ameen, L. Shi, M. Li, S. Wang, R. Ma, S. H. Jin, Z. Kang, Y. Huang, J. A. Rogers, "Multifunctional epidermal electronics printed directly onto the skin", *Adv. Mater.* 25, 2773 (2013).

[136] S. Xu, Y. Zhang, J. Cho, J. Lee, X. Huang, L. Jia, J. A. Fan, Y. Su, J. Su, H. Zhang, H. Cheng, B. Lu, C. Yu, C. Chuang, T. I. Kim, T. Song, K. Shigeta, S. Kang, C. Dagdeviren, I. Petrov, P. V. Braun, Y. Huang, U. Paik, J. A. Rogers, "Stretchable batteries with self-similar serpentine interconnects and integrated wireless recharging systems", *Nat. Commun.* 4, 1543 (2013).

[137] J. Park, S. Wang, M. Li, C. Ahn, J. K. Hyun, D. S. Kim, D. K. Kim, J. A. Rogers, Y. Huang, S. Jeon, "Three-dimensional nanonetworks for giant stretchability in dielectrics and conductors", *Nat. Commun.* 3, 916 (2012).

[138] S. Zhu, J.-H. So, R. Mays, S. Desai, W. R. Barnes, B. Pourdeyhimi, M. D. Dickey, "Ultrastretchable fibers with metallic conductivity using a liquid metal alloy core", *Adv. Funct. Mater.* 23, 2308 (2013).